APPLICATION OF THE KELDYSH FORMALISM TO QUANTUM DEVICE

MODELING AND ANALYSIS

A Thesis

Submitted to the Faculty

of

Purdue University

by

Roger K. Lake

In Partial Fulfillment of the

Requirements for the Degree

of

Doctor of Philosophy

August 1992

ACKNOWLEDGMENTS

TABLE OF CONTENTS

LIST OF FIGURES

Figure   Page

Figure   Page

ABSTRACT

Lake, Roger K., Ph.D., Purdue University. August 1992. Application of the Keldysh Formalism to Quantum Device Modeling and Analysis. Major Professor: Supriyo Datta.

The effect of inelastic scattering on quantum electron transport through layered semi-conductor structures is studied numerically using the approach based on the non-equilibrium Green's function formalism of Keldysh, Kadanoff, and Baym. The Markov assumption is not made, and the energy coordinate is retained. The electron-phonon interaction is treated in the self-consistent first Born approximation (SCFBA). The Pauli-exclusion principle is taken into account exactly within the SCFBA. The retention of the energy coordinate allows the calculation of a number of quantities which give insight into the effect of inelastic scattering on electron transport: the effect of inelastic scattering on the occupation of the energy levels, the density of states, the energy distribution of the current density, and the power density is calculated from a quantum kinetic equation for actual device structures under high bias. The approach is used to study the effect of emitter quasi-bound states on the I-V characteristic of resonant tunneling diodes (RTD's), the effect of barrier asymmetry on the phonon-peak in RTD's, and energy balance and heat exchange in mescopic systems.

CHAPTER 1
INTRODUCTION

The treatment of inelastic scattering in quantum transport is interesting from both a theoretical and practical point of view. From a practical perspective, the success of the technology of molecular beam epitaxy has allowed the fabrication of layered semiconductor structures such as double barrier resonant tunneling diodes (DBRTD) [1], superlattices [2], and hot electron injection devices [3] which operate on quantum mechanical principles under high bias. If one wishes to describe experiments on these structures, such as photoluminescence measurements of the occupation of resonant levels [4], or the valley current of a DBRTD [5], a treatment of inelastic scattering is necessary.

Theoretically, there have been many studies of the effect of inelastic scattering on resonant tunneling [6-14]. The treatment of the elastic and inelastic scattering ranges in various degrees of sophistication. As discussed by Pevzner *et al.* and Sols [15, 16], it is relatively easy to treat coherent-elastic scattering from potential barriers and device geometries exactly using numerical methods while the inelastic scattering is treated in an approximation. Two approximations are commonly used [8-12]; 1) the inelastic scattering is confined to a finite region of space, and 2) the inelastic scattering is treated within the one-electron picture, i.e: the Pauli exclusion principle is ignored.

There have been many treatments of inelastic scattering in single barrier [17] and double barrier tunneling [12, 18] using the tunneling Hamiltonian method [17, 19, 20]. However, solutions are only found to first order in the tunneling strength. There have also been a number of treatments of phonon scattering in a resonant site [8-12, 21] using the independent boson model [22]. The coupling of the resonant site to the leads has been included to all orders within the independent boson model [8, 10, 21]. There have been several treatments of tunneling with dissipation based on path-integral calculations [23, 24].

Caroli *et al.* developed a transport theory based on a tight-binding model and the non-equilibrium Green function theory of Keldysh [25] and applied it to single barrier

tunneling with phonons confined to the barrier [26-28] and Combescot applied the formalism to single barrier tunneling with localized states in the barrier [29] and the influence of impurities and the electron-phonon interaction on tunneling in metal-semiconductor contacts [30,31]. The approach was used by Ivezic to study tunneling with magnetic impurity scattering [32]. This approach has recently been used to study phonon scattering in one-dimensional double barrier resonant tunneling solving a model Hamiltonian very similar to the one solved in this work [33]. Feuchtwang developed a similar tunneling theory in the position representation [34,35]. Many of the approaches listed above have been limited to specific single or double barrier tunneling problems.

A numerical approach which has been used to study the effect of inelastic scattering on DBRTD's has been based on a solution of the Wigner-Weyl transform of the Liouville equation for the Wigner function [36-40]. The inclusion of inelastic scattering in the above work has been conceptually problematic [39,40]. The exact forms for the self-energy terms have recently been derived from a Wigner-Weyl transformation of the general equations of Keldysh, Kadanoff, and Baym [40]. However, in practice, a relaxation time approximation is used [36-38,40].

The majority of high-bias semiconductor quantum device simulators are based on the tunneling formula described by Duke [17] and used by Tsu and Esaki [41-44]. In the tunneling formula, a transmission probability across the device is calculated by solving the single particle Schrödinger equation, and the current is calculated by integrating over all energies the transmission probability weighted by the difference of the Fermi factors in the two contacts. There is no inelastic scattering in the device. Thus, in the device, an electron, in the presence of an electric field, accelerates forever, assuming an infinite parabolic band. A current and electrostatic potential drop can be calculated, however, since there are no thermalization processes present in the device, no power is dissipated in the device. Finally, starting from this approach, it is conceptually unclear how to include electron-phonon and electron-electron scattering. Electron-phonon scattering has been included in this approach for one particular problem where it appears to be justified [5,13,45-47].

The approach used in this work begins with the general many body, non-equilibrium Green's function theory of Keldysh, Kadanoff and Baym [25,48] which we will refer to as the KKB formalism. It is restricted to steady-state. The Pauli exclusion principle is rigorously included. Three approximations are made.

i) Electron-phonon interaction is treated in the self-consistent first-Born approximation which means that only one phonon scattering is included, but it is included exactly (to all orders in the language of perturbation theory).

ii) The phonons are modeled as a bath of independent oscillators which interact with the electrons locally. This corresponds to a simple model of deformation potential dispersionless optical phonons with the potential felt by the electrons proportional to the ionic displacement.

iii) The phonon coordinates are traced out by assuming that the phonons remain in equilibrium.

The phonons are not restricted to a finite region of space but extend throughout the device and contacts from $-\infty$ to $+\infty$ in the case of a 1-D [49] simulation.

The fundamental quantity in the KKB formalism is the two-time correlation function, $G^<(r_1,t_1;r_2,t_2)$. By performing a Wigner transform on the time variables, we can write the correlation function as $G^<(r_1,r_2;E,T)$ where $T=\frac{1}{2}(t_1+t_2)$ and $\frac{E}{\hbar}$ is the Fourier transform variable corresponding to the time difference coordinate (t_1-t_2). The fundamental quantity in the Liouville equation, the density matrix, $\rho(r_1,r_2;T)$, is obtained by setting $t_1=t_2$ in $G^<$ which is equivalent to integrating over energy, $\rho(r_1,r_2;T)=\int \frac{dE}{2\pi} G^<(r,r';E,T)$ [39,50].

The KKB formalism gives energy resolved information. The retention of the energy coordinate makes the inclusion of the phonon energy spectrum straight forward both conceptually and in practice. It also allows the calculation of a number of quantities which give insight into the effect of inelastic scattering on quantum electron transport. The effect of transitions between levels can be seen in the occupation of energy levels and in the energy distribution of the current density. Knowing the mean energy of the current density, the spatial distribution of the power being dissipated by the electrons to the phonon bath can be calculated throughout the device. Numerical examples of all the above mentioned quantities will be presented in this thesis.

The material in this thesis is extracted from references [51-55].

CHAPTER 2
STEADY-STATE KKB FORMALISM APPLIED TO A SIMPLE DOUBLE BARRIER RESONANT TUNNELING DIODE

2.1. General Steady-State KKB Formalism

There has been much work based on the KKB formalism and there have been several excellent reviews (see [56-58] and references therein). Recently, the formalism has been used to study the effect of alloy scattering, transient transport, and ac conductance in DBRTD's [59-62], Coulomb effects in three-dimensionally confined DBRTD's [63,64], the Kondo effect [65], and the fractional quantum Hall regime [66]. A general transport formula for steady-state non-equilibrium interacting Fermi systems [67] and for steady-state transport in the presence of ac fields [68] have recently been presented.

Our concern is with steady-state transport in mesoscopic systems. In steady-state, the coupled non-equilibrium Green-function equations take on a relatively simple form which provide a good starting point for a general, quantum- mechanical treatment of electron-phonon and electron-electron interactions in mesoscopic structures far from equilibrium. We summarize below a steady-state version of the KKB formalism that is the starting point of this work.

We do not make the gradient expansion [58] since potentials in mesoscopic systems vary rapidly in space. In steady-state, it is assumed that there is no dependence on the center-of-mass time, $\frac{t+t'}{2}$, and we Fourier transform the relative time coordinate to energy, E. The notation and definitions for the Green's functions and self-energies correspond to that found in [69]. The equations for the retarded Green's function, G^R, and the correlation functions, $G^{\lessgtr}$, are [58,69,70]

$$[E - H_0(r)] \, G^R(r,r';E) - \int dr_1 \, \Sigma^R(r,r_1;E)G^R(r_1,r';E) = \delta(r - r') \quad (2.1)$$

$$G^{\lessgtr}(r,r';E) = \int dr_1 dr_2 G^R(r,r_1;E)\Sigma^{\lessgtr}(r_1,r_2;E)G^{R*}(r',r_2;E) \quad (2.2)$$

Since we are only concerned with steady-state, a boundary term has been dropped from (2) which depends on the time at which the interaction is adiabatically turned on [70]. We write the retarded self-energy, Σ^R, as

$$\Sigma^R(r,r';E) \;=\; \sigma(r,r';E) - \frac{i\Gamma(r,r';E)}{2} \tag{2.3}$$

where $\sigma = \dfrac{\Sigma^R + \Sigma^A}{2}$ and $\dfrac{i\Gamma}{2} = \dfrac{\Sigma^R - \Sigma^A}{2}$. In (3), σ is the Hermitian part of Σ^R, and $\dfrac{i\Gamma}{2}$ is the anti-Hermitian part of Σ^R. If we Fourier transform the relative coordinate, $r - r'$, to $\mathbf{k}$, σ and $\dfrac{i\Gamma}{2}$ become, respectively, the real and imaginary parts of $\Sigma^R(\mathbf{R},\mathbf{k};E)$ where $\mathbf{R}$ is the center-of-mass coordinate, $\dfrac{r + r'}{2}$ [56]. The Hermitian part of Σ^R is the Hilbert transform of the anti-Hermitian part plus a term, Σ_{HF}, due to the singular part of Σ^R from the Hartree-Fock diagrams [56].

$$\sigma(r,r';E) \;=\; \frac{1}{\pi} P \int \frac{dE'}{2\pi} \frac{\Gamma(r,r';E')}{E - E'} + \Sigma_{HF} \tag{2.4}$$

Γ is given by the sum of the in-scattering function, $i\Sigma^<$, and the out-scattering function, $-i\Sigma^>$.

$$\Gamma(r,r';E) \;=\; i\left(\Sigma^<(r,r';E) - \Sigma^>(r,r';E) \right) \tag{2.5}$$

$\Sigma^\lessgtr$ depends on the type of interaction being considered. Once $\Sigma^<$ and $\Sigma^>$ are specified, (1)-(5) plus the equations for $\Sigma^\lessgtr$ become the closed set of equations that need to be solved.

The systems we consider are those with boundary conditions (an applied bias) that have been fixed for a long time. However, there is some evidence from numerical simulations that such systems may not reach steady state [71]; coulomb charging effects can result in high-frequency oscillations in the current for a fixed applied voltage. Under such circumstances, the steady-state equations cannot be used.

2.2. Point Scatterer Model

In this work (following [69]) we use a model for which the in-scattering and out-scattering functions, $\Sigma^<(r,r';E)$ and $\Sigma^>(r,r';E)$, are proportional to delta functions in space. This leads to a simplification of the transport equations as described in the following section. The physical model is described by the following three Hamiltonians [69]. The electrons are described by the one-electron effective mass Hamiltonian

$$H_0 = \frac{(p-eA)^2}{2m^*} + V(r) \tag{2.6}$$

where V includes the linear potential drop and the conduction band discontinuities. Magnetic fields are neglected in this work ($A = 0$). De-phasing is assumed to be caused by a reservoir of independent oscillators (maintained in thermodynamic equilibrium) described by

$$H_B = \sum_m \hbar\omega_m (a_m^\dagger a_m + \frac{1}{2}) \tag{2.7}$$

The electrons are assumed to interact with the bath through a delta potential.

$$H' = \sum_m U \delta(r - r_m)(a_m^\dagger + a_m) \tag{2.8}$$

Assuming a continuum of modes, the sum over m becomes an integral, $\Sigma_m \rightarrow \int dr \int d(\hbar\omega) J_o(r;\hbar\omega)$, where J_o is the density of oscillator modes. One is free to choose the energy spectrum, $J_0(\hbar\omega)$, of the oscillators. In this work, we have used three different models:

i)   Elastic phase breaking, $J_0(\hbar\omega) \sim \delta(\omega)$,

ii) Einstein phonon, $J_0(\hbar\omega) \sim \delta(\omega \pm \omega_0)$, $\qquad \hbar\omega_0 = 36$ meV.

iii) Debye phonon, $J_0(\hbar\omega) \sim \omega^2\theta(\omega_D - |\omega|)$, $\qquad \hbar\omega_D = 20$ meV.

This allows comparisons between simple elastic phase breaking and inelastic scattering where transitions between energy levels are present. When we model inelastic scattering, both the Debye and Einstein oscillators are included. The Debye oscillators allow for small energy transitions and close the energy gap that would otherwise occur in Σ^R at low temperatures [22].

When the Einstein spectrum is used, the local oscillator model corresponds precisely to a simple model for dispersionless deformation potential optical phonons (DPOPs). This is shown as follows. The potential felt by the electrons due to the phonons for DPOPs is

$$H_{ep}(r,t) = \frac{1}{\sqrt{V}} M \sum_q e^{iq \cdot r}(a_q e^{-i\omega_o t} + a_{-q}^\dagger e^{i\omega_o t}) \tag{2.9}$$

Then $D^< = \langle H_{ep}(r,t) H_{ep}(r',t') \rangle$ is [69]

$$D^<(r_1,r_2;\hbar\omega) = M^2(2\pi)\delta(r_1 - r_2) \{[N(\omega_0) + 1] \delta(\omega + \omega_0) + N(\omega_0) \delta(\omega - \omega_0)\} \tag{2.10}$$

where N is the Bose-Einstein factor. This is precisely the form of $D^<$ when using the Einstein spectrum in the local oscillator model (compare eq. (A.8a) in [69]).

2.3. Steady-State KKB Formalism Applied to Point Scatterers

We introduce a few identities and one definition. We need the identities for the electron density per unit energy, $n(r;E) = \dfrac{-i}{2\pi} G^<(r, r; E)$, the hole density, $p(r;E) = \dfrac{i}{2\pi} G^>(r, r; E)$, and the local density of states, $N_0(r\ E) = n(r;E) + p(r;E) = \dfrac{-1}{\pi} Im\, G^R(r, r; E)$. We define the non-equilibrium occupation factor as $f(r;E) = n(r, E)/N_0(r, E)$. At equilibrium, $f(r;E)$ is simply the Fermi-Dirac factor.

In this work, the self-energies for the electron-phonon interaction are evaluated in the self-consistent Born approximation,

$$\Sigma^\lessgtr(r,r';E) = \int dE'\, G^\lessgtr(r,r';E-E')\, D^\lessgtr(r,r';E') \qquad (2.11)$$

where

$$D^\lessgtr(r,r';E) = \int d(t-t')\, e^{iE(t-t')/\hbar} <H'(r,t)H'(r',t')>$$

Since, in our model, the electron-phonon interaction is local, the corresponding self-energies, in the SCFBA, are local. We write the self energies as

$$\Sigma^<(r_1,r_2;E) = -i\,\frac{\hbar}{\tau_p(r_1;E)}\,\delta(r_1-r_2)$$

$$\Sigma^>(r_1,r_2;E) = +i\,\frac{\hbar}{\tau_n(r_1;E)}\,\delta(r_1-r_2)$$

and

$$\Sigma^R(r_1,r_2;E) = [\sigma(r_1;E) - i\,\frac{\hbar}{2\tau_\phi(r_1;E)}]\,\delta(r_1-r_2)$$

where $1/\tau_n$ is the electron outscattering rate, $1/\tau_p$ is the hole outscattering rate, $1/\tau_\phi$ is the total de-phasing rate, and σ is the real part of Σ^R.

Only the diagonal elements of $G^\lessgtr$ are needed to calculate the self-energies because of the local nature of the interaction. With the above identities and definitions, the coupled equations for G^R, the diagonal elements of $G^<$, $\Sigma^\lessgtr$, and Σ^R, take the following forms, respectively,

$$[E - H_0(r) - \sigma(r;E) + i\,\frac{\hbar}{2\tau_\phi(r;E)}]\,G^R(r, r'; E) = \delta(r-r') \qquad (2.12)$$

$$f(r;E) = \frac{1}{N_0(r;E)}\,\frac{\hbar}{2\pi}\int dr'\,\frac{|G^R(r, r'; E)|^2}{\tau_p(r';E)} \qquad (2.13)$$

$$\frac{1}{\tau_p(r;E)} = \frac{2\pi}{\hbar} \int d(\hbar\omega)\, F(r,\hbar\omega)\, N_0(r;E-\hbar\omega)\, f(r;E-\hbar\omega) \qquad (2.14a)$$

$$\frac{1}{\tau_n(r;E)} = \frac{2\pi}{\hbar} \int d(\hbar\omega)\, F(r,\hbar\omega)\, N_0(r;E+\hbar\omega)\, [\,1 - f(r;E+\hbar\omega)\,] \qquad (2.14b)$$

$$\frac{1}{\tau_\phi(r;E)} = \frac{1}{\tau_p(r\,E)} + \frac{1}{\tau_n(r\,E)} \qquad (2.15)$$

So far, in practice, we have ignored the real part of Σ^R. In (14), F is a known function consisting of a strength, U, the density of oscillator modes, J_o, and the Bose Einstein factor, N.

$$F(r,\hbar\omega) = U^2 J_o(r,|\omega|) \begin{cases} N(\omega) & , \; \omega > 0 \\ N(|\omega|)+1 & , \; \omega < 0 \end{cases}$$

Substituting (14a) into (13) gives a homogeneous integral equation for the occupation factor.

$$f(r;E) = \frac{1}{N_0(r;E)} \int dr' \int dE' \, |G^R(r,r';E)|^2 F(r',E') N_o(r';E-E') f(r';E-E') \qquad (2.16)$$

2.3.1. Boundary Conditions

Two boundary conditions have to be specified, one for G^R in Eq. (2.12) and one for f(r;E) in Eq. (2.16). We take these up one by one.

We use open-ended boundary conditions for $G^R(r,r';E)$ to simulate perfectly absorbing contacts. G^R is calculated numerically using a finite difference solution to (2.12) (which is formally equivalent to the tight binding model) on a finite lattice and extended analytically to $\pm\infty$ [72]. This is similar to the asymptotic scattering boundary conditions used by other researchers to calculate a transmission coefficient [42,73-75]. However, there is a subtle difference. Usually, the boundary regions are ideal leads with no scattering of any kind extending to ∞ where, presumably, there is an ideal reservoir which is the contact. By contrast, inelastic scattering is included throughout our boundary regions from $-\infty$ to $+\infty$. In our model, the entire boundary region acts as the contact; we do not conceptually divide up the region into an ideal lead and an ideal reservoir.

The integral equation for f(r;E) is solved subject to the boundary condition that in the contacts

$$f(r;E) = f_o(E - \mu_i) \quad r \in \text{contact } i$$

where f_o is the Fermi-Dirac factor. This is similar in spirit to the boundary condition imposed on the electrostatic potential, and the chemical potentials when solving the drift-diffusion equation [76]. Note that we specify the energy distribution rather than the momentum distribution. Usually, it is the incident momentum distribution that is specified as an equilibrium distribution, both in semi-classical [77] and quantum transport [17, 39, 41, 78, 79]. Despite this difference, in the limit of long τ_ϕ, we find remarkable agreement between simulations based on our approach and simulations from SEQUAL [42-44, 80] based on the Tsu-Esaki approach [41] which assumes phase coherent transport and specifies the incident flux at the boundaries. We also find, for a ballistic wire with M propagating subbands at low temperature and low bias, a conductance of $M\frac{2e^2}{h}$. It thus appears that specifying the equilibrium boundary conditions in terms of the energy distribution rather than the incident momentum distribution makes no significant difference to the result. It will be noted that since inelastic scattering is included throughout our boundary regions, energy and momentum are independent variables related through the spectral function. Consequently, it is somewhat more complicated to impose a boundary condition on the momentum distribution.

The concept of an ideal reservoir [72, 78, 81-84] has received much attention in the field of electron transport in electron waveguide structures since it is implicit but fundamental to the Landauer conductance formula [85] and the multi-probe current formula [79, 86] which have proven so successful in modeling mesoscopic phenomena [87]. An ideal reservoir acts as a black-body for electrons which can be characterized by two properties:

(i) Every electron incident on the reservoir is absorbed.

(ii) The reservoir emits electrons according to an equilibrium thermal distribution.

The boundary conditions on G^R and $f(r;E)$ are consistent with the two properties listed above. The open-ended boundary conditions on G^R ensure property (i). Property (ii) is satisfied since we impose equilibrium statistics over the contact region.

The imposition of equilibrium statistics in the contacts gives rise to a contact resistance in the form of a dis-continuity in the electro-chemical potential at the device-contact interface in the linear-response theory [72], and, for the non-linear theory presented here, a dis-continuity in $f(z;E)$ at the device-contact interface. If we simulate a ballistic wire, the occupation factor calculated for the wire will be the average of the occupation factors in the contacts,

$f_w(E) = \frac{1}{2} [f_o(E - \mu_{C_L}) + f_o(E - \mu_{C_R})]$ where $\mu_{C_{L(R)}}$ is the electro-chemical potential in the left (right) contact. The contact resistance, which appears as a dis-continuity in $f(z;E)$, is a natural result of making the voltage and current measurements between two equilibrium regions [78]. It must appear if we are to find the two-terminal conductance of $M \frac{2e^2}{h}$ for a ballistic wire.

An interesting property of the equilibrium boundary condition is that while current is conserved in the device, it is not conserved in the contacts. If there is scattering throughout the contact regions, then the contacts must be in equilibrium far from the device. Thus no current flows deep inside the contacts, although current flows from the contacts into (or out of) the device. The current density decays exponentially away from the device with a decay length $L_\phi = v \tau_\phi$. If scattering is present in the boundary region adjacent to the device, then the same lack of current conservation occurs for the incident equilibrium flux boundary condition used in the Wigner function and Monte Carlo simulations and the Dirichlet boundary conditions used at ohmic contacts in drift diffusion analysis. For example, in a drift diffusion analysis it is common to assume a constant electrochemical potential, μ, at the contacts. Thus, the current density ($J = -\sigma \nabla \mu$) is zero inside the contacts although a current flows at the device contact interface. Further discussion of the boundary conditions can be found in [69, 72].

In summary, we consider the boundary regions as providing boundary conditions on the 'interesting' region, the device. The boundary regions act as ideal reservoirs. We find the correct contact resistance of $\frac{2e^2}{h}$ per mode. We find excellent agreement with the results from SEQUAL which uses the incident equilibrium flux boundary condition. Current is conserved in the device but not in the boundary regions. This condition is inherent in equilibrium boundary conditions with inelastic scattering present throughout the boundary region.

2.3.2. Current Density and Current Continuity

Equations (2.12) through (2.15) are solved iteratively. After convergence, the off-diagonal elements of $G^<$ can be calculated from the general equation, $G^< = G^R \Sigma^< G^{R\dagger}$ and then the current density, $J(\mathbf{r}; E)$, is calculated from

$$J(r;E) = \frac{-e\hbar}{4\pi m^*} \lim_{r'\to r} [\,(\nabla - \nabla')G^<(r,r';E)\,]$$

$$= \frac{-ie\hbar^2}{4\pi m^*} \int \frac{dr'}{\tau_p(r';E)} [\,G^{R*}(r,r';E)\nabla G^R(r,r';E) - G^R(r,r';E)\nabla G^{R*}(r,r';E)\,] \quad (2.17)$$

It is important that the continuity equation,

$$\int dE\ \nabla\cdot J(r,E) = 0 \qquad (2.18)$$

be satisfied. Mahan has proven that the continuity equation is satisfied for any self-energy which can be written as $\Sigma^{\lessgtr}(x,x') = g(x,x')G^{\lessgtr}(x,x')$ where $x=(r,t)$ and g is a symmetric function which satisfies $g(x,x')=g(x',x)$ [58]. This is true of the self-consistent first Born treatment of the electron-phonon interaction. We have, however, ignored the real part of Σ^R in solving the coupled equations (2.12) - (2.15). We show below that (18) still holds in our formulation of the coupled equations, (2.12) - (2.15).

Starting with equations (2.17) and (2.12), we can show that

$$\frac{1}{e}\nabla\cdot J(r;E) = \frac{p(r;E)}{\tau_p(r;E)} - \frac{n(r;E)}{\tau_n(r;E)} \qquad (2.19)$$

In equilibrium, (2.19) is a statement of detailed balance and is equal to zero at each energy [56]. This can be seen after noting that in equilibrium [69],

$$\frac{f_o(E)}{\tau_\phi(r;E)} = \frac{1}{\tau_p(r;E)} \qquad (2.20)$$

and

$$\frac{1-f_o(E)}{\tau_\phi(r;E)} = \frac{1}{\tau_n(r;E)} \qquad (2.21)$$

Away from equilibrium, we must check that the quantity $\int dE\ \nabla\cdot J(r;E)$ is zero. We write $\dfrac{1}{\tau_n}$ and $\dfrac{1}{\tau_p}$ in (2.19) using (2.14), so that (2.19) integrated over energy becomes

$$\frac{1}{e}\int dE\ \nabla\cdot J(r;E) = \int dE \frac{2\pi}{\hbar}\int dE' \left\{ F(r;E-E')n(r;E')p(r;E) - F(r;E'-E)p(r;E')n(r;E) \right\} \quad (2.22)$$

The right hand side of (2.22) is anti-symmetric under interchange of E and E' and is thus equal to zero. Thus, the divergence of the current in the device is zero. Numerically, we find that the current is conserved throughout the device to within a few percent.

2.3.3. Terminal Current

The total current flowing at each energy is obtained by integrating $J(r;E)$ over a cross section of the device. Choosing the cross-section to be the device contact interface, we can use the divergence theorem to convert the surface integral into a volume integral over the contact since there is no current flowing out the back of the contact at $\pm\infty$. We can then write the terminal current in an alternate form [88]

$$
I_1 = \int dE \int_{r \in C_1} dr \frac{e\hbar}{2\pi} \int dr' \frac{|G^R(r,r';E)|^2}{\tau_\phi(r;E)} \left\{ \frac{f_0(E-\mu_{C_1})}{\tau_\phi(r';E)} - \frac{1}{\tau_p(r';E)} \right\} \quad (2.23)
$$

We have checked numerically that Eq. (2.23) gives the same result for the terminal current as obtained by integrating the current density over a cross-section of the device.

Assuming translational invariance, the 3-D quantities in equations (2.13), (2.17), and (2.23) are reduced to 1-D quantities by projecting onto the transverse eigenstates and averaging over the cross-section. The details are described in Appendix A. Details of the numerical solution of equations (2.12) - (2.15) are given in Appendix B.

2.3.4. Coherent and Incoherent Components of the Current

The coherent and incoherent contributions to the total current can be calculated from (2.23) by breaking up the integral over r' into two parts as described in [89]. We define the coherent current as that part of total current which traverses the device from one contact to the other without suffering a de-phasing event. For a two contact device with contacts C_1 and C_2 sandwiching the "device" with r in contact C_1, the integral in (2.23) would be broken up as follows.

The coherent current is obtained by only integrating r' in (2.23) over contact C_2. Since r' is constrained to C_2, we use (2.20) to write $\dfrac{1}{\tau_p(r';E)}$ in (2.23) as $\dfrac{f_0(E-\mu_{C_2})}{\tau_\phi(r';E)}$. Then the coherent current is given by

$$
I_{\text{coherent}} = \int dE \int_{C_1} dr \frac{e\hbar}{2\pi} \int_{C_2} dr' \frac{|G^R(r,r';E)|^2}{\tau_\phi(r;E)\tau_\phi(r';E)} \left\{ f_0(E-\mu_{C_1}) - f_0(E-\mu_{C_2}) \right\} \quad (2.24)
$$

If we write a transmission coefficient as

$$
T(E) = \int_{C_1} dr \int_{C_2} dr' \, \hbar^2 \frac{|G^R(r,r';E)|^2}{\tau_\phi(r;E)\tau_\phi(r';E)} \quad (2.25)
$$

(2.24) takes the form of the well known tunneling formula [17, 41].

$$I_{coherent} = \frac{e}{h} \int dE \, T(E) \left[f_o(E-\mu_{C_1}) - f_o(E-\mu_{C_2}) \right] \tag{2.26}$$

At first it may seem surprising that the inelastic scattering times in the contacts enter the expression for the transmission coefficient, $T(E)$. We show in Appendix C that the factors of τ_ϕ cancel after performing the integral in (2.25) and that the transmission coefficient takes the same form as that obtained by Fisher and Lee for coherent transport across the device [90] (see Appendix C). However, this does not mean that the coherent component of the current is unaffected by inelastic scattering within the device. The quantity $|G^R(r,r';E)|^2$ in (2.25) is defined by (2.12) which includes an imaginary potential proportional to the dephasing rate $\frac{i\hbar}{2\tau_\phi}$. If the de-phasing rate is increased in the device, $|G^R|^2$ in (2.25) is decreased and thus, $T(E)$ is decreased.

The incoherent component of the terminal current at C_1 is due to that part of the flux that has suffered a de-phasing event in the device. Thus, the incoherent component is obtained by restricting the integral over r' in (2.23) to the device region. Note that if de-phasing is absent in the device, $\frac{1}{\tau_\phi}$ and $\frac{1}{\tau_p}$ in (2.23) will be zero in the device, and the incoherent component will be zero. As mentioned earlier, the coherent current is obtained by integrating r' in (2.23) over C_2. Also, it can be shown that the contribution from integrating r' over C_1 gives zero. The sum of the coherent and incoherent components of the current thus add up to the total current as they must.

2.3.5. Elastic Phase Breaking

Elastic phase breaking scattering occurs when the density of oscillator modes, $J_0(\hbar\omega)$, is proportional to $\delta(\hbar\omega)$. In this instance, $1/\tau_\phi(r;E) \propto N_o(r;E)$ [72]. Since the scattering is elastic, current is conserved at each energy, $\nabla \cdot J(r;E) = 0 \ \forall E$.

For purposes of comparison, it is convenient to have the capability of using a constant τ_ϕ independent of position and energy that is not calculated self-consistently so that $1/\tau_\phi$ is not proportional to N_o. However, we must insure that current continuity is preserved. Since

$$\frac{1}{e} \nabla \cdot J(r;E) = \frac{p(r;E)}{\tau_p(r;E)} - \frac{n(r;E)}{\tau_n(r;E)}$$

current conservation can be ensured if $n(r;E)/\tau_n(r;E) = p(r;E)/\tau_p(r;E)$. Dividing both sides by $N_o(r;E)$ and re-grouping gives

$$\frac{1}{\tau_p(r;E)} = \frac{f(r;E)}{\tau_\phi(r;E)} \tag{2.27}$$

If we set τ_ϕ constant, then we use (2.27) to calculate τ_p in place of Eq. (2.14), and thus ensure current conservation. Examples will be given below of the use of a constant τ_ϕ to simulate de-phasing without inelastic transitions.

2.3.6. Energy Current and Power Dissipation

The energy current, J_E, is

$$J_E(r) = \int dE\, E J_N(r; E) \tag{2.28}$$

where J_N is the particle current. Note the J_E is the *total* energy current not the kinetic energy current, J_{E_k}; $E = E_k + E_c(r)$ where E_k is the kinetic energy and $E_c(r)$ is the potential energy. The power density, $P(r)$, due to loss of energy from the electrons to the phonon bath is

$$P(r) = -\nabla \cdot J_E(r). \tag{2.29}$$

Again, note that in Boltzman transport theory this is always written as the sum of two terms, a term due to the kinetic energy, and a term due to the potential energy,

$$P(r) = -\nabla \cdot J_{E_k}(r) + \mathcal{E}(r) \cdot J(r) \tag{2.30}$$

(cf. eq. (7.39) of [91]). The derivation of (2.30) from (2.29) is trivial but will be shown here since working with total energy is unusual and has caused confusion. Re-write (2.28) as

$$J_E(r) = \int dE_k \left\{ [E_c(r) + E_k] J_N(r;E_k) \right\}$$

$$= E_c(r) J_N(r) + J_{E_k}(r)$$

and take the divergence to obtain (2.30).

2.3.7. Mean Energy of the Current

The mean energy of the current, μ_J, is defined in 1-D as

$$\mu_J = \frac{\int dE\, E J(z;E)}{\int dE\, J(z;E)} \tag{2.31}$$

For low bias, the heat current is defined in the usual way as $J_Q = J_E - \mu J_N$ where μ is

the electrochemical potential [77]. From the definition of μ_J, $J_Q = J_N(\mu_J - \mu)$, and from the definition of the Peltier coefficient (in 1-D), $\pi = J_Q/J_N = \mu_J - \mu$. Also, in 1-D, the power density is proportional to the slope of μ_J: $P(z) = -\dfrac{d}{dz}J_E = -J_N \dfrac{d}{dz}\mu_J$. For this reason, the concept of μ_J is useful for understanding the location and intensity of power dissipation in devices.

2.4. Results and Discussion

The effect of phonon scattering in a simple double barrier device and in a double barrier device with an emitter quasi-bound state will be analyzed. Inelastic scattering will be compared to simple energy broadening such as that obtained from the Breit-Wigner formula. The coherent and incoherent components of the total current will be calculated. By considering the local density of states, $N_o(z;E)$, the non-equilibrium occupation of the energy levels, $f(z;E)$, the energy spectrum of the current density, $J(z;E)$, and the consequent quantities, the mean energy of the current density, μ_J, and the power density, $P(z)$, throughout the device, we will obtain a clear picture of the effect of the electron-phonon scattering on the electron transport.

2.4.1. Device Description

The first device that is modeled is a simple double barrier resonant tunneling diode (DBRTD). The conduction band for the device is shown in Fig. 2.1. The temperature is 77K. A constant effective mass of 0.067 is used. The barrier-well conduction band discontinuity is 220 meV. A linear potential drop is applied. The electrostatic potential is not calculated self-consistently. The lattice constant for the spatial grid is 5Å.

2.4.2. Comparison with Coherent Transport

Fig. 2.2 shows a comparison of I-V characteristics. The dashed line is the output of the program SEQUAL [42-44, 80] which is based on equation (2.26) and assumes phase-coherent transport from contact to contact. Furthermore, the boundary conditions in SEQUAL are specified by an equilibrium incident momentum distribution. The solid line is the output from our quantum kinetic equation solver, labeled KKB, with the phase relaxation time set equal to a constant value, independent of position and energy, of 10 ps. The imaginary term in eq. (2.12) is 0.033 meV. This is a factor of 20 smaller than the smallest energy scale in the
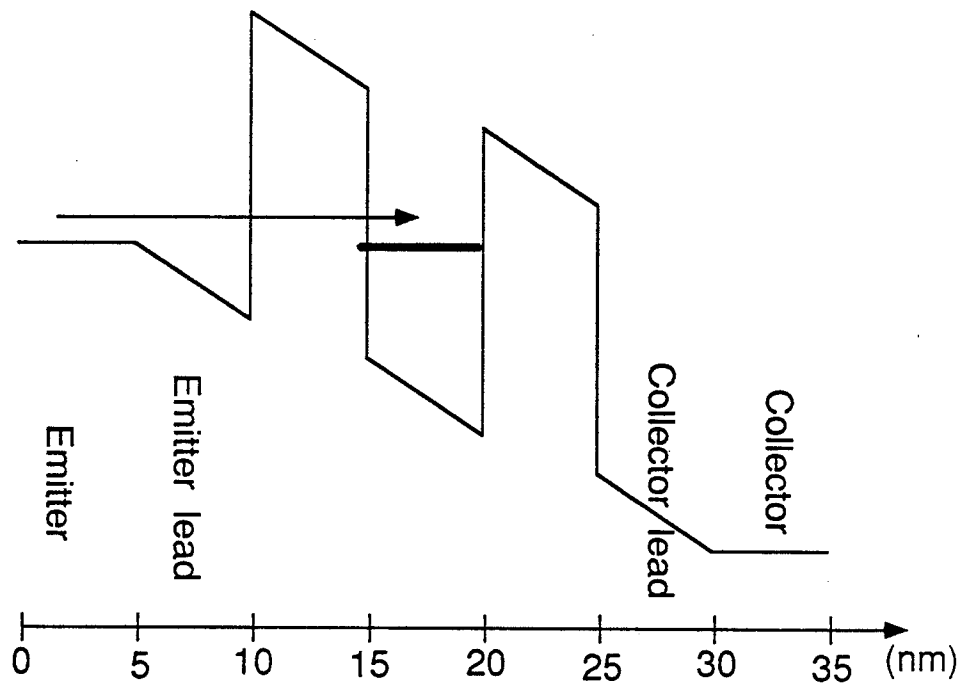
Figure 2.1. Conduction band profile of simple double barrier resonant tunneling diode considered in Figs. 2-8. $T = 77$ K, $m^* = 0.067 m_0$, $\Delta E_c = 220$ meV, $a = 5$Å.
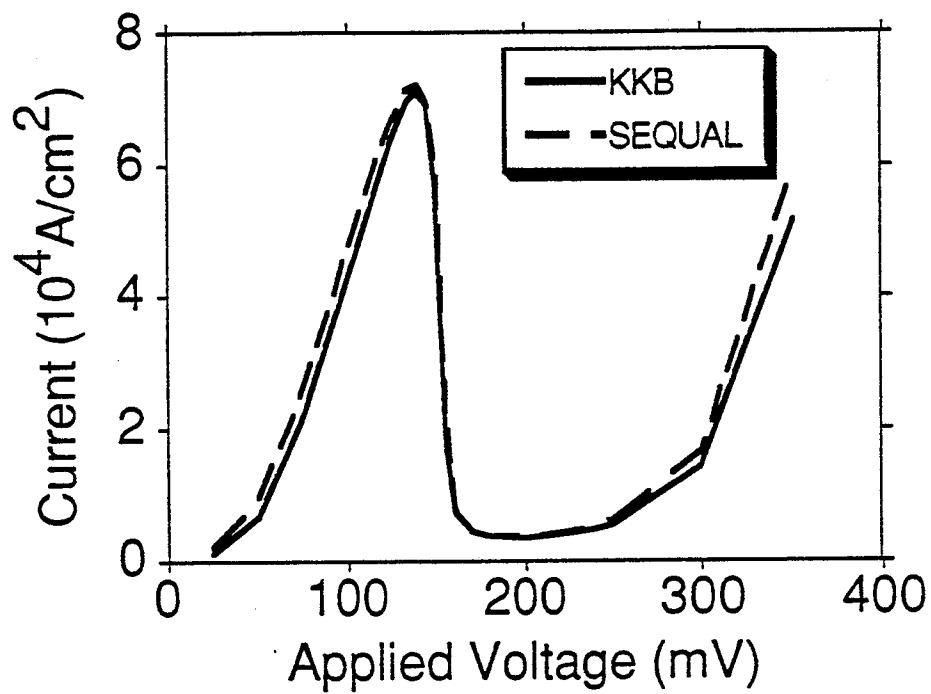
Figure 2.2.   Comparison of the results of simulator based on the Keldysh formalism (KKB) with the results of SEQUAL which assumes phase coherent transport. A constant τ_ϕ of 10 ps is used in the KKB simulator.

problem which is the resonance width. Thus, we are approximating a pure-state retarded-Green's function, $G^R = (E - H_0 + i\delta)^{-1}$, by letting the infinitesimal imaginary term, $i\delta$, become non-zero but small. In this limit, the current is essentially given by (2.24), which is identical to (2.26). Thus, in this limit, we would expect the two simulators to give the same result. Fig. 2.2 shows that this is indeed the case.

The two simulators not only differ in their theoretical basis, but they also differ in their numerical approach. SEQUAL solves for the transmission coefficient, T(E), using a scattering matrix approach. The potential is discretized into a series of steps and the plane-wave eigenstates of each step are matched at the step boundaries. Thus, the dispersion relation is parabolic for all energies above the conduction band. The KKB solver, uses finite-difference to solve (2.12) which is equivalent to tight binding [72] so that the dispersion relation is $E = \dfrac{\hbar^2}{ma^2}[\,1 - \cos(ka)\,]$. The inflection point of the tight-binding band, using the lattice constant and effective mass stated above, occurs at $E = 4.5$ eV. At high applied voltages, when the electrons come through the resonance high into the tight-binding band of the collector, one would expect a difference in the predictions of the two simulators.

2.4.3. Elastic Phase Breaking versus Inelastic Scattering

In Fig. 2.3, the effect of inelastic scattering is compared to elastic energy broadening. For the solid line, both Debye and Einstein oscillators are present. The strengths of the two scattering mechanisms are chosen such that at $5k_B T + \hbar\omega_0$ above the Fermi energy in the emitter, the scattering rate, associated with the retarded self-energy, $1/\tau_\phi$, due to optical phonons is $\sim 10^{13}$ s^{-1} and the scattering rate due to the Debye oscillators is $\sim 10^{12}$ s^{-1}. At non-degenerate energies, the rate $1/\tau_\phi$ should be similar to that calculated from Fermi's Golden Rule. The rate $1/\tau_\phi$ is calculated self-consistently with $G^<$ and, therefore, is position and energy dependent and decreases with decreasing energy.

At peak current, between the barriers, τ_ϕ varies with energy from 0.53 ps at the bottom of the resonance to 0.07 ps one optical phonon energy above the bottom of the resonance [92]. To compare with elastic phase breaking, using a constant τ_ϕ, we have calculated an average τ_ϕ using the energy distribution of the current density as a weighting factor. That is
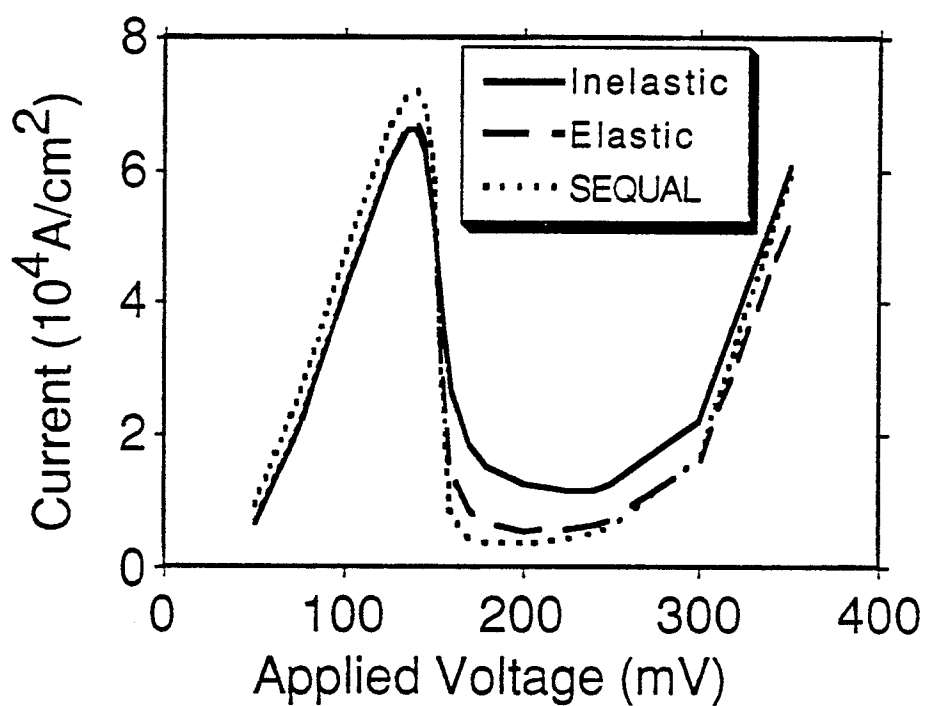
Figure 2.3. Comparison of inelastic scattering, elastic phase-breaking scattering, and phase coherent transport (SEQUAL). For the solid curve, both Debye and Einstein oscillators are present. For the long-dashed curve, only elastic phase-breaking is present; in the well, $\tau_\phi = .46ps$.

$$< \tau_\phi(z_o) > \; = \; \frac{\int dE \; \tau_\phi(z_o;E) \, J(z_o;E)}{\int dE \; J(z_o;E)}$$

where z_o is the point in the center of the well. The value for $<\tau_\phi(z_o)>$ is 0.46 ps. At the node in the emitter contact at the contact-device interface, $<\tau_\phi> = 0.8$ ps

For the long dashed line in Fig. 2.2, τ_ϕ is set to a constant .46 ps in the resonance region and 0.8 ps in the contacts. As described previously, this results in elastic phase breaking. Thus, the energy broadening is roughly the same for the two different simulations; however, in one case there is inelastic scattering present; in the other case, there is not. Also, re-plotted from Fig. 2.2 is the result from SEQUAL, (dotted line).

Comparing the inelastic and elastic I-V characteristics, the shape of the linear and peak part of the I-V curves is the same for both cases. The difference between the two curves lies in the magnitude of the valley current. When there is inelastic scattering present, the valley current is slightly larger because electrons can enter the well at high energy and inelastically scatter down into the resonance thus enhancing the current. For both curves, the peak current is slightly less than and the valley current is more than the result from SEQUAL.

2.4.4. Coherent versus Sequential Tunneling

Since Luryi first introduced the alternative explanation of the I-V characteristic of a DBRTD based on the sequential tunneling picture [93], there has been interest in determining the fraction of the total current that is coherent and incoherent [7,94]. For the I-V curve of Fig. 2.3 with inelastic scattering present, we have plotted the coherent and incoherent components (Fig. 2.4a). Initially, before the peak current is reached, the coherent part is the larger. For the valley current, the incoherent component is larger. This is due to electrons scattering down from their injected energy into the resonance. Past the valley current, the coherent component again becomes larger.

We compare this to Fig. 2.4b in which the elastic curve of Fig. 2.3 is re-plotted along with its coherent and incoherent components. For this simulation, τ_ϕ is kept fixed as described above so that it does not vary with voltage. The current is evenly split between its coherent and incoherent components.

A Breit-Wigner analysis indicates that the ratios of the coherent and incoherent components of the current are inversely related to the intrinsic time and the phase-breaking scattering time, $I_{coherent} / I_{incoherent} = \tau_\phi / \tau_{intrinsic}$ [6]. We estimate the
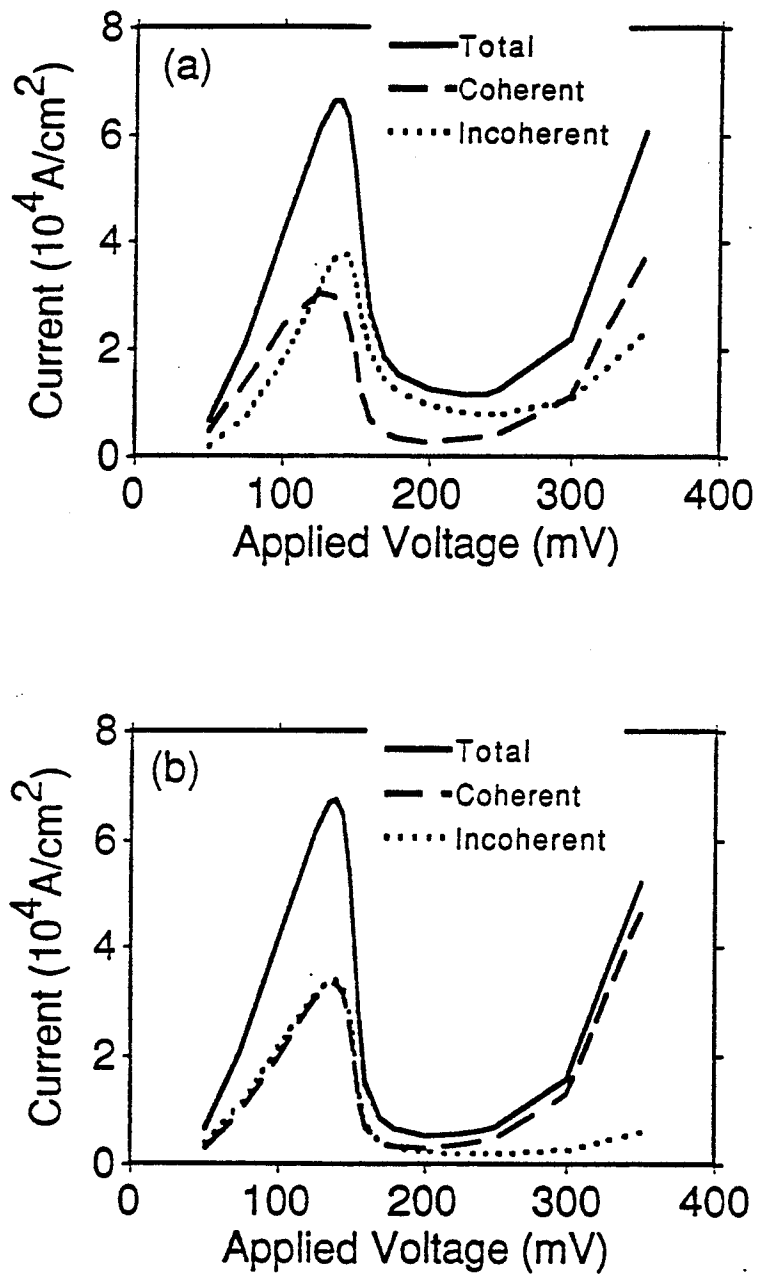
Figure 2.4.   Coherent and incoherent components of the total current. The solid
               (4a) and dashed (4b) curves of Fig. 2.3 are re-plotted. The coherent
               (long dash) and incoherent (dot) components are shown.

intrinsic time using the relation $\dfrac{\hbar}{\tau_{intrinsic}} = \Delta E$ where ΔE is the full width at half maximum of $N_0(z_0;E) = \dfrac{-1}{\pi}ImG^R(z_0,z_0;E)$ at the well center at a bias of 135 mV (peak current) with $\tau_\phi = 10\,ps$. At peak current, for Fig. 2.4b, $I_{coherent}/I_{incoherent} = 0.99$ and $<\tau_\phi>/\tau_{intrinsic} = 1.0$. Thus, if we use a constant time for τ_ϕ, we find good agreement with the prediction of a Breit-Wigner analysis.

2.4.5. Scattering Rates: Energy and Bias Dependence

The energy and bias dependence of τ_ϕ, and the inter-relationship between the non-equilibrium occupation factor, f, the 3-D density of states, N_0, and the inelastic scattering time, τ_ϕ in the self-consistent first Born approximation are demonstrated in Figures 2.5a and 2.5b. Figures 2.5a and 2.5b are overlays of cross-sections taken in position at the well center for the above three quantities plotted versus *total* energy occurring at the peak current and valley current, respectively, of Fig. 2.3. The quantities correspond to the simulation with inelastic scattering present. The scale for τ_ϕ is on the left axis. The scale for N_0 is the right axis. The scale for f is not shown but runs linearly from 0 to 1. Note that N_0 is the 3-D density of states which contains all transverse energies. We now discuss the inter-relationships between the three quantities.

The feature in τ_ϕ at point B in Figs. 2.5a and 2.5b is due to the turn on of optical phonon emission. Point B lies one optical phonon energy above the resonance bottom. In Fig. 2.5a, there is a corresponding feature in f which will be studied more closely in Fig. 2.6. At point A, one optical phonon energy below the resonance, there are prominent features in all of the quantities. There is a peak and precipitous drop-off in the occupation factor, f. This is the result of electrons scattering down from the resonance to fill the exponentially-vanishing states below the resonance. A bump in the density of states also occurs, and there is a sharp decrease in τ_ϕ. In the KKB theory, this decrease in τ_ϕ is formally associated with the emission of phonons by holes (in the conduction band). The small features at points C and D in τ_ϕ correspond to one Debye cut-off energy, 20 meV, below and above the resonance.

In Fig. 2.5b, the conduction band in the emitter is above the level of the resonance and the resonance is 24 $k_B T$ above the Fermi energy of the collector. Thus, the small occupation of the resonance level, ~ 0.03, is due to inelastically scattered electrons from the emitter. Since the occupation is negligible, Fermi's Golden Rule should be a good approximation to the scattering time τ_ϕ. This is correct above the resonance. Below the resonance, the scattering time is dominated by the hole
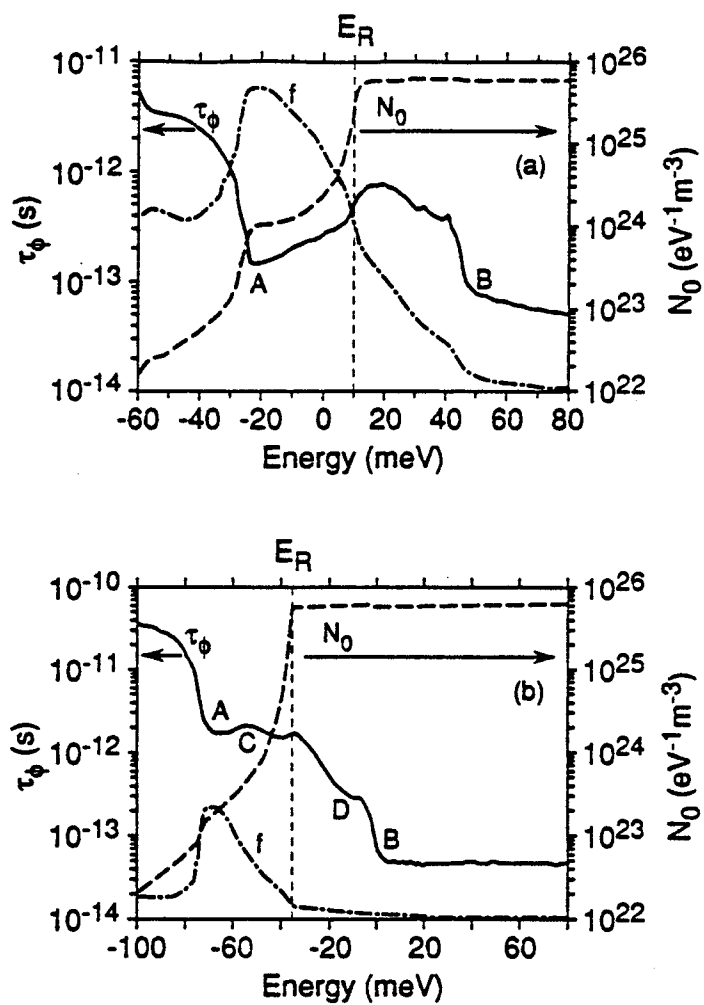
Figure 2.5.   (a) Overlay of $f(z_o;E)$, $N_0(z_o;E)$ and $\tau_\phi(z_o;E)$ at (a) peak current, 135 mV and at (b) valley current 225 mV. z_o is the fixed point in the center of the well. The scale for f is not shown but runs linearly from 0 to 1. E_r is the energy of the bottom of the resonance.

scattering rate, $1/\tau_p$ as discussed below.

The sudden increase in $1/\tau_\phi$ at point A is not due to absorption of optical phonons by electrons. $1/\tau_\phi$ is the imaginary part of Σ^R and it is the sum of the electron outscattering rate $1/\tau_n$ and the hole outscattering rate $1/\tau_p$. This results from the proper treatment of the Pauli exclusion principle built into the KKB formalism [48]. For dispersionless optical phonons, the calculation of $1/\tau_p$ and $1/\tau_n$ is particularly simple.

$$\frac{1}{\tau_n(E)} \propto N(\omega_0)N_0(E+\hbar\omega_0)[\,1-f(E+\hbar\omega_0)\,] \qquad (2.32a)$$

$$+\; [\,N(\omega_0)+1\,]N_0(E-\hbar\omega_0)[\,1\,-\,f(E-\hbar\omega_0)\,]$$

$$\frac{1}{\tau_p(E)} \propto N(\omega_0)N_0(E-\hbar\omega_0)f(E-\hbar\omega_0) \qquad (2.32b)$$

$$+\; [\,N(\omega_0)+1\,]N_0(E+\hbar\omega_0)f(E\,+\,\hbar\omega_0)$$

N is the Bose-Einstein factor, N_0 is the electron density of states, f is the electron occupation factor, and $\hbar\omega_0$ is the optical phonon energy. The position coordinate, r, has been suppressed. In (2.32), letting E be the energy of point A, one finds that the second term of (2.32b) is the largest. This represents the emission of optical phonons by holes which is identical to the emission of optical phonons by electrons one optical phonon energy above point A. At point B, the second term in (2.32a) dominates which represents the emission of optical phonons by electrons.

The slight increase in τ_ϕ after point A is due to the decrease in f(E) above the resonance. Point C occurs one Debye cutoff energy below the resonance. The Debye oscillators cannot start contributing to the rate $1/\tau_\phi$ until the energy is within a Debye cutoff of the resonance. The increase in $1/\tau_\phi$ between the points A and B is due to the Debye oscillators. At energies higher than the resonant energy, the scattering due to the Debye oscillators is dominated by emission by electrons. Above point B, τ_ϕ is determined by the second term in (2.32a). $N_0(E-\hbar\omega_0)$ is constant, $f(E-\hbar\omega_0)$ is negligible; thus, τ_ϕ becomes a constant. Contrasting with point B in Fig. 2.5a, τ_ϕ is not constant, but decreasing since $f(E-\hbar\omega_0)$ is not negligible.

Thus, at energies above resonance, when $f(E-\hbar\omega_0)$ can be ignored, τ_ϕ is given by the same terms as found in Fermi's Golden Rule. However, there is a difference. Fermi's Golden Rule treats the one phonon interaction to first order while the self-consistent first Born approximation (SCFBA) treats the one phonon interaction to all orders. Thus, in the SCFBA, the density of states is affected by the scattering rate.

This effect is seen at point A in Fig. 2.5a and point B in Figs. 2.5a,b (there is a slight decrease in $N_0(E)$ with increasing energy).

To summarize the above discussion of Fig. 2.5, below the resonance, τ_ϕ is determined by a term in the KKB formalism that corresponds to the emission of phonons by holes. This term would be absent in a one-electron picture. It affects the shape of the tail of the resonance. Above the resonance bottom, τ_ϕ is dominated by emission of phonons by electrons, and the terms in the expression are the same terms that appear in Fermi's Golden Rule when the occupation factor can be ignored. The feedback between τ_ϕ and N_0 in the SCFBA alters the density of states.

2.4.6. Non-Equilibrium Distribution Function

Inelastic scattering affects the equilibration of energy levels in the resonance. We demonstrate this in Fig. 2.6. In Fig. 2.6, we plot the occupation factor in the center of the well at peak current for the inelastic and elastic I-V curves of Fig. 2.3, the KKB curve from Fig. 2.2, now labeled "Coherent", and the tail of a Fermi-Dirac function with a Fermi-energy 4 meV below the resonance and a temperature of 205 K labeled "Feq". The arrow represents the energy of the bottom of the resonance.

When only elastic phase-breaking is present, the sequential tunneling picture predicts that the occupation of the well should be proportional to the occupation in the emitter [95]. This is what we find. Above the bottom of the resonance, the occupation in the well for both the elastic and coherent curve is a scaled version of the equilibrium Fermi-Dirac factor in the emitter. For the elastic curve, τ_ϕ is set to a constant value in the well of 0.46 ps and for the coherent curve, τ_ϕ is set to 10 ps. There is essentially no difference in the occupation of the well for the two cases. With only elastic phase-breaking processes, the different energies are in dis-equilibrium, and the occupation factor cannot be fit to the tail of a Fermi-Dirac function.

When inelastic scattering is present (solid line), the electron-state occupation is shifted to lower energies as expected. Furthermore, the occupation above the resonance can be fit fairly well to the tail of a Fermi-Dirac function (long-dashed line). The fit is good for energies above the resonance and below the threshold for optical phonon emission, $E_r < E < E_r + \hbar\omega_0$. At energies above the optical phonon energy, there is a depletion in the calculated occupation factor compared to the equilibrium factor. This is precisely what is expected. As pointed out by Yang et al. [96] and Hess [97], rapid optical-phonon scattering tends to deplete the distribution of carriers with kinetic energies larger than the phonon energy. The phonons tend to cut
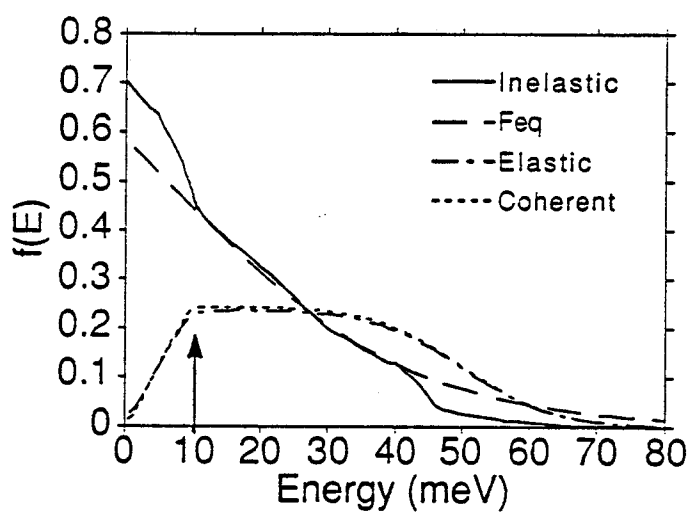
Figure 2.6. (a) f(E) at the well center at peak current (135 mV) for the three cases of inelastic scattering, elastic phase-breaking scattering (from Fig. 2.3) and coherent transport (from solid curve, Fig. 2.2). The tail of a Fermi-Dirac function with a Fermi-energy 4meV below the resonance and a temperature of 205 K is also plotted (Feq). The arrow lies at the energy of the bottom of the resonance, 10 meV.

off the high-energy part of the Boltzmann tail. This is what is shown by our simulations.

2.4.7. Energy Distribution of the Current

The energy distribution of the current density gives us information about the inelastic scattering and power dissipation within the device. In the following plots, Figs. 2.7 and 2.8, we consider the spatial variation of the inelastic scattering intensity and power dissipation. We find a relatively high intensity of inelastic scattering and power dissipation in the resonant regions.

The energy distribution of the current density, $J(z; E)$, at the bottom of the valley current (225 mV in Fig. 2.3) with inelastic scattering present is plotted versus position and energy in Fig. 2.7a. The current enters at the high energy of the emitter, the right side, and the energy distribution changes very little until the 5 nm region of the well. Then there is a major shift in the distribution from the high incoming energy down to the bottom of the resonance level where the distribution peaks sharply . This is shown clearly in Fig. 2.7b where two cross-sections taken from Fig. 2.7a along lines of constant position are plotted. Both curves are taken from a point 1 nm outside the well in the adjacent barrier. The long-dashed curve is from the emitter barrier, and the solid curve is from the collector barrier. The points on the energy axis labeled E_R, E_C, and E_F are the energies of the resonance, the emitter conduction band, and the emitter Fermi level, respectively. Exiting the well, there is little change in the distribution in the collector barrier and lead. Thus, the well is a region of relatively intense inelastic scattering compared to the leads.

This result seems reasonable on physical grounds. In the resonance, the group velocity of the electrons is slow compared to the surrounding regions. If the inelastic scattering time is roughly position independent, then the inelastic scattering length is shorter in the resonance region than in the leads and a higher intensity of energy relaxation results. Defining the power density as the power dissipated by the electrons to the phonon bath, then a peak in the power density results in the region of the resonance.
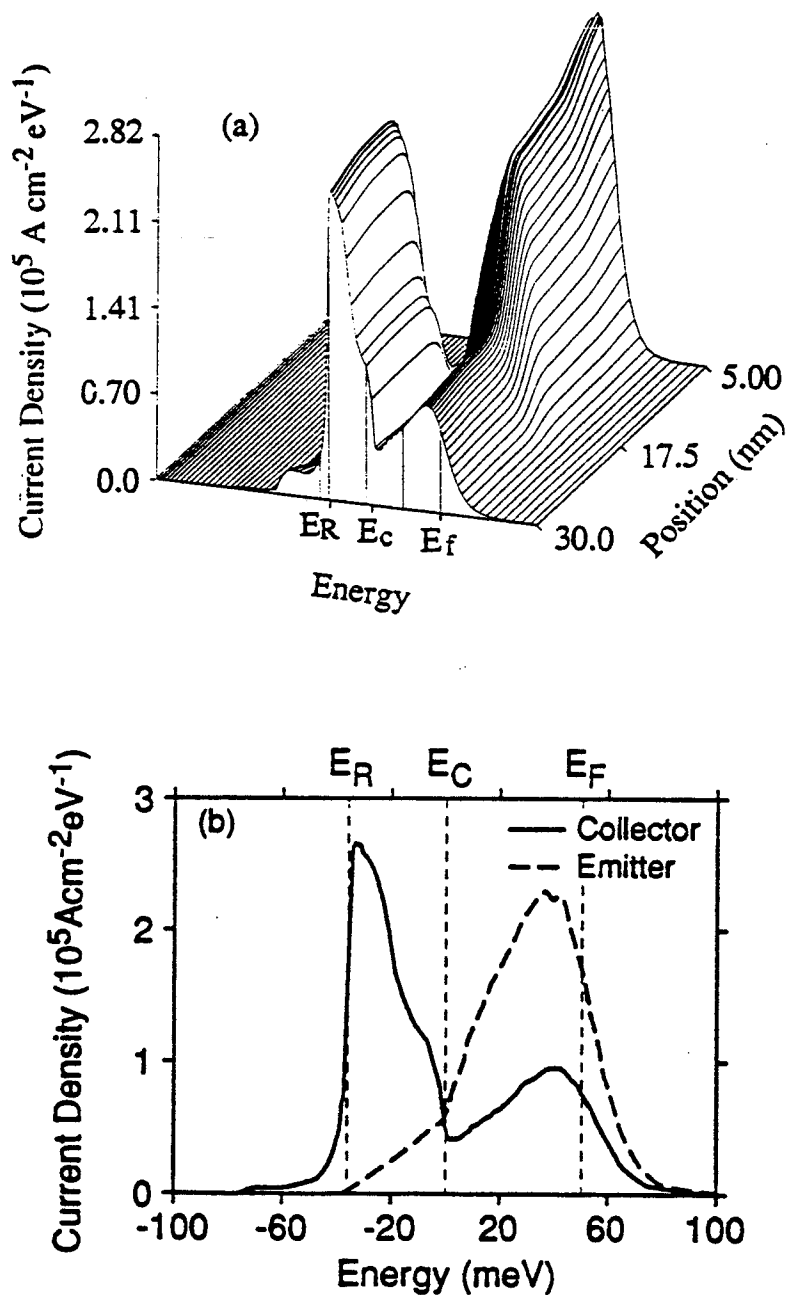
Figure 2.7. (a) J(z;E) plotted versus position and energy at 225 mV with inelastic scattering. E_f is the Fermi-Energy of the emitter, E_c is the level of the conduction band in the emitter, and E_r is the energy of the bottom of the resonance. (b) Cross sections from Fig. 2.7a at constant position 1 nm outside the well in the emitter and collector barrier.

2.4.8. Power Density

The mean energy of the current density, μ_J, is plotted versus position in Fig. 2.8a for the peak current, 135 mV, and the valley current, 225 mV, of Fig. 2.3 when inelastic scattering is present. This shows clearly the relatively large drop in energy that occurs in the well. μ_J is defined such that the power density is proportional to its derivative, $P(z) = -J_N \dfrac{d}{dz} \mu_J$. The power density, plotted in Fig. 2.8b, shows a large peak in the 5 nm region of the well.

Although most of the power loss seems to be occurring in the well, most of the $I \times V$ loss is actually occurring in the contacts (not shown) as in the usual Landauer picture [98]. Only the device region has been plotted in Figs. 2.8a and 2.8b. The total integrated power, $\int dz\, P(z)$, in Fig. 2.8b (225 mV) is ~ 0.18 IV. In a real device, the leads are metallic n^+ material and they are very long, microns instead of nanometers. Very deep in the emitter and collector leads the current is distributed in energy as it would be in an n^+ resistor. The mean energy of the current, μ_J, would lie a distance π (the Peltier coefficient) above the quasi-Fermi energy μ. Since the applied bias is 225 mV, μ_J must drop by 225 meV across the real device. In Fig. 2.8a, the total drop across the "device" is ~ 41 meV which gives the factor of 0.18. Thus, in a real device, the majority of the power dissipation is taking place in the leads and contacts. There is simply a peak in the power density in the resonance region.

The concept of the mean energy of the current density, μ_J, provides a way of qualitatively understanding the location and intensity of the power dissipation in devices and placing upper limits on the amount of power dissipated in any one region. In 1-D, when $\mathbf{J} = J\,\hat{z}$, $P(z) = -\dfrac{d}{dz} J_E(z) = -J_N \dfrac{d}{dz} \mu_J$. The net power being dissipated between points z_0 and z_1 is $J_N\,[\mu_J(z_0) - \mu_J(z_1)]$ where J_N is the particle current. Thus, the net power dissipated in a region is proportional to the drop in μ_J in that region.

As an example, consider the peak current of the device (135 mV). In the Luryi picture [93], at zero temperature, μ_J in the emitter lead equals $E_f/2$ where E_f is the Fermi energy of the emitter contact, and the energy of the bottom of the emitter conduction band is taken to be zero. Since the bottom of the emitter conduction band is aligned with the bottom of the resonance in the well, the maximum drop possible in μ_J between the barriers is $E_f/2$. Thus, the maximum power that can be dissipated between the barriers is $J_N\,E_f/2$ where J_N is the particle current density. For Fig. 2.8,
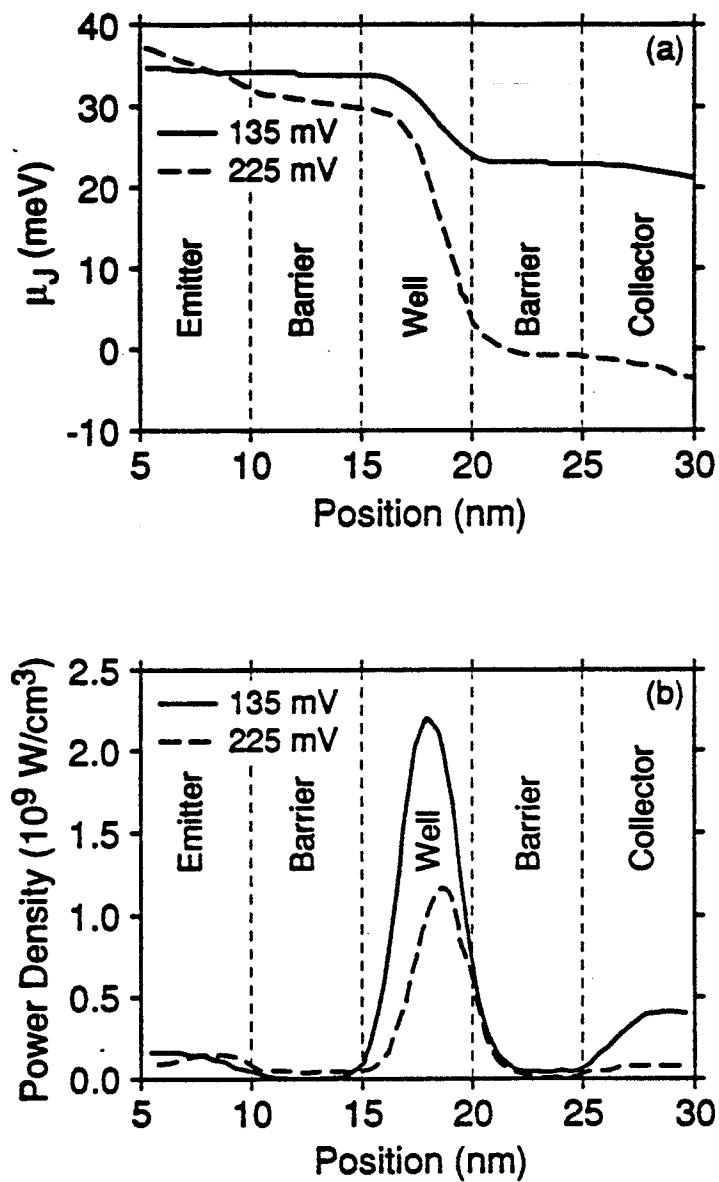
Figure 2.8.   (a) Mean energy of the current density, $\mu_J(z)$, at 135 mV and 225 mV.
(b) Power density, $P(z)$, at 135 mV and 225 mV.

this estimate is a factor of 5 higher than the calculated power dissipated in the well.

2.5. Summary and Conclusion

The non-equilibrium Green's function approach provides a powerful tool for investigating the effect of energy broadening and inelastic scattering in quantum transport. The effects of both constant and energy dependent self-energies calculated in the self-consistent first Born approximation can be compared. Our approach allows the energy spectrum of the phonons to be included, and it allows a self-consistent first Born treatment of the electron-phonon interaction. It also allows the calculation of a number of quantities which give insight into the effect of inelastic processes on quantum electron transport throughout the device. The non-equilibrium occupation factor, $f(z;E)$, shows the effect of inelastic scattering on the equilibration of energy levels. With inelastic scattering present, the occupation of the well of the simple resonant tunneling structure at the peak current can be described by the tail of a Fermi-Dirac factor up to the optical phonon energy at which point the calculated f is depleted. With no inelastic scattering, the occupation of the well is a scaled version of the occupation in the emitter. The local density of states, $N_o(z;E)$, displays how different resonances align with each other and with the conduction band. We have shown that the enhanced valley current due to inelastic scattering is coincident with enhanced occupation of the resonant state. The process of filling the state also is seen in the energy dependent current density, $J(z;E)$, which undergoes a sharp downward shift in the resonance region. This shows up as a peak in the power density between the barriers. Knowing $J(z;E)$, one can calculate the mean current energy, μ_J, and hence the power density throughout the device.

The concept of the mean current energy was introduced and shown to be a valuable intuitive tool by which to understand the spatial variation and intensity of the power dissipation. The mean energy of the current density, indicates where power is being dissipated in a device. We have consistently found peaks in the power density when current passes through a resonance; however, only a fraction of the total IV power is actually dissipated there.

Thus, by including the energy coordinate explicitly and performing energy-resolved computations, one can calculate the occupation of levels $f(z; E)$, the local density of states, $N_o(z;E)$, the energy distribution of the current density, $J(z; E)$, the mean energy of the current, μ_J, and the power density throughout the device. These quantities provide a detailed picture of the effect of inelastic transitions on quantum transport.

CHAPTER 3
THE EFFECT OF EMITTER QUASI-BOUND STATES ON
THE I-V CHARACTERISTIC OF DBRTD'S

3.1. Introduction

The effect of emitter quasi-bound states in double barrier resonant tunneling is studied numerically using an approach based on the non-equilibrium Green's function formalism of Keldysh, Kadanoff, and Baym (KKB). Our method is restricted to steady-state. The electron-phonon interaction is treated in the self-consistent first Born approximation. The phonons are modeled as a bath of independent oscillators which interact with the electrons locally. When an Einstein spectrum is used, this corresponds to a simple model of deformation potential dispersionless optical phonons. In the device simulations, both Einstein and Debye oscillators are present. The Debye oscillators allow for small energy transitions. The energy used for the Einstein phonons, ε_0, is 36 meV. The phonon coordinates are traced out by assuming that the phonons remain in equilibrium. The results from the KKB simulator are compared with results from SEQUAL 2.1 which assumes phase coherent transport [42, 43] and recent experiment [99].

3.2. I-V Characteristics and Density of States

Three double barrier devices are simulated. The difference between them lies in the lengths of the emitter and collector leads. A sketch of the conduction band profile is shown in Fig. 3.1. The temperature is 77K. A constant effective mass of .067 is used. The barrier-well conduction band discontinuity is 220 meV. A simple linear potential drop is used. The electrostatic potential is not calculated self-consistently. The strength of the Einstein phonons and Debye oscillators is chosen such that at 5 $k_B T + \varepsilon_0$ above the emitter Fermi energy, the average scattering rate due to the Debye oscillators is 1.0×10^{12} s^{-1} and the average rate due to the Einstein phonons is $10. \times 10^{12}$ s^{-1}. The rates are calculated self consistently with $G^<$ and therefore are position and energy dependent and decrease with decreasing energy. The difference between the three devices simulated lies in the length L in Fig. 3.1. The I-V

characteristics for lengths 10, 15, and 20 nm are shown in Figs. 3.2-3.4 respectively.
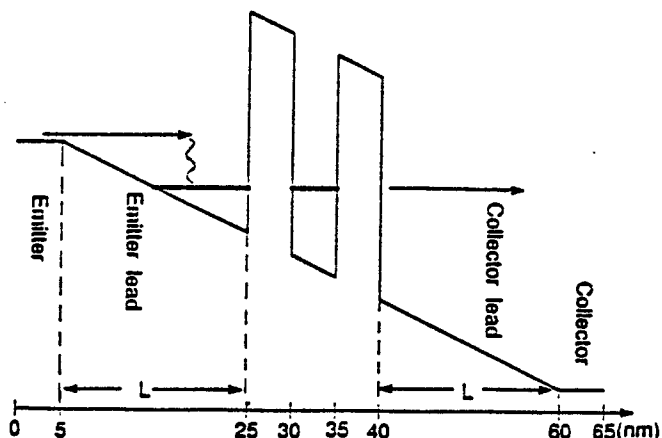
Figure 3.1. Conduction band of device simulated showing quasi-bound states and schematic of inelastic transport process.

Fig. 2.3 shows a comparison of the I-V characteristics for a device with lead lengths, L, of 5 nm calculated from the KKB simulator and SEQUAL. The peak currents occur at the same bias and the peak current from the KKB simulation is slightly less than the peak current from SEQUAL. No emitter quasi-bound state is present.

Fig. 3.2 shows the I-V characteristic when the lead lengths, L, are 10 nm. The peak current from the KKB simulator is now larger than the peak current from SEQUAL and occurs at a slightly higher voltage. Corresponding to the peak bias in the KKB simulation, 135 mV, Fig. 3.2b shows the 1-D density of states $N_0(z;E)$ as a shadow plot versus z and E with the conduction band super-imposed. The transverse energies are ignored in the plot for clarity. Dark regions are high density of states. The dark region between the barriers is the bottom of the quasi-bound state in the well. Fig. 3.2b shows that an emitter quasi-bound state is beginning to form just below the emitter conduction band and that the peak current in the KKB simulation occurs when the resonant state in the well lines up with the quasi-bound state in the emitter lead below the emitter conduction band.

For Fig. 3.3, the lead length L is 15 nm and the emitter quasi-bound state is well defined (Fig. 3.3b). The 1-D DOS is plotted in Fig. 3.3b for the peak current at 170 mV. The peak occurs when the two states align. The first peak in Fig. 3.3a is due to the emitter conduction band passing through the resonance.

When the lead length L is 20 nm, two well defined peaks occur in the I-V characteristic (Fig. 3.4a). The second peak occurs when the emitter quasi-bound state
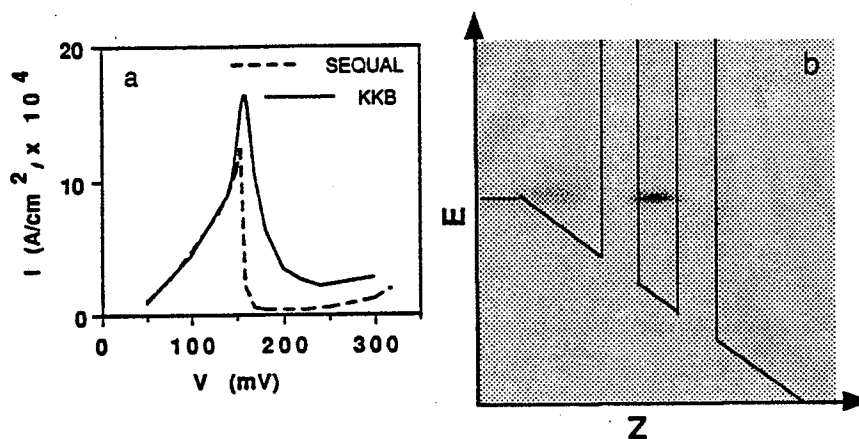
Figure 3.2.   a) I-V of device with L = 10 nm. b) 1-D density of states versus energy and position at peak current, 160 mV.
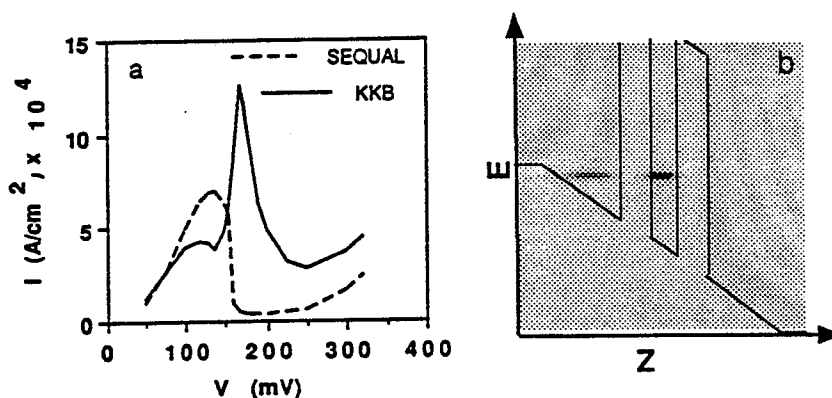
Figure 3.3.   a) I-V of device with L = 15 nm. b) 1-D density of states versus energy and position at peak current, 170 mV.

aligns with the bottom of the resonance in the well.

A recent experiment has observed features in the I-V characteristic that could be attributed to the prescence of quasi-bound states in the emitter lead [99]. To obtain a deep well in the emitter lead, the intrinsic region was 200 nm long on either side of the barriers. It was not feasible to simulate a device of that length with our present computational resources. The Green's function is calculated by a tight-binding technique [72] with a node spacing of 5 Å. The calculation time increases as N^2 where N is the number of nodes. Therefore, the linear potential was used so that well defined emitter states could be formed in relatively short, 15-20 nm, leads. The effect of a self-consistent simulation is to stretch out the I-V characteristic along the voltage axis [42]. The experimental results are similar to Fig. 3.3. There is a small NDR
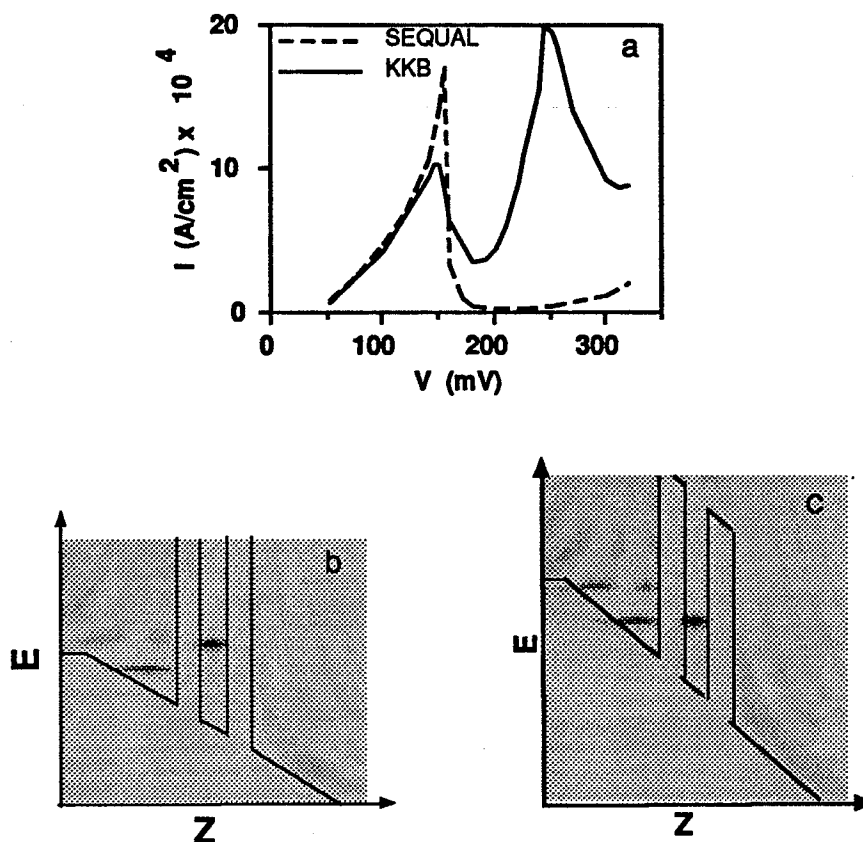
Figure 3.4. a) I-V of device with L = 20 nm. b) 1-D density of states versus energy
and position at first peak current. c) 1-D density of states versus energy
and position at second peak current.

region associated with the first peak but the first peak is not well separated from the second peak as in Fig. 3.4. The structure of Fig. 3.3 was also simulated at T = 150K. The I-V characteristic became slightly more rounded but the change was minor. At the peak current, the aligned states lie 12 meV below the emitter conduction band. The effect of the Debye oscillators on the magnitude of the peak current was investigated by reducing their strength by a factor of 16. This resulted in only a 10% reduction in the peak current. Thus, if an emitter quasi-bound state exists in an experimental device near the bottom of the emitter conduction band at 77K, it is likely to be largely filled by inelastic scattering and contribute a large peak to the I-V characteristic.

3.3. Current Flow and Power Dissipation

The first peak in the I-V characteristic in Figs. 3.3 and 3.4 corresponds to the conduction band in the emitter crossing the resonance level in the well (Fig. 3.4b). The second peak occurs when the quasi-bound state in the emitter lead aligns with the resonance in the well (Fig. 3.4c). In Fig. 3.4c, all of the current is flowing through inelastic channels. All of the current is coming from the emitter, inelastically scattering down into the quasi-bound state and flowing out through the resonance. At the first current peak (Fig. 3.4b), no current is flowing through the emitter quasi-bound state. This is clearly shown in plots of the mean current energy.

The mean current energy, μ_J, corresponding to Fig. 3.4 is plotted in Fig. 3.5a. For the first current peak, the slope of μ_J is smallest in the emitter lead, next largest in the collector lead, and largest in the well. This ordering is expected since the power density is proportional to $\frac{d}{dz}\mu_j$. The maximum power density is in the resonance region. In the collector region, where there is plenty of phase space into which to scatter, the power density is greater than in the emitter lead. The lack of drop in the emitter lead indicates that no current is flowing through the emitter quasi-bound state. At the second current peak, 245 mV, there is a large drop in μ_J in the emitter lead. This is what must occur if current is to flow through the emitter quasi-bound state.

The power density for the two current peaks is shown in Fig. 3.5b. At 150 mV, there is a peak in the power density in the well only. At 245 mV, there are large peaks both in the well and in the emitter lead corresponding to the two quasi-bound states. Again, a cautionary word is in order. Fig. 3.5b does not imply that the majority of the I-V power loss is occurring in the quasi-bound states. The drop in μ_J in the emitter lead at a bias of 245 mV is 39 meV. Thus, 39/245 (.16) of the I-V power is being dissipated in the emitter quasi-bound state; 16/245 (0.065) of the I-V power is dissipated between the barriers; the majority of the power is still being dissipated in the contacts.

3.4. Conclusion

Numerical solutions of the coupled non-equilibrium Green's function equations are presented for different double barrier resonant tunneling devices in the presence of optical phonons and Debye oscillators. Plots of the 1-D DOS show that when a quasi-bound state in the emitter aligns with the state in the well, a large current peak can occur, larger than that due to the emitter conduction band passing through the resonant state. For the device with the I-V characteristic most similar to that observed
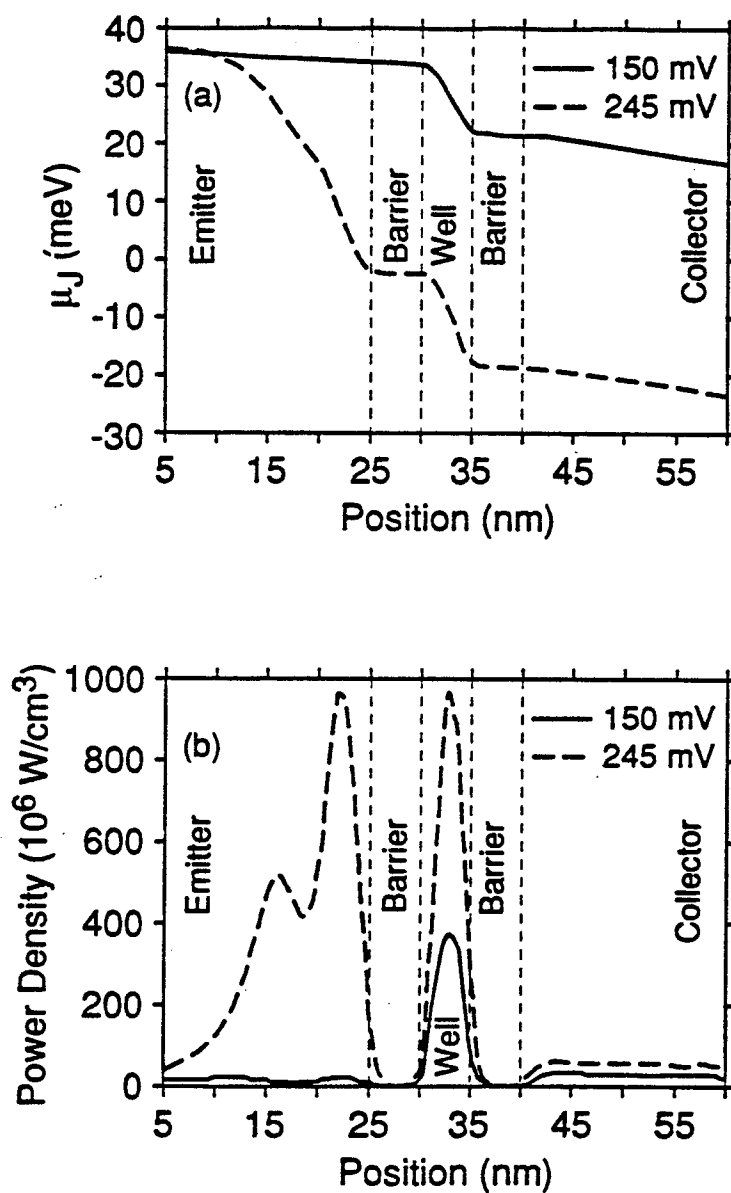
Figure 3.5. (a) Mean current energy, $\mu_J(z)$ corresponding to the two current peaks of Fig. 3.4a. (b) Power density, $P(z)$, corresponding to the two current peaks.

experimentally (Fig. 3.3), two different temperatures were simulated, 77K and 150K, showing little difference on the overall I-V characteristic. Also, the strength of the Debye oscillators was reduced by a factor of 16 and resulted in a decrease of only 10% in the magnitude of the peak current. Thus, if such a state exists in an experimental device, it will be largely populated by inelastic scattering and contribute a peak to the I-V characteristic considerably larger than that predicted by the coherent transport model.

CHAPTER 4
THE EFFECT OF BARRIER ASYMMETRY ON THE PHONON PEAK
IN DOUBLE BARRIER RESONANT TUNNELING DIODES

4.1. Abstract

The effect of barrier asymmetry on optical phonon enhanced tunneling through double barrier resonant tunneling structures is investigated theoretically both numerically and analytically, solving the coupled non-equilibrium Green function equations for a model Hamiltonian. The trends from the numerical simulations are matched well by the results of the analytical expressions. An analysis of the relative effects of elastic dephasing versus optical phonon scattering on enhancing the valley current is made. Within the local phonon model, the effect of barrier asymmetry on the I-V characteristic is to enhance the ratio of the phonon peak to the main resonant peak not by enhancing the phonon peak but by reducing the main peak. The phonon peak is found to be independent of the collector barrier over a wide range of parameters. The effect of barrier asymmetry on the occupation of the resonance is described.

4.2. Introduction

Double barrier resonant tunneling through semiconductor heterostructures has been the subject of intense interest over the past decade, both experimentally and theoretically [100]. Double barrier resonant tunneling diodes (DBRTD's) are of technological importance for high frequency applications. The investigation of the frequency limits of DBRTDs led to a discussion of resonant versus sequential tunneling [93,95] and investigations of the effect of dephasing on the transmission coefficients [7] and I-V characteristic [101]. Inelastic and dephasing processes are also of interest since they enhance the valley current and hence decrease the peak to valley ratio, an indicator of device quality [11,38,40,51,102-108]. Interest in the effect of inelastic processes in resonant tunneling, in particular the effect of optical phonons, was enhanced by the observation of optical phonon assisted tunneling in DBRTDs by Goldman, Tsui, and Cunningham [109]. The experimental observation

led to a number of theoretical investigations, all of which confirmed that the mechanism of optical phonon scattering could produce a small satellite peak or shoulder to the main resonant peak in the I-V characteristic in the region of the valley current [9, 10, 13, 21, 33, 110-112]. The initial work of Goldman, Tsui, and Cunningham was followed by several experimental studies of resonant tunneling in a longitudinal, $B \parallel J$, magnetic field [113-116] which showed evidence of phonon assisted tunneling of magnetopolarons from quantized Landau levels in the emitter [114-116]. A theoretical study followed which stressed the importance of phonon assisted tunneling as opposed to phonon coupling in the well for correctly explaining the magneto-tunneling data [18].

The experimental data shows evidence for both GaAs-like and AlAs-like LO phonons. Goldman et al. concluded that the phonon peak in their structure was due to electrons interacting with AlAs-like LO phonons in the $Al_{0.4}Ga_{0.6}As$ barrier [109]. Leadbeater et al. found evidence for both types of phonons in structures with 5 and 6 nm GaAs wells and evidence for only GaAs-like phonons in the structure with a 11.7 nm GaAs well. They hypothesized that the wavefunctions in the narrow quantum wells penetrated deeper into the $Al_{0.4}Ga_{0.6}As$ barriers enhancing the coupling with the AlAs-like modes [114]. Supporting data was provided by Boebinger et al. who found only a slight contribution from AlAs-like modes in a magneto-tunneling study of an AlAs - GaAs DBRTD with a 10 nm well [115].

Turley and Teitsworth [45-47, 117] have provided a credible answer to the question regarding the type of phonon responsible for the phonon peak by studying the matrix elements of the phonon modes using the phonon model of Mori and Ando [118] and the approach to transport of Chevoir and Vinter [13]. For narrow wells, the symmetric interface modes, which have the frequency of the bulk AlAs LO phonon, are the dominant scattering mechanism, while for wider wells, the confined modes in the well, which have the frequency of the bulk GaAs LO phonon provide the dominant scattering.

Experimental investigations of asymmetric DBRTDs have shown a strong effect of barrier asymmetry on the feature in the I-V curve that could be associated with the phonon peak. In fact, the feature is strongly enhanced with respect to the main peak in one bias direction [4, 104, 119, 120]. This observation has prompted our theoretical investigation of the effect of barrier asymmetry on the phonon peak. The structure we consider is shown in Fig. 4.1. We will analyze the effect of different collector barrier heights both numerically and analytically. Expressions for the current and occupation of the well are derived based on the non-equilibrium Green function approach of Keldysh, Kadanoff, and Baym [25, 48, 51, 69].

Büttiker showed that dephasing enhanced the off-resonant transmission coefficients and hence the off-resonant current [7,101]. Jauho showed that coherent inelastic transitions within the well enhanced the off resonant transmission [121]. Our process is a dephasing inelastic transition. We will show the effect of the dephasing and the inelastic transition on the off-resonant current enhancement.

4.3. Model

The microscopic model is described in Chapter 2. In these calculations, the Einstein delta function spectrum has been replaced by a normalized spectrum with a finite width of 4 meV. For simplicity of calculation, the shape of the spectrum was chosen to be rectangular. This replacement was found to be necessary for the following reason. Four different devices were modeled all with the same scattering strength U. The peak in the density of states at the resonant energy varies several orders of magnitude from the symmetric device to the most asymmetric device. For a true Einstein spectrum, $1/\tau_n(E) \propto N_0(E-\hbar\omega_0)$. Thus, the scattering rates one optical phonon energy above the resonance would vary by several orders of magnitude between the symmetric device and the most asymmetric device. This behavior seems unphysical and is due to the phonon spectrum being always sharper than the resonance. For the structures considered here, the intrinsic linewidth of the resonance ranges from 10 μeV to 1 meV. By giving the phonon spectrum a finite width, the maximum value of the scattering rates become relatively uniform from device to device.

Like Anda and Flores [33], the device we model is strictly one dimensional as opposed to the devices with infinite cross-sectional area. The structures modeled in refs. [9,10,21,111,112] are also effectively one dimensional since no attempt is made to include momentum transfer in the direction parallel to the direction of transport. There is one major reason for this choice. Since our scattering model is local, the resulting scattering is isotropic; all transverse energies are equally coupled. For a DBRTD of infinite cross section, the density of states in the well is a step function that turns on at the resonance. Since $1/\tau_n \propto N_0(E-\hbar\omega_0)$, the scattering rate due to optical phonon emission turns on one optical phonon energy above the resonance and stays on as shown in Fig. 2.5. This would result in a phonon step occurring in the valley current as opposed to a phonon peak. In narrow well structures, the dominant scattering from the symmetric interface modes favors small angles (see Fig. 2 of ref. [46]). Thus, the scattering rate in the well of a DBRTD due to polar optical phonons in a narrow well of infinite cross section more closely resembles the scattering rate

determined from local Einstein phonons for a strictly 1-D structure. Several papers do not neglect the momentum transfer in the direction parallel to the direction of transport [13, 45-47, 110, 117]. The results of these papers do not appear qualitatively different from the papers which do neglect the transverse momentum transfer [9, 10, 21, 111, 112].

We have chosen the strength, U, of the scattering to give a maximum scattering time of $\tau_\phi = 0.12$ ps. This corresponds to an imaginary part of the retarded self-energy, $\hbar/2\tau_\phi$, of 2.75 meV, slightly less than the value obtained by Anda and Flores of 4.4 meV (see Fig. 4 of ref. [33]).

4.4 Analytical Analysis

Within the local phonon model, the equation for the current in the contacts and the non-equilibrium occupation factor in the device can be combined into the following expression.

$$I(z;E) = \frac{e}{h} \int dz' T(z,z';E) \left[f(z;E) - f^\tau(z';E) \right] \tag{4.1}$$

where the quantities in (4.1) are defined as follows.

$$T(z,z';E) = \frac{\hbar^2 |G^R(z,z';E)|^2}{\tau_\phi(z;E)\tau_\phi(z';E)} \tag{4.2}$$

$$f^\tau = \frac{1/\tau_p(z;E)}{1/\tau_\phi(z;E)} \tag{4.3}$$

In equilibrium, or if the scattering is elastic dephasing, $f^\tau(z;E) = f(z;E)$. The current into the left (right) contact at each energy is

$$I_{L(R)}(E) = \int_{C_{L(R)}} dz\, I(z;E) \tag{4.4}$$

where $C_{L(R)}$ represents the region in the left (right) contact. In the device, $I(z;E) = 0$ which gives an expression for the non-equilibrium occupation factor, $f(z;E)$, identical to eq. (2.13). In the contacts, $f(z;E)$ is the Fermi-Dirac factor.

For the analytical analysis we consider a structure, Fig. 4.1, consisting of three regions, the emitter contact, E, the collector contact, C, and the well, W, where, in each region the occupation factor, $f(z;E)$, is independent of position. Transmission coefficients between the regions are defined as follows.

$$T_{E,C} = \int\limits_{z\in E} dz \int\limits_{z'\in C} dz' T(z,z';E) \qquad (4.5)$$

$$T_{E,W} = \int\limits_{z\in E} dz \int\limits_{z'\in W} dz' T(z,z';E) \qquad (4.6)$$

$$T_{C,W} = \int\limits_{z\in C} dz \int\limits_{z'\in W} dz' T(z,z';E) \qquad (4.7)$$

$$T_{W,W} = \int\limits_{z\in W} dz \int\limits_{z'\in W} dz' T(z,z';E) \qquad (4.8)$$

Since we are not considering magnetic fields, the transmission coefficients are symmetric.

With the above definitions, the current per unit energy in the emitter contact is

$$I_E = \frac{e}{h}\left[T_{E,C}(f_E - f_C) + T_{E,W}(f_E - f_W^\tau)\right] \qquad (4.9)$$

In the well, $I(z;E)$ is zero and (4.1) becomes

$$0 = T_{E,W}(f_W - f_E) + T_{C,W}(f_W - f_C) + T_{W,W}(f_W - f_W^\tau)$$

which gives a general expression for the occupation of the well.

$$f_W = \frac{T_{E,W}f_E + T_{C,W}f_C + T_{W,W}f_W^\tau}{T_{E,W} + T_{C,W} + T_{W,W}} \qquad (4.10)$$

Quantities in (4.9) and (4.10) are evaluated at a single energy. Equations (4.9) and (4.10) will be used to analyze the current and the occupation of the resonance at the bias of the phonon peak.

First, consider the case of elastic phase-breaking scattering in the well. For this case, $f_W^\tau = f_W$. Equations (4.9) and (4.10) yield

$$I_E = \frac{e}{h}\left[T_{E,C}(f_E - f_C) + \frac{T_{E,W}T_{C,W}}{T_{E,W} + T_{C,W}}(f_E - f_C)\right] \qquad (4.11)$$

and

$$f_W = \frac{T_{E,W}f_E + T_{C,W}f_C}{T_{E,W} + T_{C,W}} \qquad (4.12)$$

the coherent component of the current is given by the first term in (4.11) and the sequential component of the current is given by the second term.

For inelastic scattering, the emitter current per unit energy is given by (4.9). To evaluate I_E, we must evaluate f_W^τ at the incident energy. At the bias corresponding to

the phonon peak, the incident energy, E_i, is one optical phonon energy above the resonant energy, E_r. The quantity $1/\tau_p(E_i)$ in the well at a temperature of 4.2K is given by the second term in (2.32b) which is proportional to the electron density one optical phonon energy above the incident energy which is zero. $1/\tau_\phi(E_i)$ is given by the second term in (2.33a) which is proportional to the hole density at the resonance, $N_o(E_i-\hbar\omega_o)[1-f(E_i-\hbar\omega_0)]$, which is large. Thus, $f_W^\tau(E_i)=0$. The equation for the off-resonant emitter current per unit energy is then

$$I_E = \frac{e}{h}[\, T_{E,C}(f_E-f_C)+T_{E,W}f_E\,] \tag{4.13}$$

The coherent component of the current is given by the first term in (4.13) and the current in the optical phonon channel is given by the second term.

To obtain useful analytical expressions for the current in (4.11) and (4.13), we must evaluate the transmission coefficients. We have done so solving a one dimensional tight-binding model with the electron-phonon interaction at the n=0 site. The central site is coupled to the emitter (collector) lead via the hopping matrix element $W_{E(C)}$. The hopping matrix elements in the leads are identical and equal to W. The site energies in the emitter (collector) lead are $U_{E(C)}$ where U_E-U_C equals the applied voltage, $e|V|$. This model is similar to the one investigated by Hershfield *et al.* with the Hubbard U repulsion replaced by the electron phonon interaction [65]. In this model, the transmission coefficients are

$$T_{E,C} = \Gamma_E\Gamma_C\,|G^R(E)|^2 \tag{4.5a}$$

$$T_{E,W} = \Gamma_E\frac{\hbar}{\tau_\phi}\,|G^R(E)|^2 \tag{4.6a}$$

$$T_{C,W} = \Gamma_C\frac{\hbar}{\tau_\phi}\,|G^R(E)|^2 \tag{4.7a}$$

$$T_{W,W} = \left[\frac{\hbar}{\tau_\phi}\right]^2\,|G^R(E)|^2 \tag{4.8a}$$

where $\Gamma_{E(C)}$ is $\hbar$ times the rate of tunneling from the emitter (collector) lead to the central site [122] and $G^R(E)=[\,(E-E_r)+\frac{i}{2}(\Gamma_E+\Gamma_C+\hbar/\tau_\phi)\,]^{-1}$ is the retarded Green function on the resonant site where E_r is the renormalized resonant energy.

Re-arranging (4.9) and using the transmission coefficients from the tight binding model, we derive a general expression for the emitter current per unit energy and the occupation of the central site.

$$I_E = \frac{e}{h}\frac{\Gamma_E\Gamma_C}{\Gamma_E+\Gamma_C}A(E)\,[f_E-f_C] - \frac{\Gamma_E}{\Gamma_E+\Gamma_C}\mathbf{V}\cdot\mathbf{J} \qquad (4.14)$$

and

$$f_W = \frac{\Gamma_E f_E + \Gamma_C f_C + \hbar/\tau_p}{\Gamma_E + \Gamma_C + \hbar/\tau_\phi} \qquad (4.15)$$

where

$$A(E) = -2\,\mathrm{Im}\,G^R(E) = \frac{\Gamma_E + \Gamma_C + \hbar/\tau_\phi}{(E-E_r)^2 + \frac{1}{4}(\Gamma_E + \Gamma_C + \hbar/\tau_\phi)^2} \qquad (4.16)$$

is the spectral function of the central site and

$$\mathbf{V}\cdot\mathbf{J}(E) = e\left(\frac{p(E)}{\tau_p(E)} - \frac{n(E)}{\tau_n(E)}\right)$$

is the divergence of the current density per unit energy at the central site [123]. The energy dependence of $\Gamma_{E(C)}$, τ_p and τ_ϕ is understood. The first term in (4.14) is the component of the current that tunnels elastically, not necessarily coherently, through the central site. The second term in (4.14) is the component of the current that suffers inelastic transitions at the central site. This is the current in the optical-phonon channel.

At resonance, the first term of (4.14) determines the current. Integrating over the energy of the incident flux, assuming that the spectral function is sharply peaked compared to the Γ's, the total resonant current is

$$I_{res} = \frac{e}{h}\frac{2\pi\Gamma_E\Gamma_C}{\Gamma_E+\Gamma_C} \qquad (4.17)$$

where the Γ's are evaluated at the resonant energy.

At the bias corresponding to the phonon peak, for elastic scattering, (4.14) reduces to

$$I_E(E_i) = \frac{e}{h}\frac{1}{(\hbar\omega_o)^2}\Gamma_E\Gamma_C + \frac{e}{h}\frac{\hbar/\tau_\phi}{(\hbar\omega_o)^2}\frac{\Gamma_E\Gamma_C}{\Gamma_E+\Gamma_C} \qquad (4.18a)$$

and for optical phonon scattering to

$$I_E(E_i) = \frac{e}{h}\frac{1}{(\hbar\omega_o)^2}\left[\Gamma_E\Gamma_C + \Gamma_E\,\hbar/\tau_\phi\right] \qquad (4.18b)$$

where we have assumed that $\frac{1}{4}(\Gamma_E+\Gamma_C+\hbar/\tau_\phi)^2 \ll (\hbar\omega_o)^2$, $f_E = 1$, and $f_C = 0$. All

quantities in (4.17) are evaluated at the incident energy, E_i. The first term in (4.18a,b) gives the coherent component of the current. The second term in (4.18a) gives the sequential component of the current and the second term in (4.18b) gives the inelastic component of the current.

The second term in (4.18b) shows that the current in the optical phonon channel is independent of the coupling to the collector lead at the incident energy. The current in the inelastic channel does depend, through the effect of the factor of $[1-f(E_r)]$ on the value of $1/\tau_\phi(E_i)$, on the coupling to the collector at the resonant energy.

To understand the effect of the various rates on the occupation of the central site, we consider (4.15) at the incident energy and at the resonant energy. Since we are interested in asymmetric barriers, let us assume that $\Gamma_C \ll \Gamma_E$. Furthermore, since we are considering low temperature and high bias, we take $f_E = 1$ and $f_C = 0$. Then we find that at the incident energy

$$f_W(E_i) = \frac{1}{\dfrac{\hbar/\tau_\phi(E_i)}{\Gamma_E(E_i)} + 1} \tag{4.19a}$$

and at the resonant energy

$$f_W(E_r) = \frac{1}{\dfrac{\Gamma_C(E_r)}{\hbar/\tau_\phi(E_r)} + 1} \tag{4.19b}$$

where we have used $1/\tau_p(E_i) = 0$, $1/\tau_p(E_r) = 1/\tau_\phi(E_r)$, and $\Gamma_E(E_r) = 0$ (since the resonant energy is below the emitter conduction band). In both (4.19a) and (4.19b), the fraction in the denominator represents the ratio of the outscattering rate to the inscattering rate at that energy.

As an example, assume the occupation of the central site is $1/2$ at both the incident and resonant energies. Then

$$\Gamma_E(E_i) = \hbar/\tau_\phi(E_i) = \pi U^2 N_o(E_r)$$

and

$$\Gamma_C(E_r) = \hbar/\tau_\phi(E_r) = \pi U^2 N_o(E_i)$$

Taking the ratio, we find

$$\Gamma_C(E_r) = \frac{N_o(E_i)}{N_o(E_r)} \Gamma_E(E_i) \tag{4.20}$$

Since the ratio $N_o(E_i)/N_o(E_r)$ is small, $\Gamma_C(E_r) \ll \Gamma_E(E_i)$. The condition for significant filling of the well to occur at the phonon peak is that the ratio

$$\frac{\Gamma_C(E_r)}{\Gamma_E(E_i)} \sim \frac{N_o(E_i)}{N_o(E_r)} \tag{4.21}$$

For structures we consider, the decrease in Γ_C from the incident energy to the resonant energy is a factor of at most 2.0. At a bias, corresponding to the main resonant peak, the condition for half-filling the resonance is $\Gamma_E(E_r) = \Gamma_C(E_r)$. Thus, (4.21) shows that to cause significant filling of the resonance at the bias corresponding to the phonon peak considerably more asymmetry is necessary than that necessary to cause filling at the bias corresponding to the main resonant peak.

4.5. Results and Discussion

4.5.1. I-V Characteristics

In this section we present I-V characteristics calculated numerically using the non-equilibrium Green function approach, for asymmetric devices, and we explain the various attributes using the analytical results. The I-V characteristic of the DBRTD with barriers of 220 meV and 500 meV is shown in Fig. 4.2. The coherent and incoherent components of the total current are also shown. The coherent current is that part of the current that traverses the device coherently. The incoherent current component is the part of the current that has suffered a dephasing event in transit. The method of separating the current into its coherent and incoherent parts is described in section 2.3.4. Data points at the main peak, the phonon peak, and on either side of the phonon peak are shown for the current calculated with elastic de-phasing scattering instead of optical phonon scattering. The elastic-dephasing rate in each region, contact, lead, barrier, and well, is chosen to be energy independent with a value given by the maximum value of the optical phonon scattering rate in that region at that bias. The method of introducing elastic dephasing is described in section 2.3.5. The left barrier is 220 meV and the right barrier is 500 meV. Other parameters are given in Fig. 4.1. Forward bias is such that the 500 meV barrier is the collector barrier as shown in Fig. 4.1. The current is essentially totally coherent except at the phonon peak.

To compare the results of the numerical simulations with the analytical expressions derived from the tight binding model, we need expressions for $\Gamma_{E(C)}$ in terms of parameters related to the actual tunnel barriers. We will use
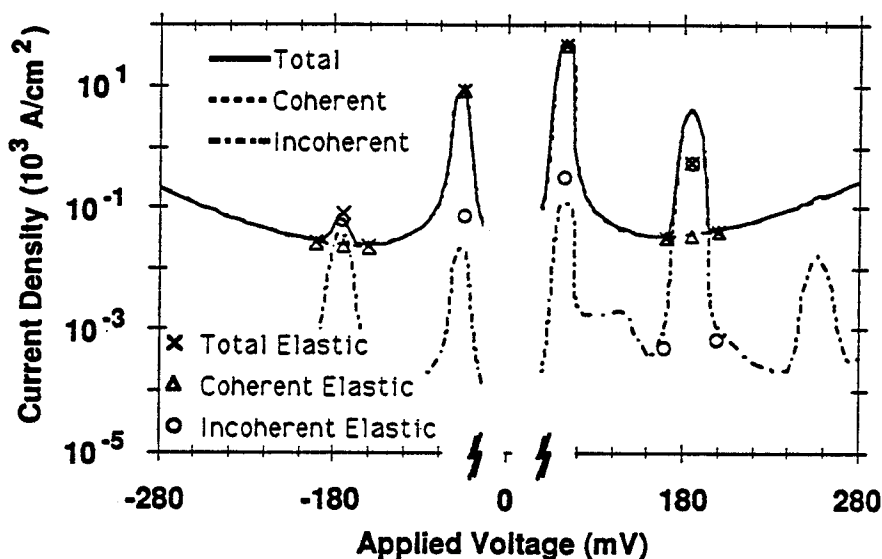
Figure 4.2. I-V characteristic of an asymmetric structure. The coherent and incoherent components of the total current are also shown. Data points at the main peak, the phonon peak, and on either side of the phonon peak are shown for the current calculated with elastic de-phasing scattering instead of optical phonon scattering. The elastic-dephasing rate in each region, contact, lead, barrier, and well, is chosen to be energy independent with a value given by the maximum value of the optical phonon scattering rate in that region at that bias. The left barrier is 220 meV and the right barrier is 500 meV. The temperature, effective mass, and emitter Fermi energy are as described in Fig. 4.1.

$$\Gamma_{E(C)} = \hbar v T_{E(C)}$$

where $v = (\hbar k/m^*)/2d$ is the attempt frequency in the well, d is the well width, and $T_{E(C)}$ is the transmission coefficient through the emitter (collector) barrier. This relation arises naturally from an exact calculation of the transmission coefficient near resonance of a DBRTD. To calculate the total off-resonant current from (4.18a,b) we integrate the coherent and sequential components over the width of the emitter Fermi sea, and we integrate the inelastic component over the width of the optical phonon dispersion, 4 meV.

The ratio of the peak currents in forward and reverse bias for the main resonant peak and the phonon peak are compared to the predictions from eqs. (4.17) and (4.18b). First, consider the resonant peak current. The ratio from the simulation is 5.6 and from eq. (4.17), 5.2. The main impediment to current flow is the 500 meV barrier. We rewrite (4.17) in terms of $\Gamma_{220(500)}$, the rate corresponding to the 220 (500) meV barrier.

$$I_{res} = \frac{e}{h} \frac{2\pi\Gamma_{220}\Gamma_{500}}{\Gamma_{220} + \Gamma_{500}}$$

Γ_{500} is an order of magnitude less than Γ_{220}. Thus, $I_{res} \approx e\Gamma_{500}$. In the forward bias configuration, the effective height of the 500 meV barrier is less than it is in the reverse bias direction. Since transmission goes as $\exp(-2\kappa d)$ where κ is proportional to the square root of the effective barrier height, a larger forward bias peak current is indicated.

The ratio of the phonon peak in forward bias to the phonon peak in reverse bias is 65 from the numerical simulation and 51 from eq. (4.18b). Considering the optical phonon channel, the second term in (4.18b), $\hbar/\tau_\phi$ is the same at forward and reverse bias. The difference arises from Γ_E. In forward bias, $\Gamma_E = \Gamma_{220}$. In reverse bias, $\Gamma_E = \Gamma_{500}$. Thus, the ratio of the forward bias to reverse bias current in the optical phonon channel is $\sim \Gamma_{220}/\Gamma_{500}$ which is large.

We note that in forward bias, the current at the phonon peak due to optical phonon scattering is greater than that due to elastic dephasing scattering. This point will be explored further in the discussion of Fig. 4.4b below.

I-V curves of four different devices of varying degrees of asymmetry are shown in Fig. 4.3. The corresponding structures are shown in Fig. 4.1. The solid line is from a symmetric structure. The short dotted line is for the 220/500 structure, the same structure as in Fig. 4.2. There are a number of interesting effects of barrier asymmetry displayed in Fig. 4.3.

The first trend to consider is the effect of asymmetry on the magnitude of the main peak current. The physics is the same as described above for Fig. 4.2. A plot of the peak current, normalized to the value of the peak current for the symmetric structure, is shown in Fig. 4.4a. The ratio of the normalization factors for the curve resulting from the numerical simulation and the curve resulting from Eq. (4.17) is 1.2. The results of Eq. (4.17) run parallel to those from the simulation but are a factor of 1.2 lower.

The most interesting trend is the effect of asymmetry on the phonon peak current in forward bias. A plot of the phonon peak current normalized to the value of the symmetric structure is shown in Fig. 4.4b. In forward bias, the magnitude of the peak is unaffected by the collector barrier height. This is expected from Eq. (4.18b). Except for the symmetric structure, the coherent component of the current at the phonon peak is negligible. Since $\hbar/\tau_\phi$ is essentially independent of the barrier heights for the range of parameters used here, (filling of the resonance at the phonon peak current is negligible) and Γ_E is fixed to Γ_{220} in the forward bias direction, the optical phonon channel is independent of the collector barrier height. Thus, the apparent enhancement of the phonon peak in forward bias in asymmetric structures is due to a reduction of the main peak combined with an insensitivity of the phonon peak to the size of the collector barrier.

Fig. 4.4b also shows the effect of barrier asymmetry on enhanced off-resonant transmission due to elastic dephasing scattering. The elastic de-phasing rate in the well is energy independent and set equal to the maximum optical phonon scattering rate in the well for the corresponding device and bias. Eq. (4.18a) is compared with the numerical results. Sequential tunneling does depend strongly on the collector barrier. In reverse bias, transmission is determined by $\Gamma_E \ll \Gamma_C$ so both (4.18a) and (4.18b) reduce to $I_{offres} = \dfrac{e}{h} \dfrac{\hbar/\tau_\phi}{(\hbar\omega_o)^2}\Gamma_E$ so that the four bottom lines in Fig. 4.4b lie together.

The normalized ratio of the phonon peak current to the main peak current is shown in Fig. 4.4c. In forward bias, the ratio is enhanced as the collector barrier becomes larger as discussed above. In reverse bias, the ratio is only slightly affected by increasing the emitter barrier height since $I_{res} = e/h\, 2\pi\Gamma_E$ for $\Gamma_E \ll \Gamma_C$.

The effect of the right barrier height in forward bias on the filling of the resonance at the main resonant peak current and the phonon peak current is shown in Fig. 4.5. The occupation has been calculated numerically for the structures described above and also for structures with left barriers of 220 meV and right barriers of 600, 700, and 1000 meV. The occupation at resonance is plotted versus the ratio

$\Gamma_E(E_r)/\Gamma_C(E_r)$ and the occupation at the phonon peak is plotted versus the ratio $\Gamma_E(E_i)/\Gamma_C(E_r)$. At resonance, the occupation becomes significant (.45) for the 220/300 structure. At the phonon peak, the occupation only becomes significant (.31) for the 220/700 structure. The difference between the filling at resonance and at the phonon peak is in agreement with the discussion of eq. (4.20).

4.5.2. Microscopic Quantities

In this section, we present cross-sections taken from the center of the well at the forward bias phonon peak for the most asymmetric structure of Fig. 4.1 of the density-of-states $(N_o(z;E) = -1/\pi \, ImG^R(z,z;E)\,)$, the occupation, $f(z;E)$, of N_o, and the optical phonon scattering time, $\tau_\phi(z;E)$, where, in the above quantities, z is the spatial point at the well center. We also show, on a gray scale plot superposed over the conduction band profile, the energy distribution of the current density, $J(z;E)$, which shows the current "flow" [98] through space and energy.

The density of states at the well center is plotted in Fig. 4.6a. The main peak is the resonance. The peak at 0 meV occurs at the incident energy one optical phonon energy above the resonance. The peak is caused by an enhancement of the imaginary part of the retarded self energy, $\hbar/2\tau_\phi$. The enhancement is due to optical phonon emission by electrons corresponding to the second term in Eq. (2.32a). The step that also occurs in N_o at 0 meV is not due to an effect of the self energy but is due to coupling through the small emitter barrier of the well to the continuum states in the emitter. The peak 36 meV below the resonance is caused by an enhancement of $\hbar/2\tau_\phi$ due to optical phonon emission by holes corresponding to the second term in Eq. (2.32b).

The scattering time, τ_ϕ, is plotted in Fig. 4.6b. The peak at 0 meV corresponds to the incident energy. The peak at 40 meV lies two optical phonon energies above the resonance. The peaks near -70 and -100 meV lie one and two optical phonon energies below the resonance respectively. The small structure around the resonance, at ~ −35meV, is due to the Debye phonon scattering.

The occupation, $f(E)$, is shown in Fig. 4.6c. At the incident energy, 0 meV, where the scattering rate, $1/\tau_\phi$, is large, the occupation is depleted. The occupation in the depleted region between the two spikes is ~ 0.08. Electrons are being removed from the incident energy and scattered down to the resonant energy. The occupation of the resonance due to electrons being scattered down from the incident energy is ~ 0.05. Further optical phonon emission causes filling of the exponentially vanishing states below the resonance.
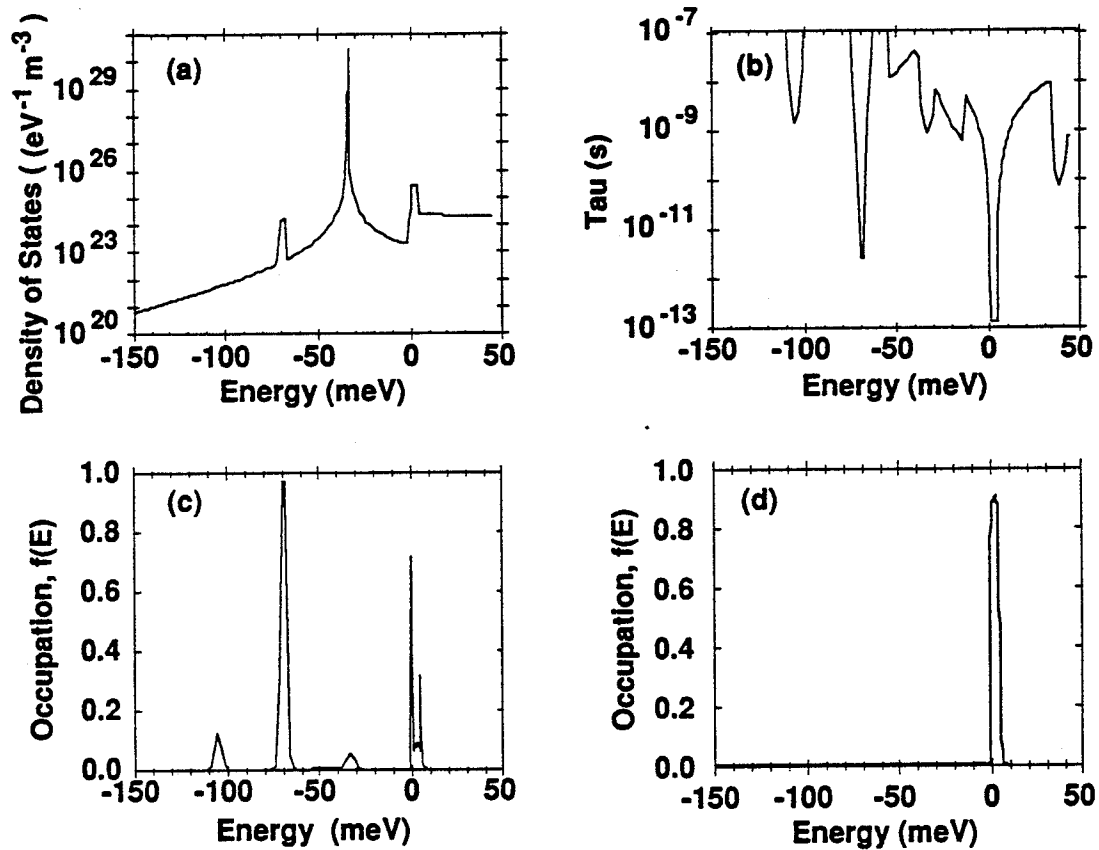
Figure 4.6.   Cross sections taken from the center of the well at the forward bias phonon peak of the most asymmetric structure (corresponding to Fig. 4.3) of (a) density of states, (b) optical phonon scattering time, and (c) occupation of states. Fig. 4.6d is the occupation of the well for the case of elastic dephasing.

The occupation, f(E), for the case of elastic de-phasing for the same bias and structure of Fig. 4.6c is shown in Fig. 4.6d. Since the scattering is elastic, all energies below the incident energy are unoccupied. The occupation of the incident energy is ~0.9.

A conduction band profile of the most asymmetric structure with optical phonon scattering superposed on a gray-scale plot of the energy distribution of the current density, J(z;E), is shown in Fig. 4.7. This is the same structure from which the values of N_o, f, and τ are extracted in Figs. 4.6a-c, and it is the same structure for which the I-V characteristic is shown in Fig. 4.2. Fig. 4.7a corresponds to the forward bias point immediately before the onset of the phonon peak; Fig. 4.7b corresponds to the forward bias point at the center of the phonon peak; and Fig. 4.7c corresponds to the reverse bias point at the center of the phonon peak. Dark regions of the shadow plot correspond to regions of high current density. Immediately before the phonon peak, current comes off of the emitter conduction band and tunnels through the double barrier structure at the incident energy. At the forward bias phonon peak, none of the current crosses the collector barrier at the incident energy. All of the current is flowing through the optical phonon channel and tunneling out through the collector barrier at the resonant energy. Note that the optical phonon emission begins before the well region. At the reverse bias phonon peak, half of the current is passing through the collector barrier at the incident energy and half of the current is passing through the collector barrier at the resonant energy. We note that in these simulations, current is conserved across the entire device at all bias points to within 0.5%.

Since we have electron-phonon coupling throughout our device-contact system, and Fig. 4.7 shows that the optical phonon emission begins before the emitter barrier, the question is again raised of the relative effects of phonon assisted tunneling versus phonon coupling in the well. In our local interaction model, the scattering rate at any spatial point is proportional to the final density of states. Thus, the scattering is greatest in the well, and greatly suppressed in the barriers. Most of the scattering is occurring in the well. When using a local interaction for the electron-phonon coupling, the scattering in the well is dominant.

4.6. Summary and Conclusion

The effect of barrier asymmetry on the phonon peak is investigated numerically, solving a model Hamiltonian using the non-equilibrium Green function formalism. The electron-phonon interaction is modeled using dispersionless Einstein phonons which interact with the electrons locally. Phonons are present throughout the
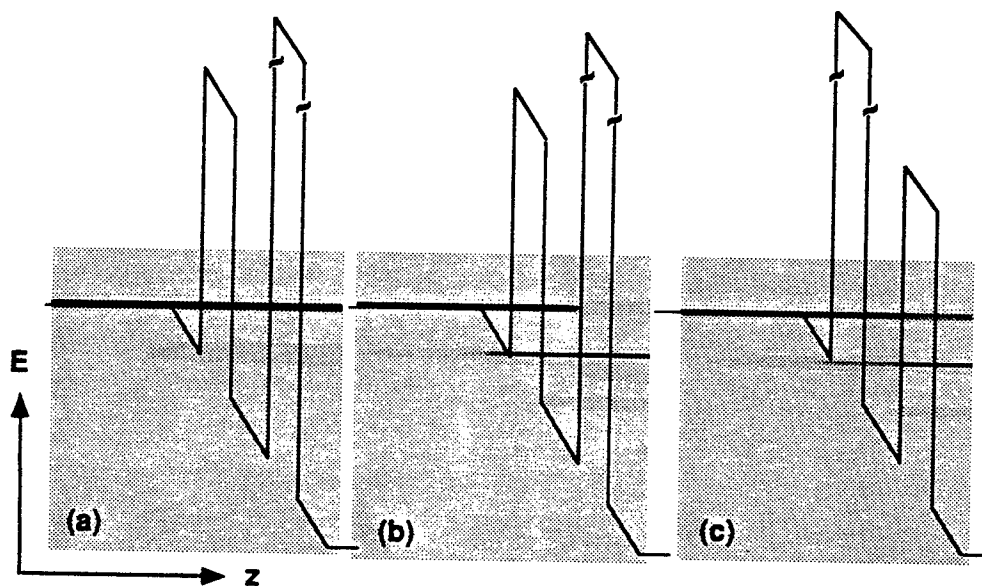
Figure 4.7.   A conduction band profile of the most asymmetric structure (corresponding to Figs. 4.2 and 4.6a-c) with optical phonon scattering superposed on a gray-scale plot of the energy distribution of the current density, J(z;E). (a) Forward bias immediately prior to the phonon peak, (b) Forward bias at the phonon peak. (c) Reverse bias at the phonon peak.

contacts, leads, and device. The numerical results are analyzed using analytical expressions derived from the Keldysh formalism in a tight binding model. All of the trends from the numerical simulations are matched well by the results of the analytical expressions. An analysis of the relative effects of elastic dephasing versus optical phonon scattering on enhancing the valley current is made both numerically and analytically. For equal scattering rates, the optical phonon scattering is found to give greater current enhancement. It is shown that considerably more barrier asymmetry is necessary to cause significant filling of the resonance at the phonon peak bias than at the resonant peak bias. Within our local phonon model, the phonon peak is only affected by a larger collector barrier via the exclusion principle in the calculation of the scattering rate. The ratio of the phonon peak to the main peak is enhanced due to a reduction of the main peak with increasing collector barrier height.

CHAPTER 5
ENERGY BALANCE AND HEAT EXCHANGE IN
MESOSCOPIC SYSTEMS

5.1. Abstract

The spatial distribution of the power transferred from the electrons to the phonon bath is calculated for several mesoscopic structures using the non-equilibrium Green's function formalism. At low bias, the local power transfer between the electrons and the phonon bath can be separated into a component that is linear in the applied bias and a component that goes quadratically with bias. The linear component represents the thermoelectric heat which can be locally positive or negative while the quadratic component represents the Joule heating which is positive everywhere. The numerical calculations presented in this paper are based on a local phonon model. However, the basic formulation is quite general. Energy balance equations are derived in the absence of magnetic fields for systems with local or non-local electron-phonon interactions.

5.2. Introduction

The spatial variation of the electrochemical and electrostatic potentials in mesoscopic systems has been discussed by several authors [72, 84, 86, 124-130]. The electrochemical potential is not a well defined thermodynamic concept on a mesoscopic length scale, but the energy distribution of the electrons has nearly a Fermi-Dirac form if the bias is small and one can define a local electrochemical potential μ, at least approximately, from the energy distribution of the carriers [72]. It has been shown that the electrochemical potential, μ, drops sharply across an obstacle while the electrostatic potential changes more gradually over a screening length. Although $d\mu/dz$ is large at the location of the obstacle, energy is not necessarily dissipated at the obstacle. This is apparent since a scatterer may not have the internal degree of freedom essential for dissipating energy. A natural question to ask is, 'Where does the power loss occur?' [51, 98, 131]

Our objective in this paper is to study this question using several numerical examples. The numerical calculations are based on the non-equilibrium Green's Function formalism [25,48] using a local phonon model [51,69]. Although the details could change with extended phonons, the basic physics seems more general. The examples presented in this paper mainly involve one dimensional structures under low bias. However, we also discuss a resonant tunneling diode of infinite cross section under high bias.

5.3. Energy Current and Power Density

We solve for the particle current density per unit energy, $J_N(z;E)$, as described in chapter 2.

$$J_N(z;E) = \frac{-\hbar}{4\pi m^*} \lim_{z' \to z} [\, (\nabla - \nabla') G^<(z,z';E) \,]$$

and calculate the energy current

$$J_E(z) = \int dE \, E \, J_N(z;E), \tag{5.1}$$

and the power transferred,

$$P(z) = -\frac{d}{dz} J_E(z) \tag{5.2}$$

from the electrons to the phonon bath throughout the device. $P(z)$ contains the self-energy terms representing the transfer of energy due to electron-phonon scattering. In our local scattering model, $P(z)$ can be written in a physically transparent form (with the position coordinate suppressed)

$$P = -2\pi \int dE \int d(\hbar\omega) \, \hbar\omega \left\{ F(\hbar\omega) \, N_o(E) \, N_o(E+\hbar\omega) \, f(E) \, [\, 1 - f(E+\hbar\omega)] \right\} \tag{5.3}$$

which can be understood as follows. The quantity in curly brackets tells us the rate of transitions from E to E+$\hbar\omega$. Each such transition leads to an exchange of energy $\hbar\omega$. Eqs. (5.1)-(5.3) seem physically reasonable. However, one might question the limits of their validity. For this reason we have included a formal derivation for arbitrary electron-phonon interactions (see Appendix D). We have not considered electron-electron interactions.

It will be noted that E is the *total* energy, kinetic plus potential, and (5.3) is identical to the usual expression for power density derived from the Boltzmann equation (cf. eq. (7.39) of [91]),

$$P(z) = -\frac{d}{dz} J_{E_k}(z) + \mathcal{E}(z) \cdot J(z)$$

where J_{E_k} is the kinetic energy current, $\mathcal{E}$ is the electric field, and J is the current density. The power density can also be written as

$$P(z) = -J_N \, d\mu_J / dz \tag{5.4}$$

where the average energy of the current density, μ_J is

$$\mu_J(z) = \frac{J_E(z)}{J_N} = \frac{\int dE \, E \, J(z;E)}{\int dE \, J(z;E)} \tag{5.5}$$

and the particle current density, J_N, is independent of position due to current conservation. Equation (5.4) provides an intuitive way of understanding the spatial distribution of power transfer. To calculate the net power transferred from the electronic system to the phonon bath in a given region, simply multiply the net drop in μ_J across the region by the electron current, J_N.

In the low bias examples discussed in this chapter, we find that the occupation factor, $f(z;E)$, calculated from (2.13) is well described by a Fermi-Dirac function with a local $\mu(z)$. We deduce a value for $\mu(z)$ from the expression $\mu(z) = \int dE \, E \, (-\partial f(z;E)/\partial E)$.

Note that while the electrochemical potential, μ, is related to the average energy of the carriers, the 'current potential,' μ_J, defined above, tells us the average energy of the current. In a homogeneous resistor, the two are parallel, that is, $d\mu_J / dz = d\mu / dz$. Consequently, the power dissipation can be deduced from the slope of either μ or μ_J. But in mesoscopic systems, μ_J can deviate significantly from μ, and the total power dissipation is related directly to $\dfrac{d\mu_J}{dz}$; however, it has no simple relation to $d\mu / dz$.

5.4. Thermoelectric and Joule Components

Under low bias conditions, we expect $P(z)$ to have a component linear in the applied bias, $\Delta\mu$, which is the thermoelectric component, P_{TE}, and a component quadratic in the applied bias which is the Joule component, P_J.

$$P(z) = \alpha(z)(\Delta\mu) + \beta(z)(\Delta\mu)^2 = P_{TE}(z) + P_J(z) \tag{5.6}$$

We identify the two components by separating the calculated $P(z)$ into a part that is anti-symmetric, $P_A(z)$, and a part that is symmetric, $P_S(z)$, in the applied bias,

$$P_A(z) = \left\{ P(z)\big|_{+\Delta\mu} - P(z)\big|_{-\Delta\mu} \right\} / 2 \qquad (5.7a)$$

$$P_S(z) = \left\{ P(z)\big|_{+\Delta\mu} + P(z)\big|_{-\Delta\mu} \right\} / 2 \qquad (5.7b)$$

At low bias, we find that $P_A \propto \Delta\mu$ while $P_S \propto (\Delta\mu)^2$ in agreement with (11).

5.5. Homogeneous Resistor

For a strictly one dimensional homogeneous resistor, we can calculate the difference $\mu_J - \mu$ analytically starting from the Boltzmann equation in the relaxation time approximation. Assuming a relaxation time which varies slowly on the order of $\partial f_o / \partial E$, we obtain

$$\pi_o = \mu_J - \mu = \frac{\displaystyle\int_0^\infty dE\, E^{3/2}\, \frac{-\partial f_o}{\partial E}}{\displaystyle\int_0^\infty dE\, E^{1/2}\, \frac{-\partial f_o}{\partial E}} - \mu \qquad (5.8)$$

where all energies are measured from the bottom of the conduction band, and f_o is the Fermi-Dirac factor. The quantity π_o is simply the Peltier coefficient (see section 2.3.7). Using the Sommerfeld expansion, (5.8) can be simplified to yield

$$\pi_o \simeq \frac{\pi^2}{6} \frac{(k_B T)^2}{\mu} \qquad (5.9)$$

In Fig. 5.1, we show the numerical results for a homogeneous 1-D resistor at a temperature of 100K and an electrochemical potential 50 meV above E_c. A bias of one $k_B T$ is applied across the resistor. Both μ and μ_J are plotted as a function of position. The difference, $\mu_J - \mu$ is found to be 2.5 meV in agreement with Eq. (14). We have performed calculations with different values of the temperature and the electrochemical potential and we find that the values of π_o obtained from the simulations compare well with (5.9).

Fig. 5.1 shows a a downward slope in μ_J near the contacts; we feel that there is no physical significance to this. As described in section 2.3.1, the equilibrium boundary condition imposed on $f(z;E)$ in (2.13) imply zero current flow deep inside the contacts, so that μ_J is undefined within the contacts giving rise to unphysical behavior near the contact regions. For this reason, we have ignored the regions near
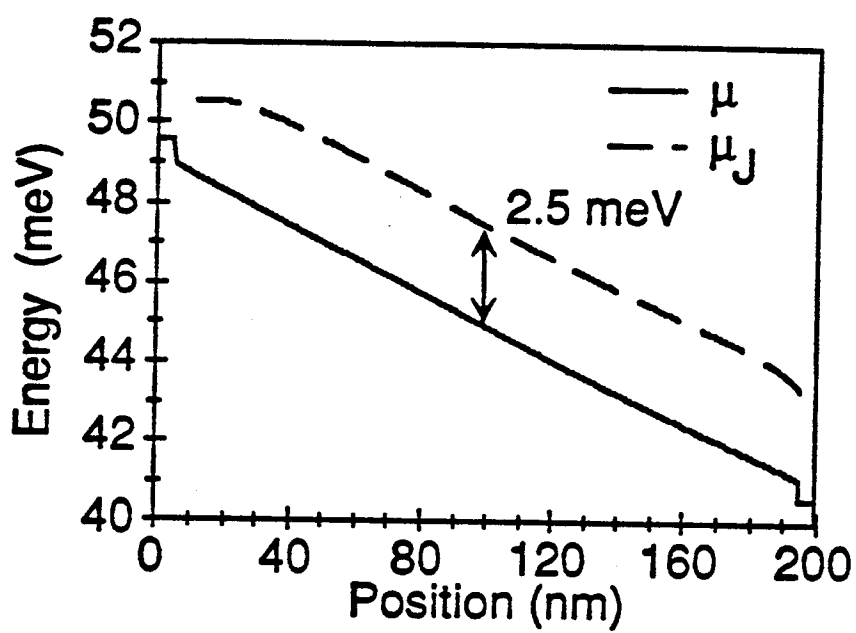
Figure 5.1   Average energy of the current density, μ_J, and electro-chemical potential, μ, for a straight wire with an applied bias of 1 $k_B T/e$ where T=100K.

the contacts in Figs. 5.2-5.5.

5.6. Tunneling Current Through a Thin Tall Barrier

In Fig. 5.2a, we show μ_J and μ calculated for a tunneling barrier of width 5 nm and height 190 meV (22 k_BT) above the Fermi energy of the emitter. Discussions of the potential drop and power dissipation in this structure have been given by Landauer [84, 98, 124]. On the emitter side, there is a slight rise in μ_J, indicating that the average energy of the current is slightly increasing. This is because the higher energies can tunnel more easily. The spatial distribution of the power density is plotted in Fig. 5.2b. The power loss occurs primarily on the collector side of the barrier.

More insight can be obtained by separating the components of the power density as explained earlier (see Eq. (5.7)). In Fig. 5.3a we have plotted the antisymmetric component of the power density divided by the applied bias for biases of 9 and 18 mV. In Fig. 5.3b, the symmetric component of the power density divided by the square of the applied bias is plotted for the same two biases. Clearly, the antisymmetric part, P_A, is linear in $\Delta\mu$ while the symmetric part, P_S, is quadratic in $\Delta\mu$. P_A represents the thermoelectric heat, P_{TE}, which is negative on the collector side and positive on the emitter side of the barrier. P_S represents the Joule heat, P_J, which is positive everywhere. We can show that $\int dz\,P_A(z) = 0$, which confirms the thermodynamic consistency of our approach. Thus, the total power dissipated arises solely from P_S and is positive definite.

5.7. Thermionic Current Over a Long Shallow Barrier

The thermoelectric effect can be illustrated more clearly by looking at a long shallow barrier such that the positive and negative components of P_{TE} are well separated spatially. Fig. 5.4 shows a 200nm long barrier with a height 1 k_BT above the Fermi-level of the emitter with an applied bias of 1 k_BT. The electro-chemical potential drops linearly across the barrier. However, μ_J rises approaching the emitter side of the barrier, runs parallel to the electro-chemical potential in the barrier region, and then falls sharply on the collector side of the barrier. The lattice is being cooled by the electron current on the emitter side and heated on the collector side.

This can be viewed as a classic Peltier effect which occurs when current is passed through materials with dissimilar Peltier coefficients placed in intimate contact [91]. The Peltier coefficient in the leads, π_L, is different from the Peltier coefficient in

Figure 5.2   (a) Conduction band edge, E_c, average energy of the current density, μ_J, and electro-chemical potential, μ, for a tunneling barrier of height 190 meV (22 $k_B T$) above the emitter Fermi-energy with an applied bias of 1 $k_B T/e$ where T = 100K. (b) Spatial distribution of the power density for the tunneling barrier. Vertical dashed lines represent the position of the barrier.
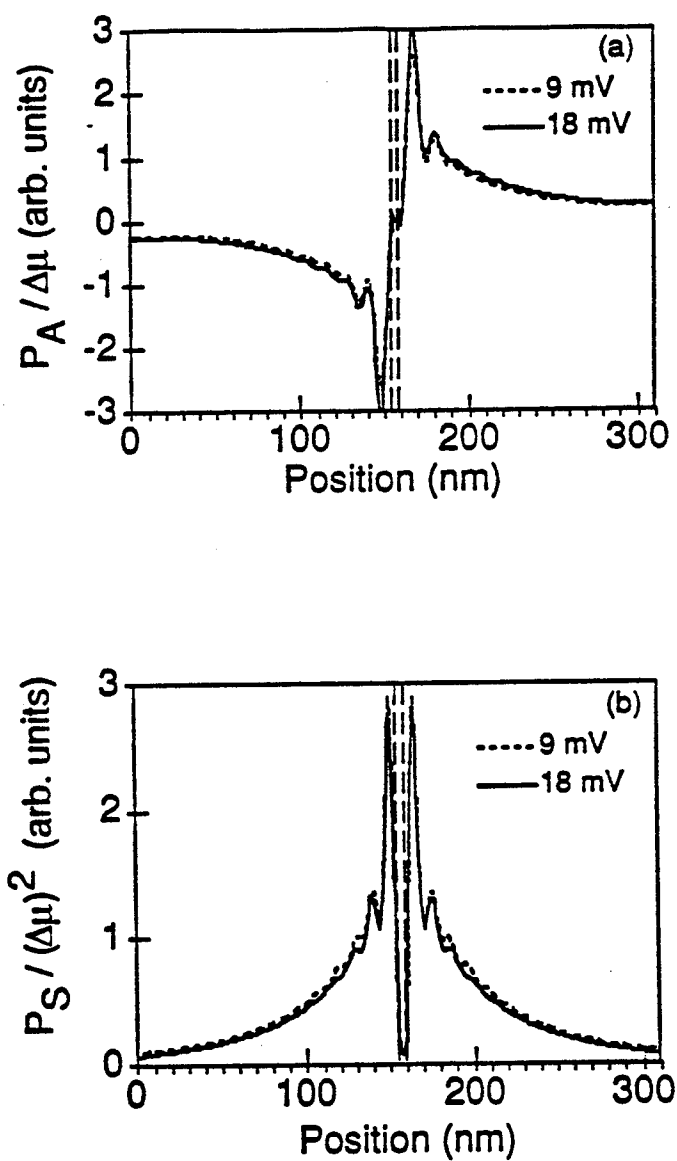
Figure 5.3   (a) Linear component of the power density of Fig. 2b divided by the applied bias for biases of 9 and 18 mV. Vertical dashed lines represent the position of the barrier. (b) Quadratic component of the power density of Fig. 2b divided by the square of the applied bias for biases of 9 and 18 mV. Vertical dashed lines represent the position of the barrier.

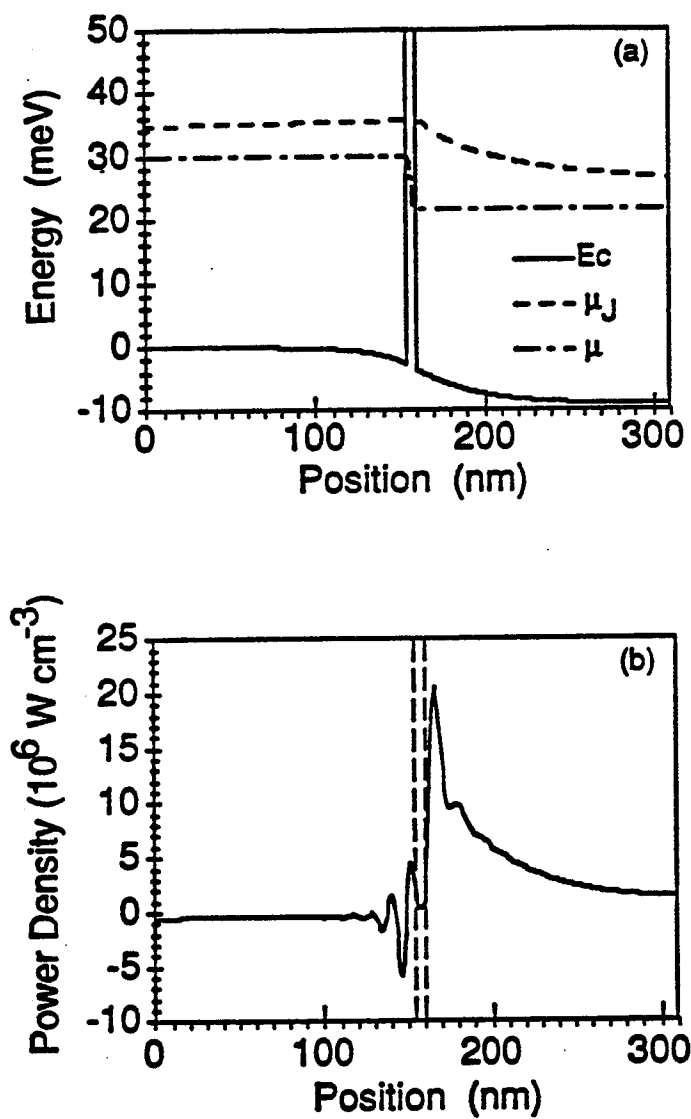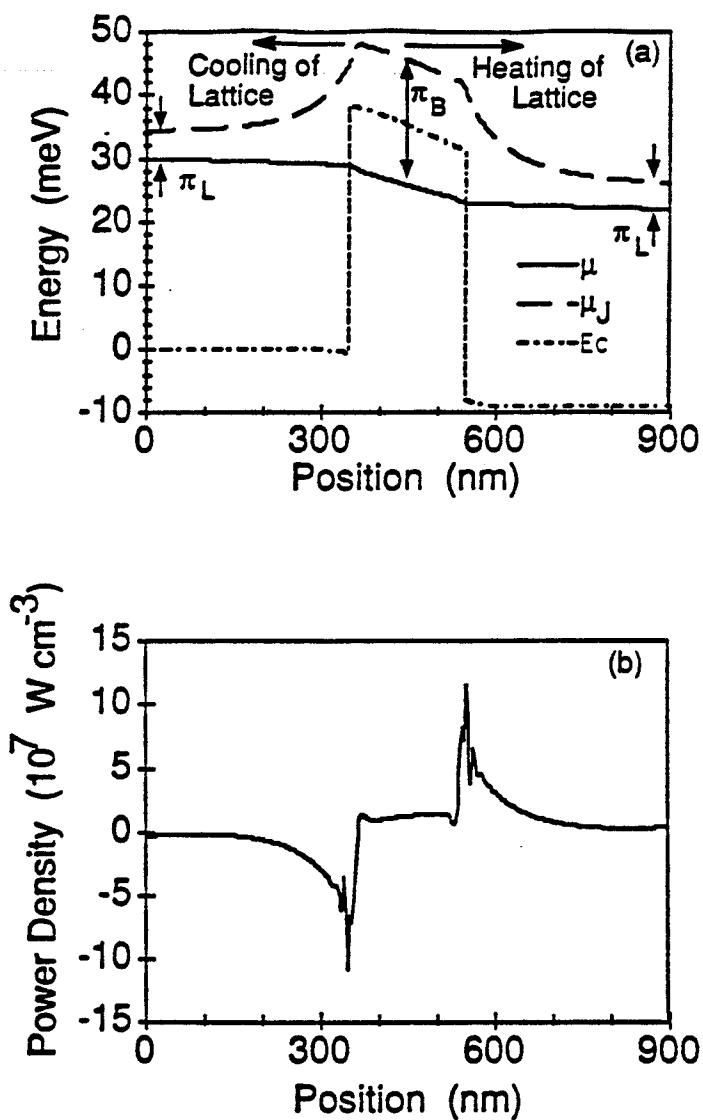Figure 5.4   (a) Conduction band, E_c, average energy of the current density, μ_J, and electro-chemical potential, μ, for a long, low barrier with a height 1 $k_B T$ above the Fermi energy of the emitter. A bias is applied of 1 $k_B T/e$. T = 100K. (b) Spatial distribution of the power density for the long barrier structure of (a).

the barrier, π_B. Thus, far from the barrier, μ_J lies at an energy π_L above the quasi-Fermi level in the leads, while in the barrier region, it is π_B above the quasi-Fermi level. The numerical result (Fig. 5.4a) gives a value for μ_J of 10.4 meV above the conduction band of the barrier in reasonable agreement with the value of 13 meV obtained from (5.8). This example also illustrates the role of vertical flow when the transmission characteristics show significant variation over the energy range where transport occurs [98, 132-135].

5.8. Double Barrier Resonant Tunneling

The previous examples have been of strictly 1-D structures under low bias, $V_a \sim k_B T$. However, the concepts are more general. In the final figure, Fig. 5.5, we show how μ_J drops and where the power is dissipated in a double barrier resonant tunneling device of infinite cross section under high bias. The bias is 135 mV, the chemical potential of the contacts is 50 meV, and the resonant level is 18.5 meV on the energy scale of Fig. 5.5a. A large peak in the power density occurs in the well due to electrons losing their transverse energy. However, the majority of the power density is distributed in the collector lead. The percent of the total IxV power dissipated between the barriers is the ratio of the drop in μ_J in the well to the total drop, 135 meV. Thus, it is clear from the figure that only a small fraction, 6%, of the total IxV loss occurs in the well. We note that due to computational limitations, the leads in this simulation are not long enough to allow μ_J to achieve its asymptotic value in the leads. Deep inside the emitter lead, using (14), μ_J must be ~ 51.4 meV, while deep in the collector lead μ_J must be ~ -83.6 meV as indicated by the arrows in Fig. 5.5a.

5.9. Conclusion

We have demonstrated that the current potential, μ_J, is a useful quantity for understanding the spatial distribution of the power transfer from the electrons to the phonon bath, at least for devices with one interesting dimension. For inhomogeneous structures under low bias, we find a linear component to the power, P_{TE}, due to thermoelectric effects which can be either positive or negative and a quadratic component, P_J, due to Joule power loss which is positive. The numerical calculations presented in this paper are based on a local phonon model. However, the basic formulation is quite general. Energy balance equations are derived (see Appendix D) in the absence of magnetic fields for systems with local or non-local electron-phonon
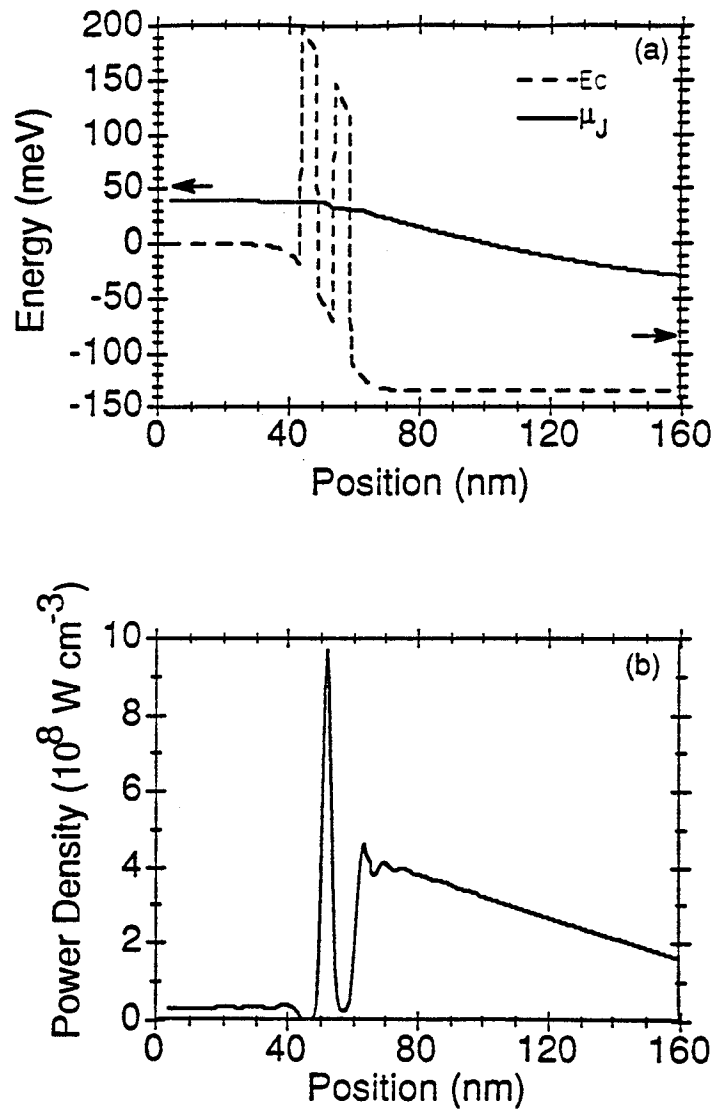
Figure 5.5   (a) Conduction band, E_c, average energy of the current density, μ_J, for double barrier resonant tunneling structure under high bias, 135 mV, with T=77K. (b) Spatial distribution of the power density.

interactions.

CHAPTER 6
SUMMARY AND RECOMMENDATIONS FOR FUTURE WORK

6.1. Summary

The non-equilibrium Green function formalism of Keldysh, Kadanoff and Baym (KKB) provides the starting point for the investigation of high-bias, quantum electron transport in semiconductor nanostructures just as the Boltzmann transport equation provides the starting point for the investigation of semi-classical electron transport. In general, self-energies for electron-phonon and electron-electron scattering are non-local. By using a local model for the electron-phonon interaction in the self-consistent first Born approximation, the general equations, (2.1)-(2.5), simplify to (2.12)-(2.15). A general solution of equations (2.12)-(2.15) for arbitrary potential profiles varying in one direction has been implemented for devices of strictly one dimension or for devices of infinite cross-sectional area with translational invariance in the transverse direction.

The device simulator calculates a number of quantities which are useful for understanding the dynamics of a complex quantum device. The quantities calculated are the spectral function, $A(z;E)$, the non-equilibrium occupation factor, $f(z;E)$, the electron density, $n(z)$, the current density per unit energy, $J(z;E)$, the energy current, $J_E(z)$, and the power density, $P(z)$. The above quantities give a detailed picture of the effect of inelastic transitions on the electron transport.

The simulator also has the capability of calculating a self-consistent electrostatic potential by solving a 1-D Poisson equation although the capability is not used in this work. A simulation which calculates a self-consistent electrostatic potential requires considerably more cpu time than a simulation which does not calculate a self-consistent electrostatic potential. The cpu time requirements are large. The simulation corresponding to Fig. 5.5 required 5.5 hours of cpu time running at an average rate of 50 Mflops on a Cray Y-MP.

The effect of electron-phonon scattering on electron transport through double barrier resonant tunneling diodes has been considered. The first calculation of the effect of phonon scattering on the occupation of the resonance, the energy distribution

of the current density, and the power density are presented in chapters 3-5. Emitter quasi-bound states give rise to a large peak in the I-V characteristic when the emitter quasi-bound state aligns with the resonance in the well. Decreasing the transparency of the collector barrier affects the phonon peak only through the Pauli exclusion principle which enters into the calculation of the scattering rate as the factor of $(1-f_r)$ where f_r is the occupation of the resonance.

6.2. Future Work

This work can be pursued in a number of directions. The numerical efficacy of the code can be enhanced. Presently, attention is being given to obtaining a good energy grid. Mesoscopic structures, such as a DBRTD, have narrow resonances on the order of a few tenths meV that need to be well resolved. Under high bias such that the Fermi-energies of the contacts are split by many $K_B T$, and with inelastic scattering, the current from the emitter flows through the device at energies above (Fig. 5.4) and below (Fig. 4.7) the injection energies. Furthermore A good energy grid is essential to obtaining the correct, current-conserving solution. Details of the energy grid optimization scheme are given in Appendix E. While progress has been made, the energy grid optimization procedure for a complex structure is not robust.

The program can be used to model quantum structures of greater complexity than considered here. An example is shown in Fig. 6.1 of the spectral function of a superlattice and the energy distribution of the current density flowing through the device. Fig. 6.1a shows the beginning of the formation of a mini-band in the nine period superlattice. An individual well alone would contain one resonance. That one resonance is now split into nine resonances in each well. Fig. 6.2b displays the effect of emission of optical phonons on the current density. Initially, the current flows at the energy of the emitter conduction band. As it crosses the superlattice, optical phonons are emitted and bands of current appear at integral multiples of the optical phonon energy below the incident energy. This is a good example of the usefulness of the simulator for obtaining insight into the internal structure and dynamics of a complex quantum device.

A number of directions can be pursued of varying degrees of theoretical and computational difficulty. The above simulations of the superlattice show the importance of mono-layer fluctuations in real devices. Monolayer fluctuations break the translational invariance and give rise to an effective broadening of levels on the order of 10 meV, which is considerably larger than broadening from inelastic scattering. Thus, the discreteness of the levels seen in Fig. 6.1a would not be
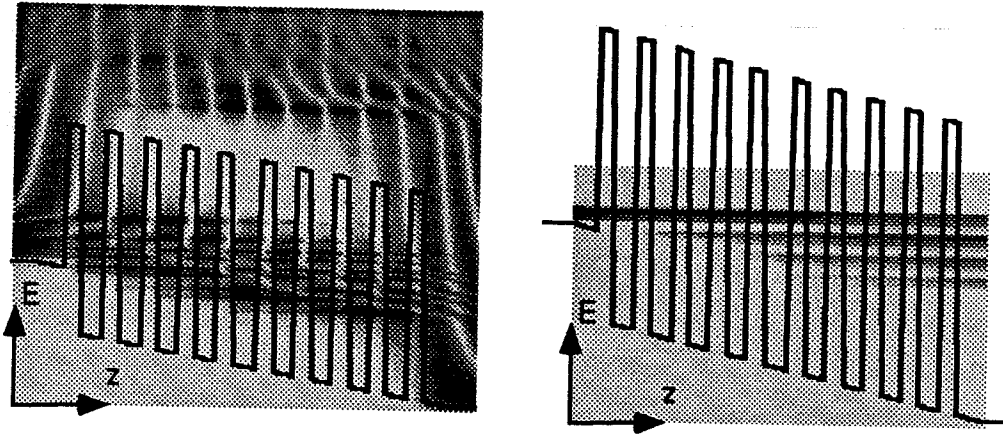
Figure 6.1.   (a) Density of states of a superlattice. (b) Current flow through the superlattice.

observed experimentally. It is not clear how to include the effect of monolayer fluctuations in our simulator.

A more realistic treatment of electron-phonon scattering and a treatment of electron-electron scattering would be of interest. For example, it is believed that the dominant de-phasing mechanism in the well of a DBRTD at resonance is electron-electron scattering [96]. Non-local self-energies are required. For strictly one-dimensional structures, the inclusion of non-local self-energies is straight-forward. For structures of infinite cross-section with translational invariance, the implementation needs to be worked out and it may be found that it is computationally prohibitive.

The inclusion of ac potentials and the interaction with light would be highly desirable. There are a number of device structures that have been proposed or tested [136-138] which are of technological interest to the field of optoelectronics. The nonequilibrium Green function approach has been used to model photocurrent effects in STM tunneling [139] and double barrier resonant tunneling with infrared radiation [140].

LIST OF REFERENCES

LIST OF REFERENCES

1. F. Capasso, K. Mohammed, and A.Y. Cho, *IEEE J. Quantum Electron.*, **QE-22**, 1853 (1986).

2. F. Beltram, F. Capasso, D. L. Sivco, A. L. Hutchinson, S. G. Chu, and A. Y. Cho, *Phys. Rev. Lett.*, **64**, 3167 (1990).

3. Serge Luryi in, *Heterojunction Band Discontinuities Physics and Device Applications*, p. 489, North-Holland, New York, 1987. Federico Capasso and Giorgio Margaritonodo, eds.

4. M.S. Skolnick, D.G. Hayes, P.E. Simmonds, A.W. Higgs, G.W. Smith, H.J. Hutchinson, C.R. Whitehouse, L. Eaves, M. Henini, O.H. Hughes, M.L. Leadbeater, and D.P. Halliday, *Phys. Rev. B*, **41**, 10754 (1990).

5. F. Chevoir and B. Vinter, *Surf. Sci.*, **229**, 158 (1990).

6. A.D. Stone and P.A. Lee, *Phys. Rev. Lett.*, **54**, 1196 (1985).

7. M. Büttiker, *IBM J. Res. Develop.*, **32**, 63 (1988).

8. L.I. Glazman and R.I. Shekhter, *Sov. Phys. JETP*, **67**, 163 (1988).

9. W. Cai, T.F. Zheng, P. Hu, B. Yudanin, and M. Lax, *Phys. Rev. Lett.*, **63**, 418 (1989).

10. N.S. Wingreen, K.W. Jacobsen, and J.W. Wilkins, *Phys. Rev. Lett.*, **61**, 1396 (1988).

11. G.Y. Wu and T.C. McGill, *Phys. Rev. B*, **40**, 9969 (1989).

12. M. Jonson, *Phys. Rev. B*, **39**, 5924 (1989).

13. F. Chevoir and B. Vinter, *Appl. Phys. Lett.*, **55**, 1859 (1989).

14. B.Y. Gu, C. Coluzza, M. Mangiantini, and A. Frova, *Superlattices and Microstructures*, **7**, 29 (1990).

15. V. Pevzner, F. Sols, and Karl Hess in, *Granular Nanoelectronics*, p. 223, Plenum Press, New York, 1991. D.K. Ferry, J.R. Barker, C. Jacoboni, eds.

16. F. Sols, *Scattering, Dissipation, and Transport in Mesoscopic Systems.* (preprint)

17. C. B. Duke, *Tunneling in Solids,* Academic Press, New York, 1969.

18. X. Wu and S.E. Ulloa, *Phys. Rev. B,* **44,** 13148 (1991).

19. J. Bardeen, *Phys. Rev. Lett.,* **6,** 57 (1961).

20. M.C. Payne, *J. Phys. C: Solid State Phys.,* **19,** 1145 (1986).

21. N.S. Wingreen, K.W. Jacobsen, and J.W. Wilkins, *Phys. Rev. B,* **40,** 11834 (1989).

22. G.D. Mahan, *Many-Particle Physics,* Plenum, New York, 1986.

23. R. Bruinsma and Per Bak, *Phys. Rev. Lett.,* **56,** 420 (1986).

24. B. Y. Gelfand, S. Schmitt-Rink, and A.F.J. Levi, *Phys. Rev. Lett.,* **62,** 1683 (1989).

25. L.V. Keldysh, *Zh. Eksp. Teor. Fiz.,* **47,** 1515 (1964). [Sov. Phys. JETP **20,** 1018, (1965)].

26. C. Caroli, R. Combescot, P. Nozieres, and D. Saint-James, *J. Phys. C: Solid State Phys.,* **4,** 916 (1971).

27. C. Caroli, R. Combescot, D. Lederer, P. Nozieres, and D. Saint-James, *J. Phys. C: Solid State Phys.,* **4,** 2598 (1971).

28. C. Caroli, R. Combescot, P. Nozieres, and D. Saint-James, *J. Phys. C: Solid State Phys.,* **5,** 21 (1972).

29. R. Combescot, *J. Phys. C: Solid State Phys.,* **4,** 2611 (1971).

30. R. Combescot and G. Screder, *J. Phys. C: Solid State Phys.,* **6,** 1363 (1973).

31. R. Combescot and G. Screder, *J. Phys. C: Solid State Phys.,* **7,** 1318 (1974).

32. T. Ivezic, *J. Phys. C: Solid State Phys.,* **8,** 3371 (1975).

33. E.V. Anda and F. Flores, *J. Phys.: Condens. Matter,* **3,** 9087 (1991).

34. T. E. Feuchtwang, *Phys. Rev. B,* **10,** 4121 (1974).

35. T. E. Feuchtwang, *Phys. Rev. B,* **10,** 4135 (1974).

36. U. Ravaioli, M.A. Osman, W. Potz, N. Kluksdahl, and D.K. Ferry, *Physica,* **134B,** 36 (1985).

37. W.R. Frensley, *Phys. Rev. B,* **36,** 1570 (1987).

38. N.C. Kluksdahl, A.M. Kriman, D.K. Ferry, and C. Ringhofer, *Phys. Rev. B,* **39,** 7720 (1989).

39. W.R. Frensley, *Rev. Mod. Phys.,* **62,** 745 (1990).

40. F.A. Buot and K.L. Jensen, *Phys. Rev. B,* **42,** 9429 (1990).

41. R. Tsu and L. Esaki, *Appl. Phys. Lett.*, **22**, 562 (1973).

42. M. Cahay, M. McLennan, S. Datta, and M.S. Lundstrom, *Appl. Phys. Lett.*, **50**, 612 (1987).

43. D. Landheer and G.C. Aers, *Superlattices and Microstructures*, **7**, 17 (1990).

44. M.J. Mclennan, *Quantum Ballistic Transport in Semiconductor Heterostructures*, Master's Thesis, Purdue University, 1987.

45. P. J. Turley and S. W. Teitsworth, *Phys. Rev. B*, **44**, 3199 (1991).

46. P. J. Turley and S. W. Teitsworth, *Phys. Rev. B*, **44**, 8181 (1991).

47. P. J. Turley and S. W. Teitsworth, *Phys. Rev. B*, **44**, 12959 (1991).

48. L.P. Kadanoff and G. Baym, *Quantum Statistical Mechanics*, Benjamin, Reading, Mass., 1962.

49. We use 1-D to mean devices with one interesting direction and translational invariance in the transverse directions. We will use "strictly 1-D" to describe a device with only one quantized transverse energy below the Fermi level.

50. A. Jauho, *Solid-State Electronics*, **32**, 1265 (1989).

51. R. Lake and S. Datta, *Phys. Rev. B*, **45**, 6670 (1992).

52. R. Lake and S. Datta, in *Nanostructures and Mesoscopic Systems*, p. 387, edited by W.P. Kirk and M. Reed, Academic Press , 1992.

53. R. Lake and S. Datta, *Phys. Rev. B*, **46** (1992). (to appear)

54. R. Lake, G. Klimeck, M. McLennan, and S. Datta, *A Quantum Device Simulator Based on the Non-Equilibrium Green Function Equations of Keldysh, Kadanoff, and Baym*, to appear in the proceedings of the International Workshop on Computational Electronics, Urbana-Champaigne, Illinois, May 28-29, 1992

55. R. Lake, G. Klimeck, and S. Datta, *The Effect of Barrier Asymmetry on the Phonon Peak in Double Barrier Resonant Tunneling*, (preprint)

56. P. Danielewicz, *Annals of Physics*, **152**, 239 (1984).

57. J. Rammer and H. Smith, *Rev. Mod. Phys.*, **58**, 323 (1986).

58. G.D. Mahan, *Physics Reports*, **145**, 251 (1987).

59. E. Runge and H. Ehrenreich, *Phys. Rev. B*, **45**, 9145 (1992).

60. L. Y. Chen and C. S. Ting, *Phys. Rev. B*, **41**, 8533 (1990).

61. L. Y. Chen and C. S. Ting, *Phys. Rev. B*, **43**, 2097 (1991).

62. L. Y. Chen and C. S. Ting, *Phys. Rev. Lett.*, **64**, 3159 (1990).

63. A. Groshev, T. Ivanov, and V. Valtchinov, *Phys. Rev. Lett.*, **66**, 1082 (1991).

64. L. Y. Chen and C. S. Ting, *Phys. Rev. B*, **44**, 5916 (1991).

65. S. Hershfield, J.H. Davies, and J.W. Wilkins, *Phys. Rev. Lett.*, **67**, 3720 (1991).

66. J. Kinaret, Y. Meir, N. S. Wingreen, P. A. Lee, and X. G. Wen, *Phys. Rev. B (to appear)*.

67. Y. Meir and N.S. Wingreen, *Phys. Rev. Lett.*, **68**, 2512 (1992).

68. S. Datta and M. P. Anantram, *Phys. Rev. B*, **45**, 13761 (1992).

69. S. Datta, *J. Phys. Condens. Matter*, **2**, 8023 (1990).

70. F.S. Khan, J.H. Davies, and J.W. Wilkins, *Phys. Rev. B*, **36**, 2578 (1987).

71. K.L. Jensen and F.A. Buot, *Phys. Rev. Lett.*, **66**, 1078 (1991).

72. M. J. McLennan, Y. Lee, and S. Datta, *Phys. Rev. B*, **43**, 13846 (1991).

73. F. Sols, M. Macucci, U. Ravaioli, and K. Hess, *J. Appl. Phys.*, **66**, 3892 (1989).

74. A.D. Stone and A. Szafer, *IBM J. Res. Develop.*, **32**, 384 (1988).

75. H.U. Baranger and A.D. Stone, *Phys. Rev. B*, **40**, 8169 (1989).

76. S. Selberherr, *Analysis and Simulation of Semiconductor Devices,* Springer-Verlag, New York, 1984.

77. M.S. Lundstrom, *Fundamentals of Carrier Transport: Vol. 10 in the Modular Series on Solid State Devices,* Addison-Wesley, Reading, Mass., 1990. Gerold W. Neudeck and Robert F. Pierret, eds.

78. R. Landauer, *Z. Phys. B*, **68**, 217 (1987).

79. M. Büttiker, *Phys. Rev. Lett.*, **57**, 1761 (1986).

80. M.J. McLennan and S. Datta, *SEQUAL 2.1 User's Manual,* Purdue University TR-EE 89-17, 1989.

81. R. Landauer, *Phil. Mag.*, **21**, 863 (1970).

82. M. Büttiker, Y. Imry, R. Landauer, and S. Pinhas, *Phys. Rev. B*, **31**, 6207 (1985).

83. Y. Imry in, *Directions in Condensed Matter Physics,* p. 101, World Scientific, Singapore, 1986. G. Grinstein and G. Mazenko, eds.

84. R. Landauer, *IBM J. Res. Develop.*, **32**, 306 (1988). (and refs. therein).

85. R. Landauer, *IBM J. Res. Dev.*, **1**, 223 (1957).

86. M. Büttiker, *IBM J. Res. Develop.*, **32**, 317 (1988).

87. C.W.J. Beenakker and H. van Houten in, *Solid State Physics,* 44, Academic Press, 1991. H. Ehrenreich and D. Turnbull, eds.

88. Eq. (2.23) is obtained using (C.5) and (B.18) of Ref. [69] and the equilibrium relation (2.20).

89. G. Neofotistos, R. Lake, and S. Datta, *Phys. Rev. B*, **43**, 2442 (1991).

90. D.S. Fisher and P.A. Lee, *Phys. Rev. B*, **23**, 6851 (1981).

91. Arthur C. Smith, James F. Janak, and Richard B. Adler, *Electronic Conduction in Solids,* McGraw-Hill, New York, 1967.

92. Since we are working with three dimensional devices, the resonant level fills up with states of increasing transverse energy. By "bottom of the resonance", we mean the resonant energy of electrons with zero transverse energy.

93. S. Luryi, *Appl. Phys. Lett.*, **47**, 491 (1985).

94. S. Luryi, *Superlatt. Microst.*, **5**, 375 (1989).

95. T. Weil and B. Vinter, *Appl. Phys. Lett.*, **50**, 1281 (1987).

96. C.H. Yang, Jean M. Carlson-Swindle, S.A. Lyon, and J.M. Worlock, *Phys. Rev. Lett.*, **55**, 2359 (1985).

97. K. Hess in, *Physics of Nonlinear Transport in Semiconductors,* p. 1, Plenum, New York, 1980. D.K. Ferry, J. Barker, and C. Jacoboni, eds.

98. R. Landauer, in *Localization, Interaction, and Transport Phenomena,* 38, Springer-Verlag, New York (1985). B. Kramer, G. Bergmann, and Y. Bruynseraede, eds.

99. J. S. Wu, C. Y. Chang, C. P. Lee, K. H. Chang, D. G. Liu, and D. C. Liou, *Appl. Phys. Lett.*, **57**, 2311 (1990).

100. *Resonant Tunneling in Semiconductors Physics and Applications,* edited by L.L. Chang, E.E. Mendez, and C. Tejedor, Plenum Press, New York, 1991.

101. M. Büttiker in ref. [100] p. 213.

102. M. Jonson and A. Grincwajg, *Appl. Phys. Lett.*, **51**, 1729 (1987).

103. W.R. Frensley, *Solid-State Electronics*, **31**, 739 (1988).

104. M.L. Leadbeater, E.S. Alves, L. Eaves, M. Henni, O.H. Hughes, F.W. Sheard, and G.A. Toombs, R.K. Mains, and G.I. Haddad, *J. Appl. Phys.*, **64**, 5041 (1988).

105. W.R. Frensley, *Solid State Electronics*, **32**, 1235 (1989).

106. A.N. Khondker, *J. Appl. Phys.*, **67**, 6432 (1990).

107. M.A. Alam, R.A. Morrisey, and A.N. Khondker, *J. Appl. Phys.*, **71**, 3077 (1992).

108. P. Roblin and L. Wan-Rone, *preprint*.

109. V.J. Goldman, D.C. Tsui, and J.E. Cunningham, *Phys. Rev. B*, **36**, 7635 (1987).

110. B.G.R. Rudberg, *Semicond. Sci. Technol.*, **5**, 328 (1990).

111. P. Hyldgaard and A.P. Jauho, *J. Phys.: Condens. Matter*, **2**, 8725 (1990).

112. J.A. Stovneng, E.H. Hauge, P. Lipavsky, and V. Spicka, *Phys. Rev. B*, **44**, 13595 (1991).

113. J.J.L. Rascol, K.P. Martin, S. Ben Amor, R.J. Higgins, A. Celeste, J.C. Portal, A. Torabi, H.M. Harris, and C.J. Summers, *Phys. Rev. B*, **41**, 3733 (1990).

114. M.L. Leadbeater, E.S. Alves, L. Eaves, M. Henni, O.H. Hughes, A. Celeste, J.C. Portal, G. Hill, and M.A. Pate, *Phys. Rev. B*, **39**, 3438 (1989).

115. G.S. Boebinger, A.F.J. Levi, S. Schmitt-Rink, A. Passner, L.N. Pfeiffer, and K.W. West, *Phys. Rev. Lett.*, **65**, 235 (1990).

116. J.G. Chen, C.H. Yang, M.J. Yang, and R.A. Wilson, *Phys. Rev. B*, **43**, 4531 (1991).

117. P. J. Turley and S. W. Teitsworth, "Theory of localized phonon modes and their effects on electron tunneling in double barrier structures," (preprint).

118. N. Mori and T. Ando, *Phys. Rev. B*, **40**, 6175 (1989).

119. E.S. Alves, L. Eaves, M. Henni, O.H. Hughes, M.L. Leadbeater, F.W. Sheard, and G.A. Toombs, *Electronics Letters*, **24**, 1190 (1988).

120. P. J. Turley, C. R. Wallis, and S. W. Teitsworth, "Experimental evidence for symmetric interface phonons in GaAs/AlAs double barrier structures," (preprint).

121. A. Jauho, *Phys. Rev. B*, **41**, 12327 (1990).

122. $\Gamma_{E(C)} \equiv |W_{E(C)}/W|^2 \hbar v_{E(C)}/a$ where $v_{E(C)}$ is the velocity in the emitter (collector) lead and a is the lattice spacing.

123. Equations (4.15) and (4.16) are similar to equations (4) and (5) of ref. [65].

124. R. Landauer, in *Electrical Transport and Optical Properties of Inhomogeneous Media*, ed. by J.C. Garland, D.B. Tanner, AIP, New York, (1978).

125. M. Büttiker, *Phys. Rev. B*, **40**, 3409 (1989).

126. M.C. Payne, *J. Phys. Cond. Matter*, **1**, 4931 (1989).

127. M.C. Payne and G.E. Engel, *J. Phys. Condens. Matter*, **2**, 1355 (1990).

128. C.S. Chu and R.S. Sorbello, *Phys. Rev. B15*, **40**, 5950 (1989).

129. P.L. Pernas, A. Martin-Rodero, and F. Flores, *Phys. Rev. B*, **41**, 8553 (1990).

130. P.L. Pernas and F. Flores, *Physica B*, **175**, 221 (1991).

131. M. Büttiker, *Phys. Rev. B*, **33**, 3020 (1986).

132. T. Wang, K. Hess, and G.J. Iafrate, *J. Appl. Phys.*, **58**, 857 (1985).

133. F. Venturi, E. Sangiorgi, S. Luryi, P. Poli, L. Rota, and C. Jacoboni, *IEEE Transactions on Electron Devices*, **38**, 611 (1991).

134. R. Landauer, *Physica Scripta* (1992). (to appear)

135. S. Datta and R. Lake, *Phys. Rev. B*, **44**, 6538 (1991).

136. Q. Hiu and S. Feng, *Appl. Phys. Lett.*, **59**, 2923 (1991).

137. Kastalsky, V. J. Goldman, and H. Abeles, *Appl. Phys. Lett.*, **59**, 2636 (1991).

138. A. Larsson, S. I. Borenstain, B. Jonsson, I. Andersson, J. Westin, and T. G. Andersson, *Appl. Phys. Lett.*, **58**, 1297 (1991).

139. A. L. Yeyati and F. Flores, *Phys. Rev. B*, **44**, 9020 (1991).

140. P. Johansson and G. Wendin, *Phys. Rev. B*, **45**, 15 July 1992, (to appear).

141. S. Datta, M.S. Lundstrom, A. Das, R. Lake, M.J. McLennan, and M. Stettler, *Physics and Modeling of Submicron Devices*, p. 137, Purdue University Technical Report: TR-EE 89-59, 1989.

142. P.M. Morse and H. Feshbach, *Methods of Theoretical Physics*, p. 884, McGraw-Hill, New York, 1953.

143. A.N. Khondker and M.A. Alam, *Phys. Rev. B*, **44**, 5444 (1991).

APPENDICES

Appendix A: Infinite Cross Section

To simulate a device with translational invariance, we wish to only compute one dimensional quantities. We achieve this by averaging Eqs. (2.13), (2.17), and (2.23) over the transverse plane. The derivation that follows is identical in spirit to a simpler derivation by Mclennan in which only the case of a constant τ_ϕ, independent of position and energy, was considered [141]. We assume a separable Hamiltonian. Furthermore, since the system is translationally invariant, we assume that the occupation factor, $f(r;E)$, and the phase relaxation time, $\tau_\phi(r;E)$, are not functions of the transverse coordinates. Thus, the transverse eigenfunctions of the Hamiltonian,

$$H_\tau(r;E) = H_o(r) - i\hbar/\tau_\phi(r;E) \tag{A.1}$$

are plane waves.

We will take Eq. (2.13) as an example. The transverse coordinates are x and y, and the longitudinal coordinate is z. We begin by multiplying both sides of (13) by $N_o(r;E)$ and then averaging both sides over the cross section. Considering the left hand side first, we have

$$f(z;E) \frac{1}{W_x W_y} \int dx\, dy\, N_o(x,y,z;E) \tag{A.2}$$

Next, we write N_o as $-\text{Im}\, G^R(r,r;E)/\pi$ and expand G^R in terms of the eigenfunctions of (A.1). Since we have assumed that τ_ϕ is only a function of z, the transverse part of H_τ is Hermitian with plane wave eigenfunctions. The z-component is non-Hermitian and is expanded in terms of the eigenfunctions $\chi_n(z)$ and $\eta_n(z)$ of the adjoint operators $H_\tau(z)$ and $H_\tau^*(z)$ [142]. Eq. (A.2) becomes

$$f(z;E) \frac{1}{W_x W_y} \int dx\, dy\, \frac{-1}{\pi} \text{Im} \sum_{l,m,n} \frac{\phi_l(x)\phi_m(y)\chi_n(z)\phi_l^*(x)\phi_m^*(y)\eta_n^*(z)}{E - \varepsilon_l - \varepsilon_m - \varepsilon_n} \tag{A.3}$$

ϕ_l and ϕ_m are plane wave eigenstates, $\phi_l(x) = \exp(ik_l x)/\sqrt{W_x}$. ε_l and ε_m are the corresponding eigenenergies. ε_n is the complex eigenvalue corresponding to χ_n and η_n^*. Since the plane-waves appear with their complex conjugates, they disappear from (A.3), and (A.3) becomes

$$f(z;E) \frac{1}{W_x W_y} \frac{-1}{\pi} \text{Im} \sum_{l,m,n} \frac{\chi_n(z)\eta_n^*(z)}{E - \varepsilon_l - \varepsilon_m - \varepsilon_n} \tag{A.4}$$

We re-write the term $\frac{-1}{\pi} \text{Im} \sum_{l,m,n}$ in (A.4) as

$$\sum_{l,m} N_o^{1-D}(z; E-\epsilon_l-\epsilon_m) \tag{A.5}$$

where N_o^{1-D} is the density of states obtained from only considering the z-component of H_τ. Defining a quantity $<N_o>$ as

$$<N_o(z;E)> = \frac{1}{W_x W_y} \sum_{l,m} N_o^{1-D}(z; E-\epsilon_l-\epsilon_m)$$

$$= \frac{m^*}{2\pi\hbar^2} \int_{-\infty}^{E} dE' N_o^{1-D}(z; E') \tag{A.6}$$

(A.4) becomes

$$f(z;E) <N_o(z;E)> \tag{A.7}$$

Now we consider the right hand side of (13). We substitute (2.14a) into (2.13) and average over the cross section to obtain.

$$\frac{1}{W_x W_y} \frac{\hbar}{2\pi} \int dE' \int dz' \int dx\,dy\,dx'dy' \left\{ |G^R(\mathbf{r},\mathbf{r}';E)|^2 N_0(\mathbf{r}';E')f(z';E')F(E-E') \right\} \tag{A.8}$$

The integral

$$\frac{1}{W_x W_y} \int dx\,dy\,dx'dy' |G^R(\mathbf{r},\mathbf{r}';E)|^2 N_0(\mathbf{r}';E') \tag{A.9}$$

is evaluated by expanding $|G^R|^2$ and N_0 in terms of the eigenfunctions of H_τ. Writing out the expansion, (A.9) becomes

$$\frac{1}{W_x W_y} \int dx\,dy\,dx'dy' \left\{ \sum_{l,m,n} \frac{\phi_l(x)\phi_m(y)\chi_n(z)\phi_l^*(x')\phi_m^*(y')\eta_n^*(z')}{E-\epsilon_l-\epsilon_m-\epsilon_n} \right.$$

$$\sum_{l',m',n'} \frac{\phi_{l'}^*(x)\phi_{m'}^*(y)\chi_{n'}^*(z)\phi_{l'}(x')\phi_{m'}(y')\eta_{n'}(z')}{E-\epsilon_{l'}-\epsilon_{m'}-\epsilon_{n'}^*}$$

$$\left. \frac{-1}{\pi} \mathrm{Im} \sum_{i,j,k} \frac{\phi_i(x')\phi_j(y')\chi_k(z')\phi_i^*(x')\phi_j^*(y')\eta_k^*(z')}{E-\epsilon_i-\epsilon_j-\epsilon_k} \right\} \tag{A.10}$$

The third term in the integrand of (A.10) is $<N_o(z;E)>$. The integrals over x' and y' give factors of $\delta_{l,l'}$ and $\delta_{m,m'}$, respectively. $\dfrac{1}{W_x W_y}$ times the integral of the first two terms in the integrand of (A.10) becomes

$$\frac{1}{W_x W_y} \sum_{l,m} \left\{ \sum_n \frac{\chi_n(z)\eta_n^*(z')}{E-\epsilon_l-\epsilon_m-\epsilon_n} \sum_{n'} \frac{\chi_{n'}^*(z)\eta_{n'}(z')}{E-\epsilon_l-\epsilon_m-\epsilon_{n'}^*} \right\} \qquad (A.11)$$

The quantity in (A.11) is

$$\frac{1}{W_x W_y} \sum_{l,m} |\, G_{1-D}^R(z,z';E-\epsilon_l-\epsilon_m)\,|^2 \qquad (A.12)$$

where G_{1-D}^R is the retarded Green's function of the z-component of H_τ. We define the quantity $<|G^R|^2>$ as

$$< |G_R(z,z';E)|^2 > = \frac{1}{W_x W_y} \sum_{l,m} |G_{1-D}^R(z,z';E-\epsilon_l-\epsilon_m)|^2$$

$$= \frac{m^*}{2\pi\hbar^2} \int_{-\infty}^{E} dE' |G_{1-D}^R(z,z';E')|^2 \qquad (A.13)$$

Putting this all back together, Eq. (2.13) becomes

$$f(z;E) = \frac{\hbar}{2\pi} \frac{1}{<N_0(z;E)>} \int dz' \frac{<|G^R(z,z';E)|^2>}{<\tau_p(z';E)>} \qquad (A.14)$$

where

$$\left[E + \frac{\hbar^2}{2m^*} \frac{d^2}{dz^2} - V(z) + \frac{i\hbar}{2<\tau_\phi(z;E)>} \right] G_{1-D}^R(z,z';E) = \delta(z-z') \qquad (A.15)$$

$$\frac{1}{<\tau_p(z;E)>} = \frac{2\pi}{\hbar} \int dE' F(E-E') <N_0(z;E')> f(z;E') \qquad (A.16)$$

$$\frac{1}{<\tau_n(z;E)>} = \frac{2\pi}{\hbar} \int dE' F(E'-E) <N_0(z;E')> \left[1-f(z;E') \right] \qquad (A.17)$$

and

$$\frac{1}{<\tau_\phi(z;E)>} = \frac{1}{<\tau_n(z;E)>} + \frac{1}{<\tau_p(z;E)>} \qquad (A.18)$$

Equations (2.12) through (2.15) become equations (A.14) through (A.18) which are the coupled set of equations that we have numerically solved to provide the results shown in this paper.

The equations for the current density, eq. (2.17), and the terminal current, eq. (2.23), are treated the same way.

Appendix B: Solution Procedure

Fig. 12 is a flow chart of the solution procedure when inelastic, energy-dependent scattering is present. To save on notation, all quantities such as the τ's, N_0, $|G^R|^2$, and J represent their bracketed counterparts due to averaging over the cross section as described in Appendix A. Note that a Poisson solver for self-consistent electrostatic solutions exists in the loop although it has not been used in the simulations presented in this paper.
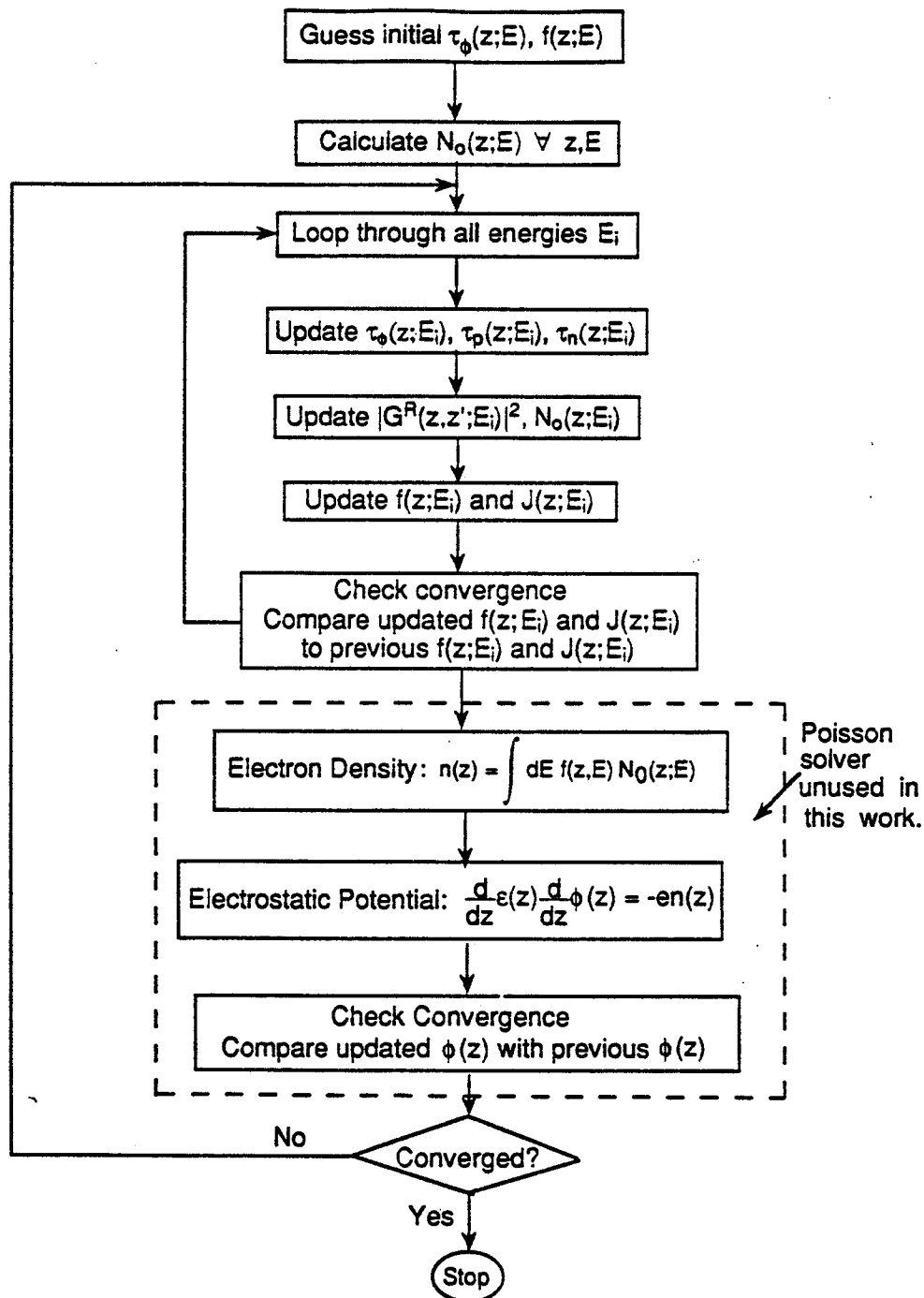
Figure B.1   Flow chart for numerical solution.

Appendix C: Fisher-Lee Transmission Coefficient

For a strictly 1-D (one transverse energy) device, the Fisher-Lee transmission coefficient is [90]

$$T(E) = \hbar^2\, v_1\, v_2\, |G^R(z_1,z_2;E)|^2 \tag{C.1}$$

To show that Eq. (2.25) reduces to (C.1), we consider a 1-D device with the contact-device interface of contact 1 at point z_1 and the contact-device interface of contact 2 at point z_2. The contacts are far enough away from the disordered region so that the self-energies are independent of position in the contacts. Then, the Green's function connecting point z in contact 1 and point z′ in contact 2 is

$$G^R(z,z';E) = e^{i\gamma_1(z_1-z)}\, G^R(z_1,z_2;E)\, e^{i\gamma_2(z'-z_2)} \tag{C.2}$$

where

$$\gamma_j = [\,2m^*(E-V_j+i\frac{\hbar}{2\tau_{\phi_j}(E)})\,]^{1/2}/\hbar \tag{C.3}$$

In (C.3) j stands for either 1 or 2 for γ in contact 1 or 2, respectively. The integral in (25) becomes

$$\frac{\hbar^2\,|G^R(z_1,z_2;E)|^2}{\tau_{\phi_1}\,\tau_{\phi_2}} \int\limits_{-\infty}^{z_1} dz \int\limits_{z_2}^{\infty} dz'\, e^{-2\mathrm{Im}\,\gamma_1(z_1-z)}\, e^{-2\mathrm{Im}\,\gamma_2(z'-z_2)} \tag{C.4}$$

Performing the integral in (C.4) gives

$$T(E) = \frac{\hbar^2\,|G^R(z_1,z_2;E)|^2}{\tau_{\phi_1}\,\tau_{\phi_2}}\,\frac{1}{2\mathrm{Im}\,\gamma_1}\,\frac{1}{2\mathrm{Im}\,\gamma_2} \tag{C.5}$$

In terms of E and τ_ϕ,

$$\mathrm{Im}\,\gamma = \frac{\sqrt{m}}{\hbar}\left\{\left[(E-V)^2+\left[\frac{\hbar}{2\tau_\phi}\right]^2\right]^{1/2}-(E-V)\right\}^{1/2} \tag{C.6a}$$

and

$$\mathrm{Re}\,\gamma = \frac{\sqrt{m}}{\hbar}\left\{\left[(E-V)^2+\left[\frac{\hbar}{2\tau_\phi}\right]^2\right]^{1/2}+E-V\right\}^{1/2} \qquad \text{(C.6b)}$$

If we follow Khondker [143] and define the group velocity, $v(E)$, as

$$v(E) = \frac{\hbar\,\mathrm{Re}\,\gamma}{m^*}$$

we evaluate $\mathrm{Im}\,\gamma$ by multiplying by $\dfrac{v(E)}{v(E)}$, expanding out all the quantities using (C.6) and find

$$\mathrm{Im}\,\gamma = \frac{1}{2\,v\,\tau_\phi} \qquad \text{(C.7)}$$

If $(E\text{-}V) \gg \dfrac{\hbar}{2\tau_\phi}$, $v(E)$ reduces to the usual quantity, $v = \dfrac{[2m(E-V)]^{1/2}}{m^*}$. Thus, the coherent component of the current is given by the usual tunneling formula (2.26) with the Fisher-Lee form for the transmission coefficient. For devices with infinite cross section with translational invariance across the cross-section, the contribution from the transverse energies is included as described in Appendix A. For devices very short compared to L_ϕ, the coherent current is essentially the total current and the our quantum-kinetic equation reduces to the tunneling formula (2.26).

Appendix D: Derivation of the Energy Balance Equation (5.2)

In this appendix, our notation for the Green functions and self energies corresponds to that used by Danielewicz [56]. We write our Hamiltonian as ($\hbar = 1$)

$$H(t) = \int dr \psi^\dagger(r,t) \left[\frac{-\nabla^2}{2m^*} + U(r) \right] \psi(r,t) + \int dr \psi^\dagger(r,t)\psi(r,t)\phi(r,t) + H_B(t) \qquad (D1)$$

where the ψ's are the electron field operators, H_B is the Hamiltonian of the phonon bath, and ϕ is the phonon field operator which includes the coupling constant. Evaluating the equation of motion for ψ and $\psi^\dagger$ as described by Kadanoff and Baym [48] leading to their eq. (2-8), we find

$$\int dr \frac{1}{2} i \left\{ \left[\frac{\partial}{\partial t} - \frac{\partial}{\partial t'} \right] \psi^\dagger(r,t')\psi(r,t) \right\}_{t' \to t} =$$

$$\int dr \left\{ \left[-\frac{1}{2} \left[\frac{\nabla^2 + \nabla'^2}{2m^*} \right] + U(r) \right] \psi^\dagger(r',t)\psi(r,t) \right\}_{r' \to r} + \int dr \psi^\dagger(r,t)\psi(r,t)\phi(r,t) \quad (D2)$$

The right hand side of (D2) is the electronic energy, $H_e = H - H_B$. Fourier transforming the time difference coordinate to energy, we obtain

$$\int dr \int dE \, E \, n(r;E,T) = \langle H_e(T) \rangle \qquad (D3)$$

where $\qquad T = \frac{t+t'}{2}, \qquad n(r;E,T) = \frac{-i}{2\pi} G^<(r,r;E,T), \qquad$ and

$$G^<(r,r;E,T) = \int \frac{dE}{2\pi} e^{-iE(t-t')} i \langle \psi^\dagger(r,t')\psi(r,t) \rangle.$$

We must define a local electronic energy density to derive a local energy balance equation. From (D2), we define the local electronic energy density as

$$\langle h_e(r,t) \rangle = \lim_{r' \to r} \left\{ \left[-\frac{1}{2} \left[\frac{\nabla^2 + \nabla'^2}{2m^*} \right] + U(r) \right] \langle \psi^\dagger(r',t)\psi(r,t) \rangle \right\} + \langle \psi^\dagger(r,t)\psi(r,t)\phi(r,t) \rangle \qquad (D4)$$

From (D2) and (D3), this can be written as $\langle h_e(r,T) \rangle = \int dE \, E \, n(r;E,T)$. This definition of the local electronic energy density appears reasonable if we view $n(r,E,T)$ as the number of electrons with energy E at position r and time T. Of course, this viewpoint has to be used with caution since $n(r,E,T)$ is not positive

definite.

To derive a balance equation for $\langle h_e(r,T) \rangle$, we start with Eq. (4) written in its most general form [17]

$$G^<(1,2) = \int d3\,d4\, G^R(1,3)\Sigma^<(3,4)G^A(4,2) \tag{D5}$$

where the integers stand for both the space and time variable, eg. $1=(r_1,t_1)$. Operating on (D5) from the left with $(i\frac{\partial}{\partial t_1} - H_o(1))$ where $H_o(1) = \frac{-\nabla_1^2}{2m^*} + U(r_1)$ gives

$$\left[i\frac{\partial}{\partial t_1} - H_o(1)\right]G^<(1,2) = \int d3 \left\{\Sigma^R(1,3)\,G^<(3,2) + \Sigma^<(1,3)\,G^A(3,2)\right\} \tag{D6}$$

Similarly, hitting (D5) on the left with $(-i\frac{\partial}{\partial t_2} - H_o(2))$ results in

$$\left[-i\frac{\partial}{\partial t_2} - H_o(2)\right]G^<(1,2) = \int d3 \left\{G^R(1,3)\,\Sigma^<(3,2) + G^<(1,3)\,\Sigma^A(3,2)\right\} \tag{D7}$$

To obtain (D6) and (D7), we have used the relations

$$\left[i\frac{\partial}{\partial t_1} - H_o(1)\right]G^R(1,2) = \delta(1-2) + \int d3\,\Sigma^R(1,3)\,G^R(3,2)$$

and

$$\left[-i\frac{\partial}{\partial t_2} - H_o(2)\right]G^A(1,2) = \delta(1-2) + \int d3\,G^A(1,3)\,\Sigma^A(3,2)$$

Equations (D6) and (D7) are identical to equations (8-27a) and (8-28a) of Kadanoff and Baym [48], and (D6) is identical to equation (60) of Keldysh [25].

Now, we subtract (D7) from (D6) to obtain

$$\left[i\frac{\partial}{\partial t_1} + i\frac{\partial}{\partial t_2} + \frac{\nabla_1^2}{2m^*} - \frac{\nabla_2^2}{2m^*} - U(r_1) + U(r_2)\right]G^<(1,2)$$

$$= \int d3\,\{\,\Sigma^R(1,3)G^<(3,2) + \Sigma^<(1,3)G^A(3,2) - G^R(1,3)\Sigma^<(3,2) - G^<(1,3)\Sigma^A(3,2)\,\} \tag{D8}$$

This is identical to equation (9-3) of Kadanoff and Baym [48]. To obtain the energy balance equation we operate on (D8) with $\frac{-i}{2}(\partial/\partial t_1 - \partial/\partial t_2)$ and take the limit as $r_2,t_2 \to r_1,t_1$ to obtain

$$\frac{-i}{2}\left[i\left[\frac{\partial}{\partial t_1}+\frac{\partial}{\partial t_2}\right]\left[\frac{\partial}{\partial t_1}-\frac{\partial}{\partial t_2}\right]G^<(\mathbf{r}_1,t_1,\mathbf{r}_1,t_2)\right]_{t_2\to t_1}$$

$$+\frac{-i}{2}\left[\left[\frac{\partial}{\partial t_1}-\frac{\partial}{\partial t_2}\right]\left[\frac{\nabla_1^2-\nabla_2^2}{2m^*}\right]G^<(\mathbf{r}_1,t_1,\mathbf{r}_1,t_2)\right]_{\mathbf{r}_2,t_2\to\mathbf{r}_1,t_1}$$

$$=\frac{-i}{2}\left[\left(\frac{\partial}{\partial t_1}-\frac{\partial}{\partial t_2}\right)\int d3\,\{\,\Sigma^R(1,3)G^<(3,2)+\Sigma^<(1,3)G^A(3,2)\right.$$

$$\left.-G^R(1,3)\Sigma^<(3,2)-G^<(1,3)\Sigma^A(3,2)\,\}\,\right]_{2\to 1} \quad\text{(D9)}$$

where, on the right hand side, the integers stand for both the space and time variable, eg. $1=(\mathbf{r}_1,t_1)$. Since we are concerned with steady-state, we have let the single-particle potential U be time independent.

Changing to center-of-mass and relative coordinates and Fourier transforming the time-difference coordinate, (D9) becomes

$$\frac{\partial}{\partial T}\langle h_e(\mathbf{R},T)\rangle + \int dE\,E\,\nabla\cdot\mathbf{J}_N(\mathbf{R},E,T) = -P(\mathbf{R},T) \quad\text{(D10)}$$

where, since the limit $\mathbf{r}_2\to\mathbf{r}_1$ has been taken, $\mathbf{R}\equiv\dfrac{\mathbf{r}_1+\mathbf{r}_2}{2}=\mathbf{r}_1$. The first term is the time rate of change of the energy density. The second term is the divergence of the energy current, $\nabla\cdot\mathbf{J}_E(\mathbf{R},T)$, where $\mathbf{J}_E(\mathbf{R},T)=\int dE\,E\,\mathbf{J}_N(\mathbf{R},E,T)$ and $\mathbf{J}_N(\mathbf{R},E,T)$ is the particle current per unit energy. The right hand side represents the power transferred from the phonons to the electrons due to scattering. In steady-state, we can write (cf. Eq. (7))

$$\nabla\cdot\mathbf{J}_E(\mathbf{R}) = -P(\mathbf{R}) \quad\text{(D11a)}$$

where the energy current $\mathbf{J}_E(\mathbf{R}) = \int dE\,E\,\mathbf{J}_N(\mathbf{R},E)$ and the local power transfer $P(\mathbf{R})$ is given by

$$P(\mathbf{R})=\int dE\,E\int d\mathbf{r}'\{\Sigma^R(\mathbf{R},\mathbf{r}';E)G^<(\mathbf{r}',\mathbf{R};E)+\Sigma^<(\mathbf{R},\mathbf{r}';E)G^A(\mathbf{r}',\mathbf{R};E)$$

$$-G^R(\mathbf{R},\mathbf{r}';E)\Sigma^<(\mathbf{r}',\mathbf{R};E)-G^<(\mathbf{R},\mathbf{r}';E)\Sigma^A(\mathbf{r}',\mathbf{R};E)\,\} \quad\text{(D11b)}$$

It is interesting to check that in equilibrium, in the absence of magnetic fields, such that detailed balance exists, $P(\mathbf{R})=0$. Matrix notation will be used to represent the spatial integrations. The energy coordinate will be suppressed. In this notation, $\int d\mathbf{r}'\Sigma(\mathbf{R},\mathbf{r}';E)G(\mathbf{r}',\mathbf{R};E)=\Sigma G$. Thus, the integration over space in (D11) is written as

$$\Sigma^R G^< + \Sigma^< G^A - G^R \Sigma^< - G^< \Sigma^A \; = \; i f_0 \left\{ \Sigma^R A + \Gamma G^A - G^R \Gamma - A \Sigma^A \right\} \; = \; 0 \qquad \text{(D12)}$$

where we have used the definitions $\Gamma \equiv -i\,[\Sigma^R - \Sigma^A]$ and $A \equiv -i[G^R - G^A]$ and the equilibrium relations

$$\Sigma^<(r_1, r_2; E) \; = \; i f_0(E) \, \Gamma(r_1, r_2; E) \qquad \text{(D13)}$$

and

$$G^<(r_1, r_2; E) \; = \; i f_0(E) \, A(r_1, r_2; E) \qquad \text{(D14)}$$

$f_0(E)$ being the Fermi-Dirac factor. Also, we have used the fact that, in the absence of magnetic fields, Σ^R, G^R, Γ, and A are symmetric, eg. $A(r_1, r_2; E) = A(r_2, r_1; E)$. Eq. (D12) shows that the energy exchange with the bath is zero at each point R as we would expect under conditions of detailed balance.

In our local scattering model, (D11) can be simplified since the self-energies are proportional to delta functions in space. Using Eq. (2.19) we have

$$P(R) \; = \; \int\!dE\, E \left\{ \frac{n(R;E)}{\tau_n(R;E)} - \frac{p(R;E)}{\tau_p(R;E)} \right\} \qquad \text{(D15)}$$

Using the definitions of $\dfrac{1}{\tau_{p,n}}$, (D11) can be cast into a particularly transparent form (cf. eq. (22) of [51]) (with the position coordinate suppressed),

$$P \; = \; 2\pi \int\!dE \int\!d\omega\, \omega \left\{ F(\omega)\, N_0(E)\, N_0(E+\omega)\, f(E)\, [\,1 - f(E+\omega)\,] \right\} \qquad \text{(D16)}$$

The physical meaning of (D16) is discussed in the text (see Eq. (5.3)).

Appendix E: Optimization of the Energy Grid

Mesoscopic structures, such as a DBRTD, have narrow resonances on the order of a few tenths meV that need to be well resolved. The essential physics of the device may be contained within one or more energy windows of a few tenths meV. However, the the entire energy range corresponding to the applied bias, on the order of hundreds of meV's must also be adequately resolved. A good energy grid is essential to obtaining the correct, current-conserving solution.

The quantities which need to be resolved in energy are the following: (1) the density of states (resonances), (2) $\partial f/\partial E$ in the contacts - the sharp cut-off at the Fermi-energy at low temperatures, (3) the scattering rate, $1/\tau_\phi$, and (4) the current density per unit energy, $J(z;E)$. The scattering rate, $1/\tau_\phi$, is a functional of the density of states, $N_0(z;E)$, and their occupation, $f(z;E)$. For Einstein phonons, the relation is given by (3.11). The scattering rate at energy E is determined by $N_0(E\pm\hbar\omega_o)$ and $f(E\pm\hbar\omega_o)$. Also, since $N_0 = -1/\pi\,\mathrm{Im}\,G^R(z,z;E)$, is calculated self-consistently with τ_ϕ, N_0 sill be enhanced at each $n\hbar\omega_o$ above and below a resonance. The enhancement dies off exponentially with n, and for realistic scattering times, 0.1 - 1.0 ps, we have only seen echo peaks in N_0 one $\hbar\omega_o$ above and below a resonance. In such instances we see enhancements in $1/\tau_\phi$ at one and two optical phonon energies above and below the resonance. Thus, the resonant energy plus one and two optical phonon energies above and below the resonance must be well resolved. If the energy grid is well resolved for the above quantities, then it will generally be well resolved for the energies at which the current is flowing since the majority of the current will be flowing through the main resonance or one or two optical phonon energies above or below the main resonance. However, if the current is flowing off resonance, then we need to resolve the energies of the Fermi-sea in the emitter and energies integer optical phonon energies above and below the energies of the emitter Fermi sea.

The optimization of the energy grid begins with a Romberg integration of $N_0(z;E)$ to create a monotonically increasing function of energy, $M(z;E)$.

$$M(z;E) = \int_{E_{min}}^{E} dE'\,N_0(z;E') \tag{E.1}$$

A constant value for τ_ϕ of ~0.1–1.0 ps is used when evaluating $G^R(z,z;E)$. Thus, the N_0 that is integrated contains the main resonances but not the phonon echoes. A second function, $M_N(z;E)$, is created

$$M_N(z;E) = \sum_{n=-2}^{2} a_n M(z;E-n\hbar\omega_o) \tag{E.2}$$

where a_n are scaling factors < 1. A third monotonically increasing function of energy is created, $M_f(z;E)$, defined by

$$M_f(z;E) = \int_{E_{min}}^{E} dE' (-\partial f(z;E')/\partial dE') \tag{E.3}$$

M_f and M_N are normalized to their maximum values, weighted, added, and integrated over position to form the function that is used to optimize the energy grid, $M_{opt}(E)$.

$$M_{opt}(E) = \sum_{i} \int_{R_i} dz [c_1 M_N(z;E) + M_f(z;E)] \tag{E.4}$$

where R_i represents user specified spatial regions of integration. The vertical M_{opt} axis is divided into equally spaced nodes whose number corresponds to the desired number of energy grid points. The nodes are projected horizontally across to the function $M_{opt}(E)$ and then vertically down to the energy axis. The intersections with the energy axis are the optimized energy grid points. If necessary, after several iterations, a similar type of optimization can be done based on the energy distribution of the current density.